Conference Proceedings of the Society for Experimental Mechanics Series

Evro Wee Sit *Editor*

Sensors and Instrumentation, Volume 5

Proceedings of the 33rd IMAC, A Conference and Exposition on Structural Dynamics, 2015

SEM

Springer

Conference Proceedings of the Society for Experimental Mechanics Series

Series Editor

Tom Proulx
Society for Experimental Mechanics, Inc.
Bethel, CT, USA

More information about this series at http://www.springer.com/series/8922

Evro Wee Sit
Editor

Sensors and Instrumentation, Volume 5

Proceedings of the 33rd IMAC, A Conference and Exposition on Structural Dynamics, 2015

Springer

Editor
Evro Wee Sit
SVcommunity.com
Hermosa Beach, CA, USA

ISSN 2191-5644 ISSN 2191-5652 (electronic)
Conference Proceedings of the Society for Experimental Mechanics Series
ISBN 978-3-319-15211-0 ISBN 978-3-319-15212-7 (eBook)
DOI 10.1007/978-3-319-15212-7

Library of Congress Control Number: 2015937182

Springer Cham Heidelberg New York Dordrecht London

Printed on acid-free paper

Springer International Publishing AG Switzerland is part of Springer Science+Business Media (www.springer.com)

Preface

Sensors and Instrumentation represents one of ten volumes of technical papers presented at the 33rd IMAC, A Conference and Exposition on Structural Dynamics, 2015, organized by the Society for Experimental Mechanics, and held in Orlando, Florida February 2–5, 2015. The full proceedings also include volumes on Nonlinear Dynamics; Dynamics of Civil Structures; Model Validation and Uncertainty Quantification; Dynamics of Coupled Structures; Special Topics in Structural Dynamics; Structural Health Monitoring and Damage Detection; Experimental Techniques, Rotating Machinery and Acoustics; and Shock and Vibration Aircraft/Aerospace, Energy Harvesting; and Topics in Modal Analysis.

Each collection presents early findings from experimental and computational investigations on an important area within Sensors and Instrumentation. Topics represent papers on calibration, smart sensors, rotational effects, stress sensing and tracking of dynamics. Topics in this volume include:

Experimental Techniques
Smart Sensing
Rotational Effects
Dynamic Calibration

The organizers would like to thank the authors, presenters, session organizers, and session chairs for their participation in this track.

Hermosa Beach, CA, USA — Evro Wee Sit

Contents

Chapter 1
LLCD Experimental Line-of-Sight Jitter Testing

Brandon J. Dilworth

Abstract The LLCD program at MIT Lincoln Laboratory is the first space laser communication system for NASA. The optical communications terminal was carried into lunar orbit by the LADEE spacecraft which launched on September 6, 2013. The primary goal of the LLCD program is to demonstrate optical communication from lunar orbit to the Earth's surface.

Optical communication systems have many advantages over RF systems which include achieving higher data rates using lower size, weight and power (SWaP). Optical communication systems rely on much narrower beams than RF systems to achieve these advantages; the penalty is that the optical beam must have good stability in order to maintain the communication link between the transmitter and receiver. There are a number of factors that play a role in the stability of the optical beam, but the focus of this talk is on the residual LOS jitter resulting from unrejected spacecraft excitation. Experimentation with physical hardware is a common method for validating mathematical models, including residual LOS jitter models. The LLCD program developed a test bench in order to validate the residual LOS jitter model which provides higher confidence in the computational results.

Keywords LOS jitter • Optical communication • Model validation • MIMO sine testing • LLCD

Nomenclature

DOF	Degree of Freedom
FEM	Finite Element Model
ICD	Interface Control Document
IR	Infrared
LADEE	Lunar Atmosphere and Dust Environment Explorer
LLCD	Lunar Laser Communication Demonstration
LOS	Line-of-Sight
MAC	Modal Assurance Criterion
MIMO	Multiple Input Multiple Output
MIRU	Magneto-hydrodynamic Inertial Reference Unit
MIT	Massachusetts Institute of Technology
NASA	National Aeronautics and Space Administration
PSD	Power Spectral Density
RF	Radio Frequency
SNR	Signal-to-Noise Ratio

Statement
This work is sponsored by the National Aeronautics and Space Administration under Air Force Contract #FA8721-05-C-0002. Opinions, interpretations, conclusions and recommendations are those of the author and are not necessarily endorsed by the United States Government.

B.J. Dilworth, Ph.D. (✉)
MIT Lincoln Laboratory, 244 Wood Street, Lexington, MA 02420, USA
e-mail: brandon.dilworth@ll.mit.edu

E.W. Sit (ed.), *Sensors and Instrumentation, Volume 5*, Conference Proceedings of the Society for Experimental Mechanics Series, DOI 10.1007/978-3-319-15212-7_1

1.1 Introduction

The LLCD program developed and fielded the first duplex laser communication system for NASA. MIT Lincoln Laboratory designed and built a space terminal for lunar orbit and the primary ground terminal to execute the demonstration. A month after launch, the LLCD system demonstrated a 20 Mbps uplink and a 622 Mbps downlink between the Moon and the Earth. Both links represent data rates much higher than ever achieved previously over that distance. An overview of the system architecture and demonstration results have been previously published [1].

Optical communication systems use much shorter (>10,000×) wavelengths as compared to existing RF communication systems. The shorter wavelengths enable large bandwidth modulation, higher data rates and low diffraction losses as compared to RF systems. The shorter wavelength results in a narrow beamwidth which means that the optical terminals (at both ends of the link) can be much smaller and require less power than their RF counterparts. However, a narrow beamwidth means beam stability becomes a much more significant challenge. For the LLCD space terminal, the resulting requirement was that the beam had to be stabilized better than 4.2 μrad to maintain the communication link.

The space terminal optical module included several features in order to achieve the pointing requirements which are graphically summarized in Fig. 1.1. Initial pointing of the terminal is executed by the spacecraft with accuracy based on the performance of its star trackers. The 2-axis gimbal provides coarse pointing while the MIRU provides the fine pointing and inertial stabilization of the optical head. The telescope is an all-beryllium structure with a 10 cm primary mirror. The approach of the control system and the architecture of the optical paths have been described previously [2].

1.2 Line-of-Sight Jitter

Line-of-sight jitter is simply defined as the time-varying motion of the image on the detector plane [3]. In imaging systems (like cameras), LOS jitter can result in blurred images. In laser communication systems, LOS jitter can result in loss of data rate. In both scenarios, the LOS jitter can be induced either internally from or externally to the system. Typical sources of self-excitation are due to the tracking system mechanism(s). On the LLCD Space Terminal, the dominant sources of self-excitation were due to the Gimbal motion (stepper motors) and the nutation mechanism on the Optical Head. Primary sources of external excitation were due to the reaction wheels on the LADEE spacecraft coupling through the spacecraft structure and acting as base excitation to the Instrument Panel. The external excitation was prescribed early in the program based on

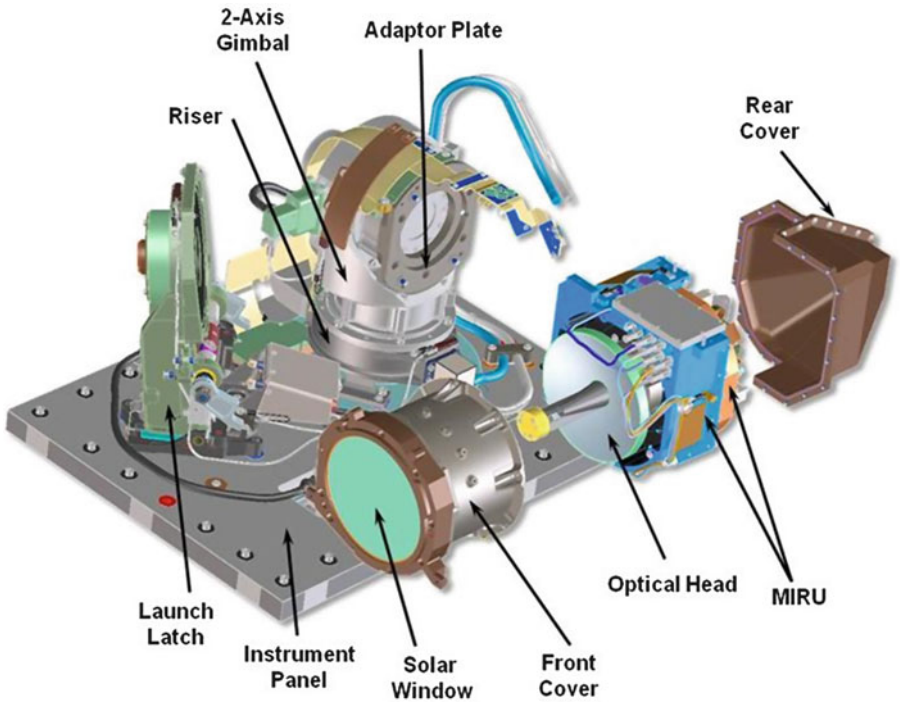

Fig. 1.1 LLCD space terminal optical module

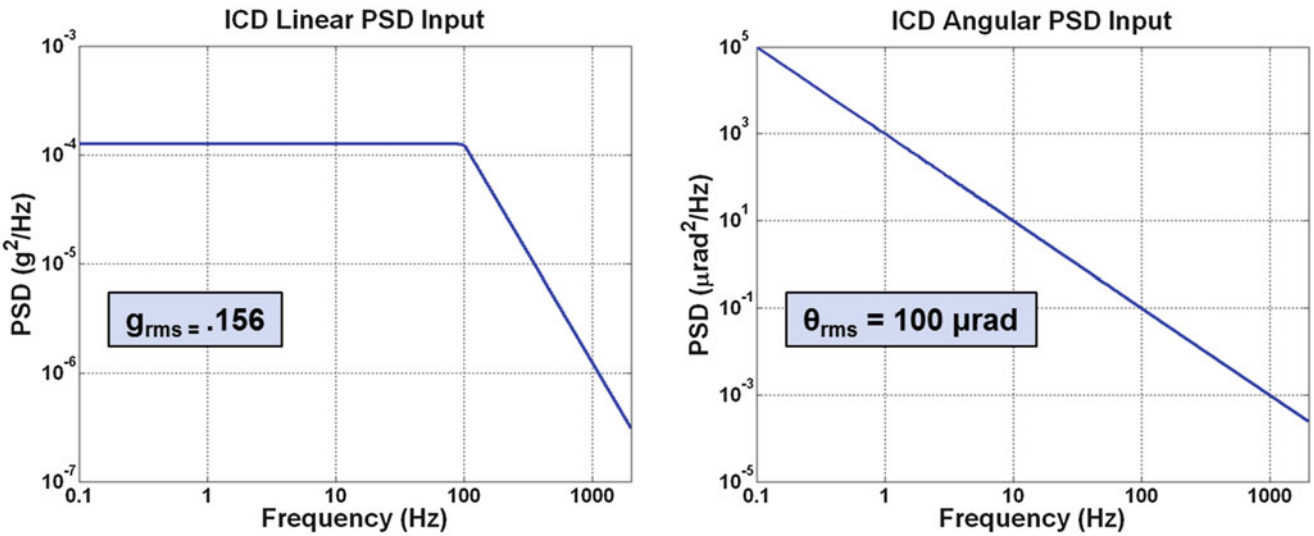

Fig. 1.2 Excitation disturbance defined at instrument panel

previous experience of the team, and was defined in the ICD as shown in Fig. 1.2. From the angular disturbance alone, it is apparent that some stabilization control is required to bring the 100 μrad disturbance down to less than 4.2 μrad of residual LOS jitter.

As system performance is greatly dependent on the LOS jitter performance, a computational model was developed to study design tradeoffs and to verify system requirements [4]. The modeling efforts went through several iterations of validation and updating throughout the program [5]. The focus of this paper is on the experimental efforts which supported the model validation of the LOS jitter computational model.

1.3 Test Setup

Conceptually, the LOS jitter test bench needed to provide three functions: base excitation to the Optical Module, dynamic measurement of the excitation at the base of the structure and dynamic measurement of the beam position. Practically, several tradeoffs were considered when developing the test bench which balanced cost with resultant data. One significant assumption used when weighing the tradeoffs was that the structure would act as a linear system during test. The advantage of the structure assumed to be a linear system meant that the input excitation would not need to match the ICD disturbances exactly, which greatly simplifies the design requirements on the test setup and test fixture structure.

In order to provide base excitation to the system the test fixtures needed to be able to support the weight of the Optical Module and all of the test fixtures, provide 6-DOF motion at the base of the Optical Module, and needed to have provisions for incorporating exciters. A product sold as an isolator system was cable of supporting both the weight of the test structure and provide the 6-DOF motion. Electro-dynamic exciters were selected to provide the base excitation to the test structure, connected through additional fixtures. The shakers were sized based on the prescribed ICD linear acceleration and the expected mass of the test structure (Optical Module plus all additional fixtures). A second isolation table provided the reaction mass for the shakers in addition to providing isolation from any environmental/room excitation. In an effort to keep test fixture costs down, only three shakers were included in the setup which did not enable all 6-DOF's to have similar excitation levels concurrently. However, arranging the shakers into multiple configurations enabled all 6-DOF base motion to be evaluated.

Dynamic measurement of the excitation at the base of the Optical Module was enabled by a triaxial accelerometer and three angle rate sensors to characterize the 6-DOF motion. The angle rate sensors enabled measurement of the angular DOF's directly, which helped reduce opportunities for measurement errors as compared with post-processing several accelerometer sensors configured in a geometry such that angular DOF's could be calculated. The accelerometer was mounted near the pivot point of the angular DOF's to passively minimize effects due to the angular excitation. The angle rate sensors were mounted at the perimeter of the instrument panel of the Optical Module. Figure 1.3 shows the test structure with the Optical Module under test in one (of multiple) shaker configurations.

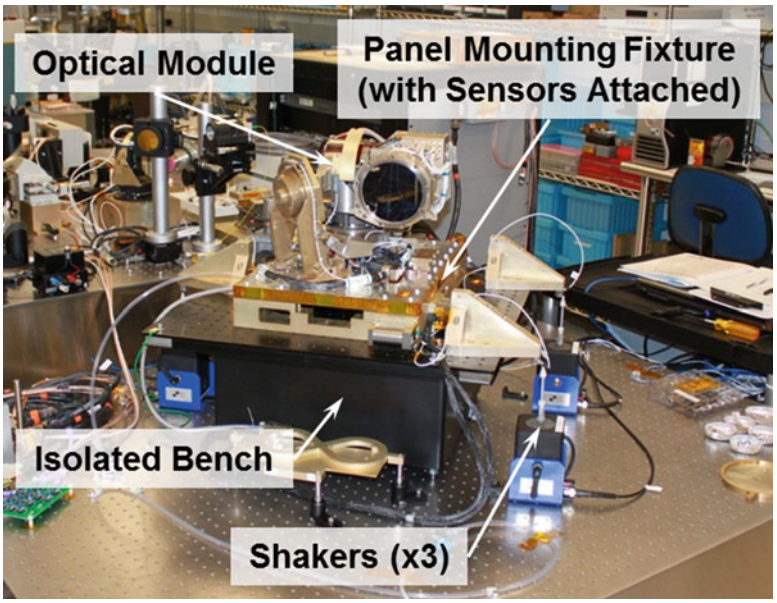

Fig. 1.3 Photograph of test setup

The dynamic measurement of the beam position was enabled through the use of an optical test bench. The details of the layout of the optical test bench are not described in detail in this paper, but the enabling sensor to measure the dynamic position of the beam was an IR camera. The IR camera output was coupled with a centroid estimating algorithm which operated at near a 4 kHz update rate. At the smallest frame size of the camera, the resolution of the centroid estimate was about 0.8 μrad which provided enough SNR to reliably capture the beam dynamics in the frequencies of interest. A graphical representation of the test setup is provided in Fig. 1.4 which provides an overview of the entire test setup architecture.

1.4 Test Methodology

As stated before, this experimental effort was in support of model validation of the FEM developed to predict overall residual LOS jitter performance. With that perspective in mind, the test bench was developed to target the frequencies which were predicted to be the most predominant in the context of LOS jitter. It was this perspective which drove the test bench to be capable of supporting a test bandwidth of 5–1,000 Hz.

Initial estimates from the FEM suggested that the first flexible modes related to bending of the gimbal had the most dominant role, which were initially predicted to be near 60.3 Hz. The MIRU had an internal mode near 11 Hz and even though it was assumed that this mode would be mitigated by the inertial stabilization loop, this frequency was used as one bound to define the lower excitation frequency of the test bench. The angle rate sensors used to measure the angular DOF's of the test bench described previously have a useable bandwidth of 5–1,000 Hz. Although other constraints were considered to limit the low frequency excitation of the system (such as stroke limits of the exciters and the isolation table), 5 Hz was selected primarily based on the usable bandwidth of the angle rate sensors.

A typical approach to presenting LOS jitter results is to show forward and backward cumulative RMS plots to compliment a PSD response. The FEM predicted LOS jitter response plots are shown in Fig. 1.5 which provided initial insight to system performance. The FEM predicted that excitation frequencies above 500 Hz would have minimal impact to the overall residual LOS jitter (cumulative sum above 500 Hz roughly 10× below total). In order to validate that prediction with confidence, the upper bound test frequency was selected to be 1,000 Hz.

Due to resource availability, the excitation method was developed using a preliminary optical test bench. Initial characterization of the preliminary test bench indicated that the noise floor of the optical response was much higher than expected. As a result, MIMO sine control excitation using force feedback at the stinger attachment points was selected to drive the base motion of the system. Both stepped and swept sine excitation methods were evaluated and swept sine was determined to provide the best trade-off between fidelity of the data and time of test execution. Random excitation was evaluated, but excitation levels could not be driven at high enough levels to provide reliable measurements above the sensor noise floor of the initial optical test bench. Although the final optical test bench had greatly improved performance, as noted above, the entire base excitation test procedure was developed using the initial optical test bench.

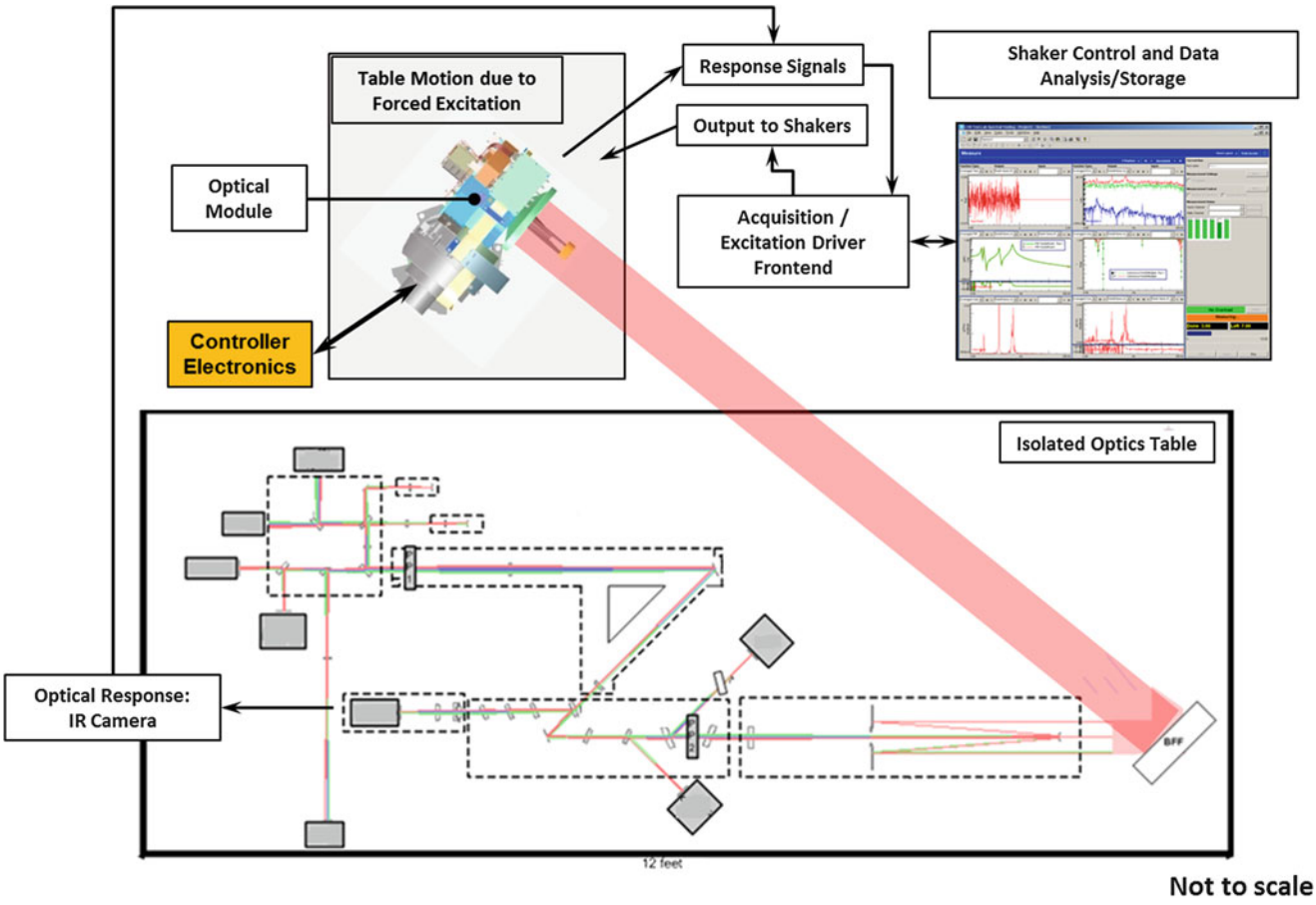

Fig. 1.4 Test setup architecture

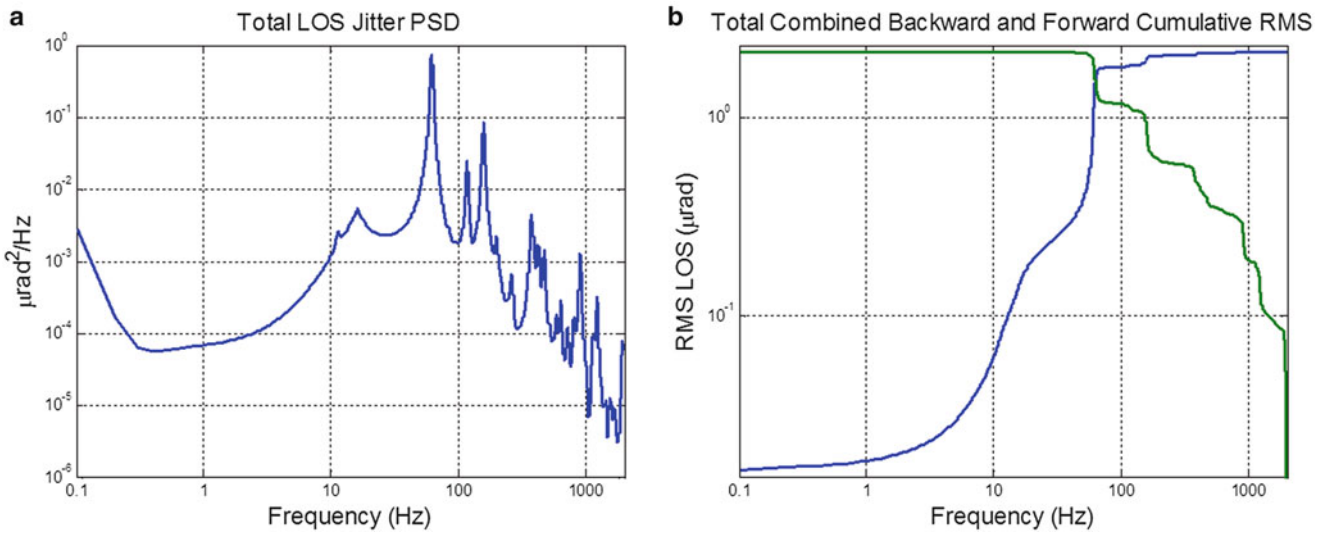

Fig. 1.5 FEA predicted LOS jitter response PSD (**a**) and corresponding cumulative RMS (**b**)

1.5 Test Execution

One of the very first tests conducted was to verify that the excitation provided to the base of the optical module would not propagate to the optical test bench. A simple transmissibility test was conducted using a fixed light source on the optical test bench in addition to placing seismic accelerometers on the bench. The triaxial accelerometer on the base of the optical module was used as the reference signal. Although the quantitative data is not shown in this paper, there was no resolvable evidence (with the sensors used) of the shaker excitation propagating to the optical test bench. As an isolated optical bench was used both on the optical test bench and on the optical module base excitation test bench coupled with low (but representative) excitation levels provided to the system, the measure of low transmissibility was not surprising.

Another set of tests were executed to validate the linear system assumption. Although it was expected that the 2-axis gimbal would act non-linear in many different conditions, the test structure was linearized to within 1 % (based on modal frequencies) by bounding the input excitation levels based on the ICD base excitation disturbance. Base excitation was provided to the optical module and data were processed as an operational modal test using the accelerometer at the base of the optical module as the phase reference. The test was conducted in this manner as the shaker attachment points were not on the test structure itself, but rather attached to test fixtures which precluded the opportunity of running a more classical modal test. Data shown in Fig. 1.6a identifies a sub-set of crosspowers used to curve fit the modal parameters and the modal frequency results indicating linearity within 1 % between all of the excitation levels. Figure 1.6b shows the MAC analysis between two sets of the mode shape vectors which indicate that the mode shapes are consistent at the different excitation levels as well. These results validated the linear system assumption for the excitation levels prescribed for the LOS jitter testing. These tests also provided the data to support the model updating described in previously [5] which improved the model results from over 25 % error down to within 3.5 % error.

Once the final optical test bench was operational, a set of tests were conducted to characterize its dynamic response with a fixed light source. As shown in Fig. 1.4, there are several optical elements in the optical path. Each optical element has its own mounting structure and is typically mounted to the optical bench using bolted attachments. There are several elements in the optical path that have mounting structures with tip/tilt adjustment. For the adjustable mounts used on this optical bench, the adjustment mechanism was spring-loaded. A point not mentioned previously is that all optical tests were conducted in a clean room environment. A consequence of operating in a clean room is that the air handling can have substantial effects on optical measurements. Other dynamic effects, such as floor excitation from the surrounding laboratory environment, were also presumed to influence the behavior of the optical measurement. In order to characterize and baseline the optical response due to the environmental conditions, a fixed light source was mounted on the optical test bench and data were collected at the IR camera. A photograph of the fixed light source is shown in Fig. 1.7a and the measured response is shown in Fig. 1.7b. There are two artifacts noted in the measured response. The first artifact is associated with the dynamics of the optical test bench due to the environmental conditions in the room. Fortunately, all of the dynamics associated with the

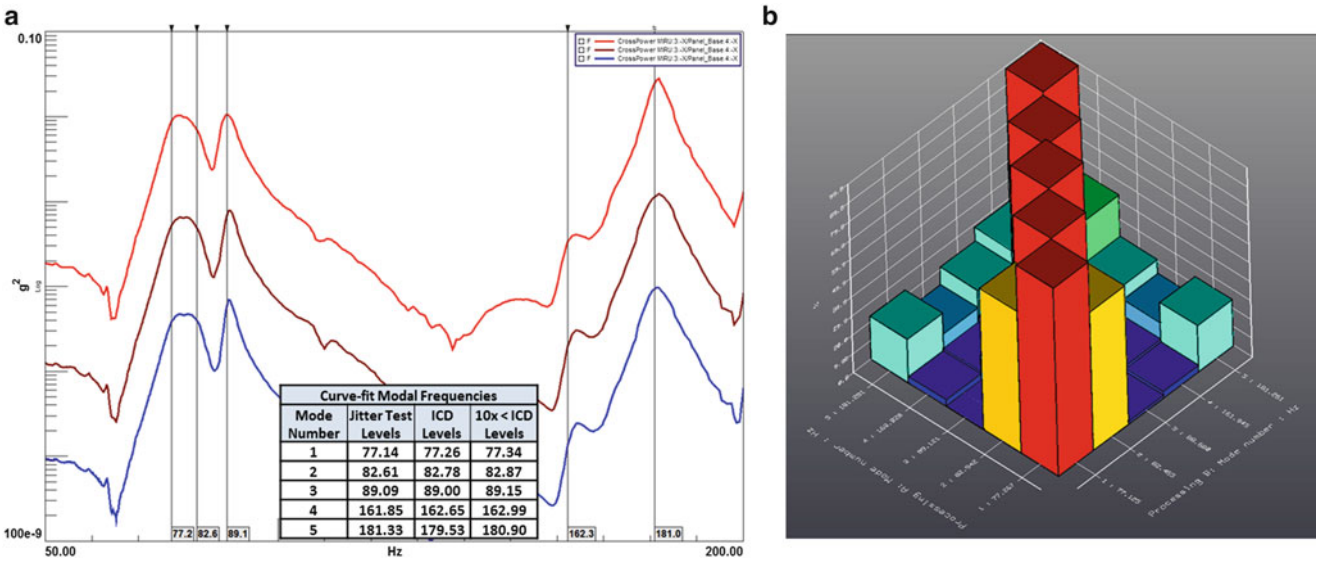

Fig. 1.6 Sub-set of crosspowers used to curve fit modal parameters (**a**) MAC calculation between two sets of mode shape vectors due to different excitation levels (**b**)

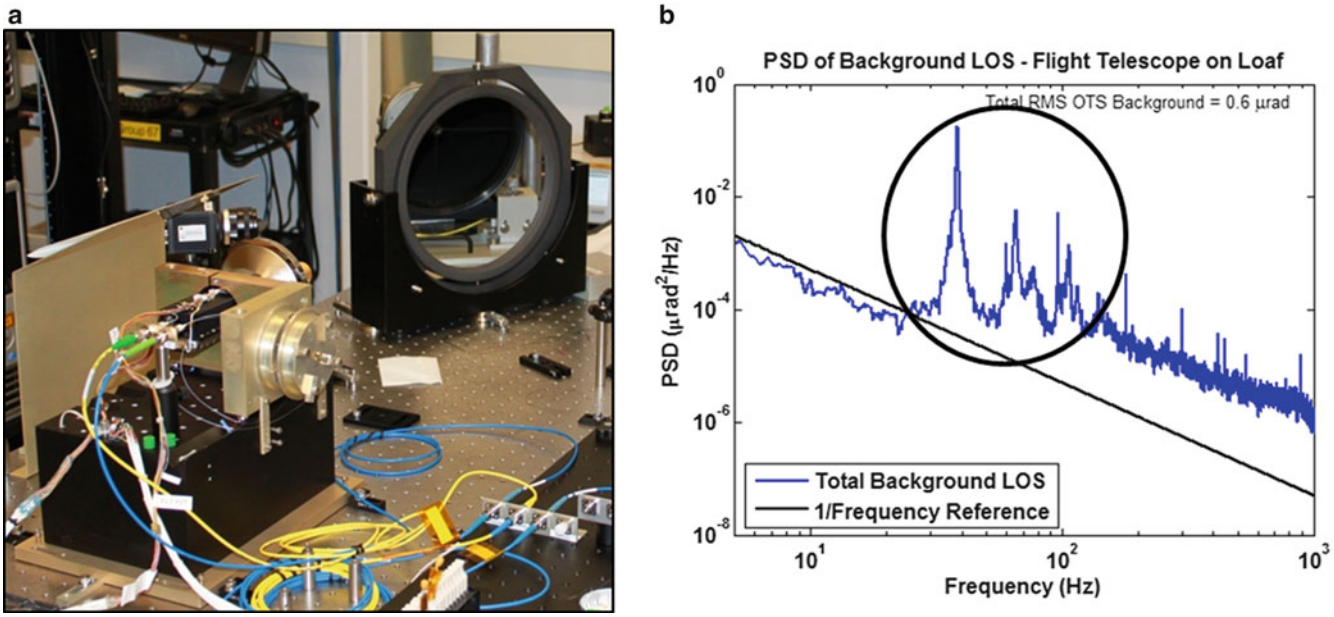

Fig. 1.7 Photograph of fixed light source (**a**) Response due to background environment (**b**)

optical response occur at different frequencies than the modes of the optical module. The second artifact is the typical 1/f or "flicker noise" which is associated with the digital IR camera electronics. This background measurement proved to be very useful to understand the full measurement chain in the LOS jitter measurement.

The last consideration prior to final LOS jitter testing was attempting to quantify the effects of the air handling between the optical module and the optical test bench. Although not shown to scale in Fig. 1.4, there was roughly 12 ft of open air space between the optical model and the first optical element on the optical test bench. Tests were conducted with varying amounts of passive approaches to mitigate the effects due to the airflow in the room. Simple structures such as tubes and tarps shown in Fig. 1.8a were used to quantify the effects. Results of the mitigation techniques are shown in Fig. 1.8b indicating up to a 3× improvement in the noise floor of the measurement, with the primary improvement noted in frequencies below 20 Hz.

Final LOS jitter testing applied all of the lessons learned based on previous experiments: defining input loads to the test structure, validating the linear system assumption for the LOS jitter input loads, characterizing the dynamics of the optical test bench, and mitigating effects due to the airflow in the clean room. Measurements were collected using multiple shaker configurations to allow each of the 6 base excitation DOF's to be excited at or above ICD levels. Combining these measurements verified that no one particular DOF dominated the LOS jitter response. The raw measured data from the LOS jitter experiment was post-processed to account for the background noise of the optical test bench and the fact that the experimental inputs exceeded the ICD excitation at most frequencies. Although the details of the post-processing are not described in this paper, the results provided evidence that the optical module would be able to meet its LOS jitter performance requirements. Coupling the post-processed results with the final updated FEM provided the last step in the successful model validation effort as shown in Fig. 1.9. Although the results do not overlay perfectly, the overall system behavior is well matched in the two data sets.

1.6 Conclusions

An experimental LOS jitter test bench was developed for the LLCD program which was used to validate the FEM used to predict performance. The LOS jitter test bench offered insight to the dynamics of the optical module which would have otherwise gone uncharacterized. Clear evidence was made to underline the advantage of such a test bench and highlight the versatility of such a test setup.

Conducting tests as operational modal tests enabled model updating where a classical modal test was not possible. Dynamic characterization of the optical test bench was essential to understanding the optical response and differentiating

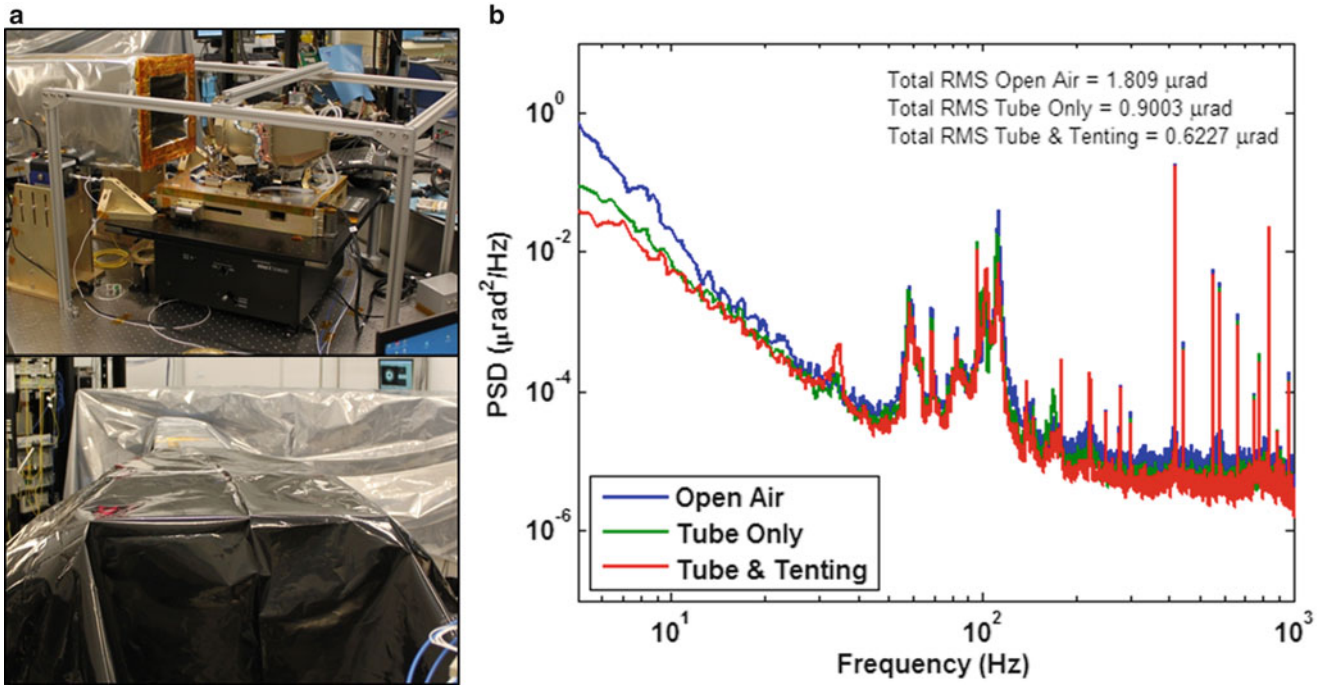

Fig. 1.8 Airflow mitigation (**a**) Results of passive airflow mitigation (**b**)

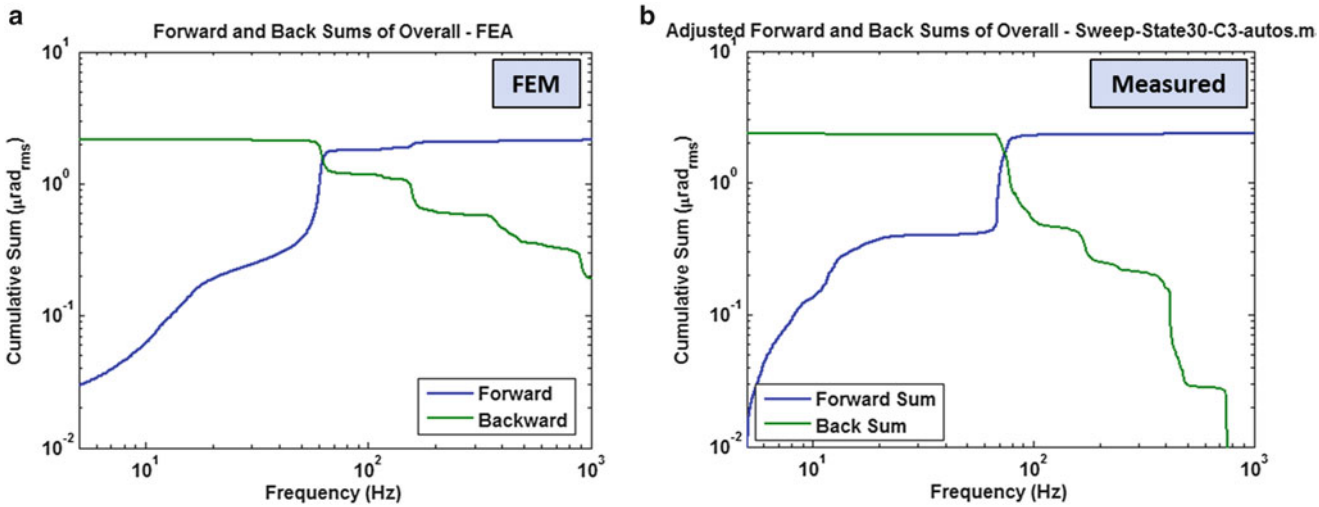

Fig. 1.9 FEM predicted LOS jitter (**a**) Post-processed measured LOS jitter results (**b**)

between optical module dynamics from optical response behavior. Passive airflow mitigation techniques proved to be helpful in improving the SNR of the measurement at lower frequencies.

The LOS jitter test bench enabled the FEM to be validated which provided confidence in final system performance prior to launch. Although the LOS jitter test bench offered the initial indication that the optical module would meet its performance requirements, the final validation occurred during the successful performance of the optical communication link while on orbit around the moon.

Acknowledgements The author would like to thank the LLCD team members who helped contribute to this work through several insightful discussions and time and effort in the lab: Allen Pillsbury, Dennis Burianek, Stephen Conrad, Jamie Burnside, Kate Nevin, Michele Weatherwax, Cathy DeVoe, Amy Raudenbush, Jay Petrilli and Joe Warfel. The author would also like to thank the team at NASA Goddard Space Flight Center for their support of this work.

References

1. Boroson D, Robinson B, Murphy D, Burianek D, Khatri F, Kovalik J, Cornwell D (2014) Overview and results of the lunar laser communication demonstration. In: Proceedings of the SPIE 8971, free-space laser communication and atmospheric propagation XXVI. San Francisco, CA
2. Burnside J, Conrad S, Pillsbury A, DeVoe C (2011) Design of an inertially stabilized telescope for the LLCD. In: Proceedings of the SPIE 7923, free-space laser communication technologies XXIII. San Francisco, CA
3. Doyle K, Genberg V, Michels G (2002) Integrated optomechanical analysis, vol TT58. SPIE Press, Bellingham, p 140
4. Nevin K, Doyle K, Pillsbury A (2011) Optomechanical design and analysis for the LLCD space terminal telescope. In: Proceedings of the SPIE 8127, optical modeling and performance predictions V. San Diego, CA
5. Weatherwax M, Doyle K (2014) Vibration analysis and testing for the LLST optical module. In: Proceedings of the SPIE 9192, current developments in lens design and optical engineering XV. San Diego, CA

Chapter 2
A Virtual Reality Glovebox with Dynamic Safety Modeling for Improved Criticality Regulation Visualization

Kyle Embry, Andrea Hengartner-Cuellar, Hannah Ross, and David Mascareñas

Abstract Technicians working in gloveboxes must vigilantly keep track of the locations of the radioactive materials they work with in order to make sure they do not inadvertently perform an action that can lead to a technical criticality safety violation. The administrative consequences of these mistakes can result in halting work in a facility and can be costly. The process currently used to ensure safe operations requires every two technicians to be monitored and documented by a third technician, thus resulting in large overhead costs. This work aims to help reduce the possibility of incurring an administrative criticality violation by tracking the dynamics of nuclear materials located inside a glovebox. Emerging technologies in sensing and virtual/augmented reality were combined with knowledge of nuclear criticality regulations to create a prototype Interactive Electronic Work Control System. Visual and depth sensors are used to detect the dynamically changing location of fissile materials in a glovebox during simulated working conditions. These measurements are then fed into a representative criticality safety model to determine appropriate separation distances between different materials. A visual depiction of these models is overlaid on representations of physical objects using virtual reality technologies to enhance the operator's perception of criticality safety regulations.

Keywords Glovebox • Augmented reality • Virtual reality • 3D sensing • Nuclear criticality safety

2.1 Introduction

2.1.1 Background

When a material needs to be isolated from the external environment, a sealed container called a glovebox is often used to perform necessary operations. Some materials require a controlled environment while others, such as radioactive materials, need to be isolated due to their potential to cause harm to personnel. The use of gloveboxes for operations involving nuclear materials is dictated by criticality safety regulations, which are an extensive set of rules written to ensure that all operations involving radioactive materials pose the smallest threat possible to technicians working in hazardous areas. A set of gloveboxes used at Los Alamos National Laboratory (LANL) is shown in Fig. 2.1 [1].

Although nuclear criticality safety regulations are written to ensure that glovebox operations are inherently safe, an additional, more stringent set of administrative criticality safety regulations exist to further ensure no harm comes to technicians working with hazardous materials. These administrative regulations control the proximity of different objects within a glovebox. Ensuring these regulations are followed is a tedious, costly process that often requires additional technicians devoted solely to overseeing and documenting each operation. Although manual observation and documentation is a functional method for enforcing administrative criticality safety regulations, a computerized approach has the potential to reduce violations. The proposed system, an Interactive Electronic Work Control System (IEWCS), would give operators a physical sense of radiation and criticality regulations to make them more aware of the invisible characteristics of the materials they are handling.

K. Embry (✉)
Department of Mechanical Engineering, Missouri University of Science and Technology, Rolla, MO 65401, USA

A. Hengartner-Cuellar
Department of Cognitive Science, University of California Berkeley, Berkeley, CA 94704, USA

H. Ross
Department of Mechanical Engineering, Tennessee Technological University, Cookeville, TN 38505, USA

D. Mascareñas
Engineering Institute, Los Alamos National Laboratory, Los Alamos, NM 87545, USA

E.W. Sit (ed.), *Sensors and Instrumentation, Volume 5*, Conference Proceedings of the Society for Experimental Mechanics Series, DOI 10.1007/978-3-319-15212-7_2

Fig. 2.1 Gloveboxes at Los Alamos National Laboratory

An important consideration in the development of the IEWCS is the method used to monitor activity in a glovebox. Monitoring could potentially be accomplished by the use of a 3D sensor that can track motion in real-time. The popularity of 3D sensors for motion gaming applications has enabled cost-effective 3D imaging to become widely accessible. Some of these sensors use infrared cameras to virtually reconstruct their surroundings and infer object positioning in 3D space. Creation of these reconstructions requires the detection of objects, assimilation of multiple images into a single point cloud, and visualization of inferred surfaces [2]. Research in this area has been applied to several fields, including marketing [3], rehabilitation [4], and industry [5]. Siemens has used this type of sensor for planning maintenance tasks in areas exposed to nuclear radiation. Operators simulate the motions necessary to complete specific jobs while being scanned by a Microsoft Kinect sensor. The operator's motions are saved and integrated into a model of the building that contains radiation hazard information to calculate the exposure that the operator would receive while performing the task. This process is repeated until the exposure is determined to be as low as reasonably achievable.

Finally, a method is needed to visualize information about a material's radioactivity. Augmented or virtual reality technologies are being considered for this application. Augmented reality (AR) is a layering of virtual information over real-world objects; it merges tangible reality with digital information [6]. Virtual reality (VR) is "the use of computer technology to create the effect of an interactive three-dimensional world in which the objects have a sense of spatial presence" [7]. While both AR and VR technologies were originally inspired by the gaming community, they have since been widely applied to scientific, industrial, and commercial research. In the medical field, surgeons have experimented with AR technology to overlay X-ray images onto the site of injury during operations [8]. Similarly, in industry, AR and VR products have been used to interactively guide workers through steps requiring detailed instructions, suggesting a potential to replace directive handbooks [9]. Researchers have also found a wide range of applications for AR and VR technologies in the nuclear industry. Hirotake [10] states that VR can reduce the time, expense, and danger associated with the education of nuclear power plant employees for both operations and maintenance training. Researchers at LANL have also used VR to examine the possibilities of deploying nuclear safeguard systems. A study completed by Michel [11] concluded that regulations and procedures related to nuclear criticality safety can be incorporated into a VR environment and used for design, planning, training and safety enforcement purposes.

2.1.2 Motivation

Although emerging technologies are currently being implemented in the nuclear field with promising results, continued research in their application to criticality safety is essential to determine if these technologies can contribute significantly to decreasing the number of administrative criticality safety violations in routine operations. Gloveboxes in particular have the potential to benefit from AR/VR technologies. Operators currently rely solely on personal knowledge and alertness to safeguard against administrative criticality violations, and experience has shown that many violations are either unnoticed or unreported. Although these violations do not result in safety hazards to personnel, their occurrence can cause costly facility shutdowns and lengthy policy re-evaluations. This research has the potential to reduce the number of administrative criticality

violations in routine operations and eliminate the need for redundant technicians to ensure safety regulations are followed. A heightened awareness of radiation would allow technicians to be better informed about their work, thus increasing their ability to conduct operations in a safe and confident manner.

2.1.3 Purpose

To test the practicality of the IEWCS, a prototype was created to demonstrate the system's ability to display useful information onto the user's view. The development of the IEWCS prototype necessitated the use of emerging technologies in 3D sensing and information visualization, as well as their novel integration with a computational model of technical criticality regulations. An array of infrared sensors collected point cloud data inside the prototype glovebox, and object-identification algorithms were used to detect if these measurements were representative of fissile material containers. Once these containers were identified, a simplified computational model of the nuclear criticality regulations found the minimum acceptable distance between fissile materials. As the containers were moved around the glovebox, the results of this computational model were presented on a wearable VR device, equipping the user with a physical sense of the regulations that ensure his/her safety.

2.2 Experimental Procedure

As mentioned above, the IEWCS prototype consisted primarily of the following three processes, which are explained in further detail below.

1. Object identification
2. Nuclear criticality safety modeling
3. Information visualization

Information was passed among these three processes using the open-source software Robot Operating System (ROS) [12].

2.2.1 Object Identification

To identify and track fissile material containers inside a glovebox, it was necessary to implement an object identification algorithm that has the ability to recognize a specific shape. The majority of the code utilized in this system was taken from the Point Cloud Library (PCL), an open-source library of algorithms that processes point clouds composed of three dimensional image data [13]. Point clouds of a test container were generated using an array of four identical Microsoft Kinect sensors. A global reference frame was defined during laboratory testing, and it is illustrated in Fig. 2.2. The solid

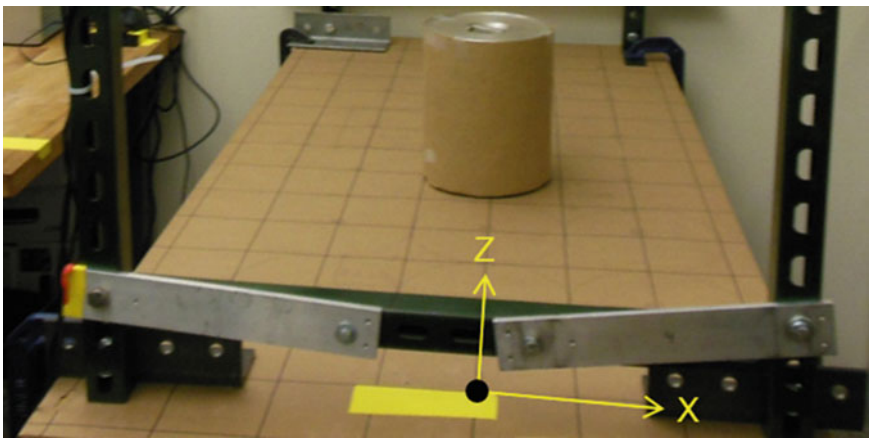

Fig. 2.2 Grid showing the global reference frame origin and axes

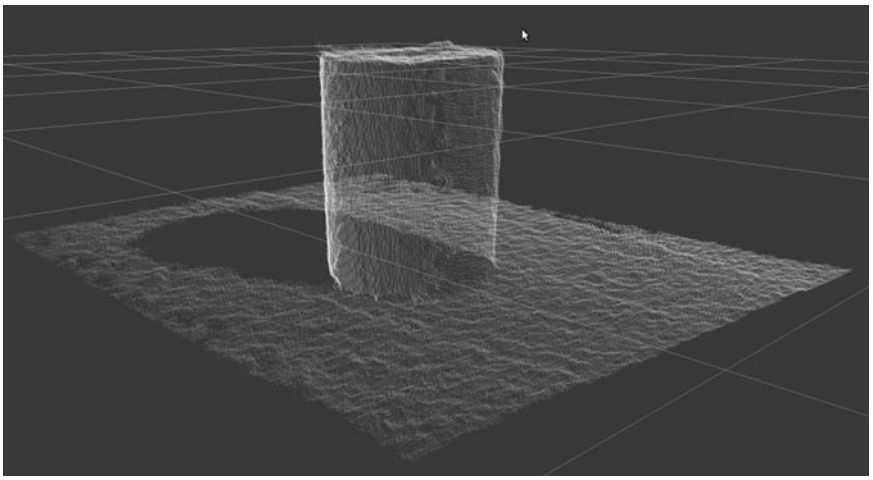

Fig. 2.3 A point cloud representation of the region of interest shown in Fig. 2.2

black circle at the bottom of the figure represents the spot defined as the origin. The X and Z axes denoted on the figure represent directions along the grid while the positive Y axis (not shown) is defined perpendicular to the grid and pointing towards the floor.

The transformation matrices used to align the point clouds with the global reference frame were calculated separately for each Kinect sensor using the ar_kinect package developed by Ferguson for use with ROS [14]. The transformations were then refined manually. After each transformation was applied, the point clouds were concatenated together to form a single dataset containing all of the information from the sensor array. To reduce the amount of data analyzed in further calculations, all points outside of the region of interest defined by the grid in Fig. 2.2 were then removed from the dataset. A point cloud representation of this region of interest is shown in Fig. 2.3.

Next, because cylindrical containers are common in a glovebox workspace, PCL's Sample Consensus algorithm for cylinder segmentation was applied to the point cloud. This algorithm first recognized and eliminated any planar objects found in the dataset, reducing the number of points that were passed on for further processing. The algorithm then identified any cylinders that were within the bounds of user-specified parameters and eliminated all remaining points. The final output of this algorithm was a point cloud consisting of only the data points judged to lie on the surface of the recognized container. The radius and three-dimensional centroid of the point cloud were calculated and output for further analysis.

2.2.2 Nuclear Criticality Safety Modeling

Because nuclear criticality safety regulations are complex and extensive, a very simplified model, calculated using Eq. 2.1, was used for the initial IEWCS prototype.

$$I_i = \sum_{i=1}^{n} \frac{k_n}{d_i^2} \tag{2.1}$$

In Eq. 2.1, I_i is radioactive intensity at each point i, n is the number of containers, k_n is the representative coefficient of radiation, dependent upon material type, and d_i is the distance from the container centroids to each point i. This model is used to represent the interactions between two containers that could hold nuclear materials. This model does not necessarily capture criticality features accurately; it is solely used as a very rough approximation to quickly implement the system. The main goal of this model is to convey the message that criticality safety decreases when two radioactive materials are within close proximity of each other. To implement this model, an algorithm was written that discretized the space in the region of interest shown in Fig. 2.2 into discrete points. Each point was then assigned n independent values based on its distance from each of the containers. The representative intensity of radiation, I_i, was then calculated by summing the values at each point. When the containers were moved within a particular distance of each other, the intensity reached a certain threshold and the points between the two cylinders changed from a grey to a purple color to warn the operator that an administrative violation was soon to occur. If the containers were moved even closer, the points changed from purple to blue to communicate that an administrative violation had occurred. A visualization of the model is shown in Fig. 2.4, where the red shape represents a container fixed in space and the green shape is a dynamic marker that tracks a moving container.

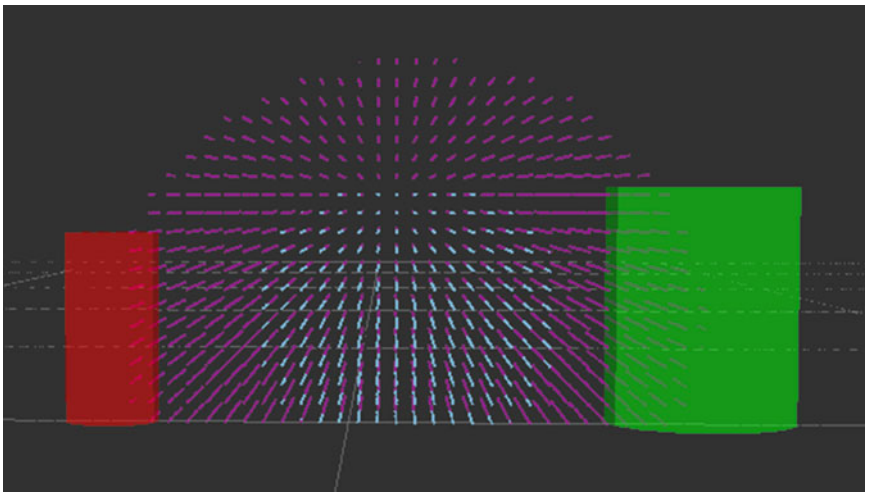

Fig. 2.4 Model showing the warning signs displayed when an administrative criticality safety violation occurs

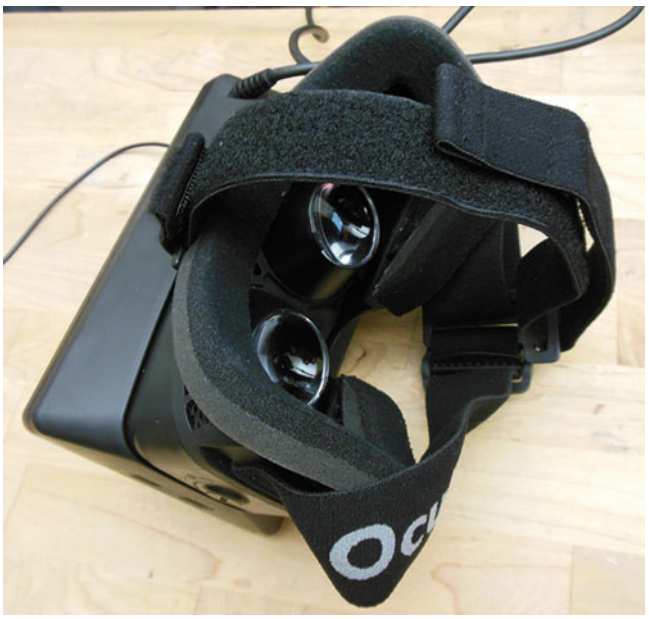

Fig. 2.5 The Oculus Rift virtual reality device

2.2.3 Information Visualization

In order to effectively communicate the information contained in the model described above to the glovebox operator, an Oculus Rift virtual reality device, shown in Fig. 2.5, was used. This device has the capability to display virtual information, such as a point cloud representation of the nuclear criticality model shown in Fig. 2.4.

2.2.4 Testing Motivation

To be considered a viable system for preventing nuclear criticality violations, the IEWCS must be reliable. Part of its reliability is determined by how well the system can accurately and repeatedly identify nuclear containers. The accuracy of the nuclear criticality safety models that are attached virtually to each container relies upon how well the container can be located in the glovebox. Therefore, an experiment was designed to find the accuracy and precision with which the centroid of a container can be inferred from a point cloud representing the container's surface. Similarly, identifying dimensions is important to differentiating between nuclear containers within the same glovebox. Therefore, the experimental procedure also included an analysis of the accuracy and repeatability of the radius calculated from the point clouds of the test containers.

2.2.5 *Physical Setup*

The data necessary for analyzing the accuracy and repeatability of the system was gathered by designing a controlled experimental setup. This setup consisted of a grid composed of 105 squares with 10 cm side lengths. Four Kinect sensor were placed at various locations around the grid. The test setup and sensor array is shown in Fig. 2.6, and Table 2.1 gives the locations of each of the four Kinect sensors with respect to the global reference frame denoted on the grid.

Four containers of varying size and shape were used as test objects. These containers are shown in Fig. 2.7, and a summary of their dimensions is given in Table 2.2. As seen in the image, each of the containers was wrapped in stiff brown paper to eliminate any variations caused by differing surface properties.

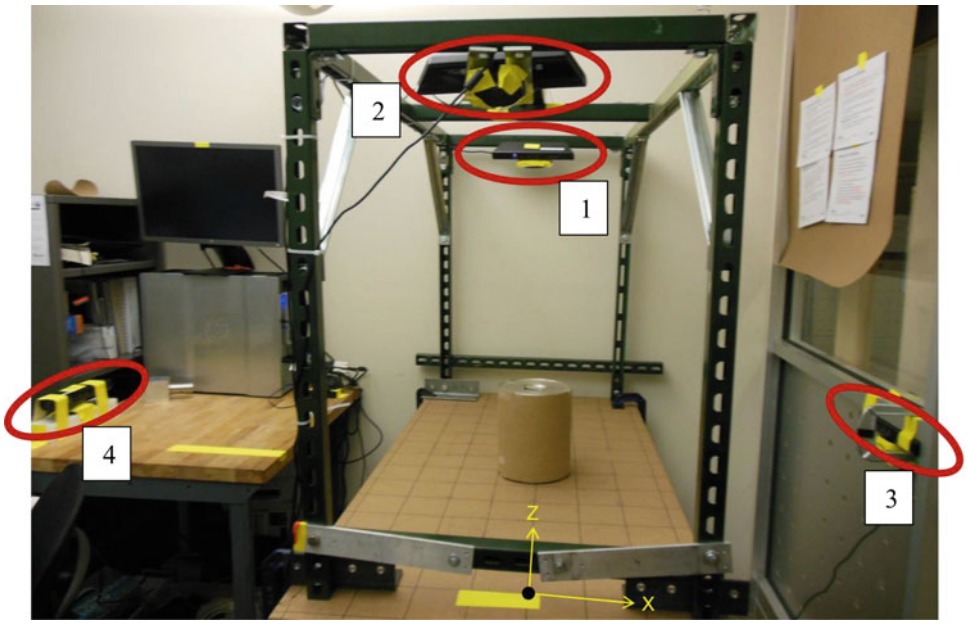

Fig. 2.6 Experimental setup showing grid, global reference frame origin and axes, Kinect array, and test container

Table 2.1 Position and orientation of Kinect Sensors with respect to global reference frame

	X (m)	Y (m)	Z (m)	Rotation (degrees)
Kinect 1	0	−0.9	1.3	−45
Kinect 2	0	−0.9	0	−45
Kinect 3	0.8	−0.1	0.6	0
Kinect 4	−1.4	−0.1	0.8	0

Fig. 2.7 Test containers

Table 2.2 Dimensions of test cylinders

	Radius (m)	Height (m)
Container 1	0.104	0.261
Container 2	0.094	0.233
Container 3	0.076	0.180
Container 4	0.076	0.110

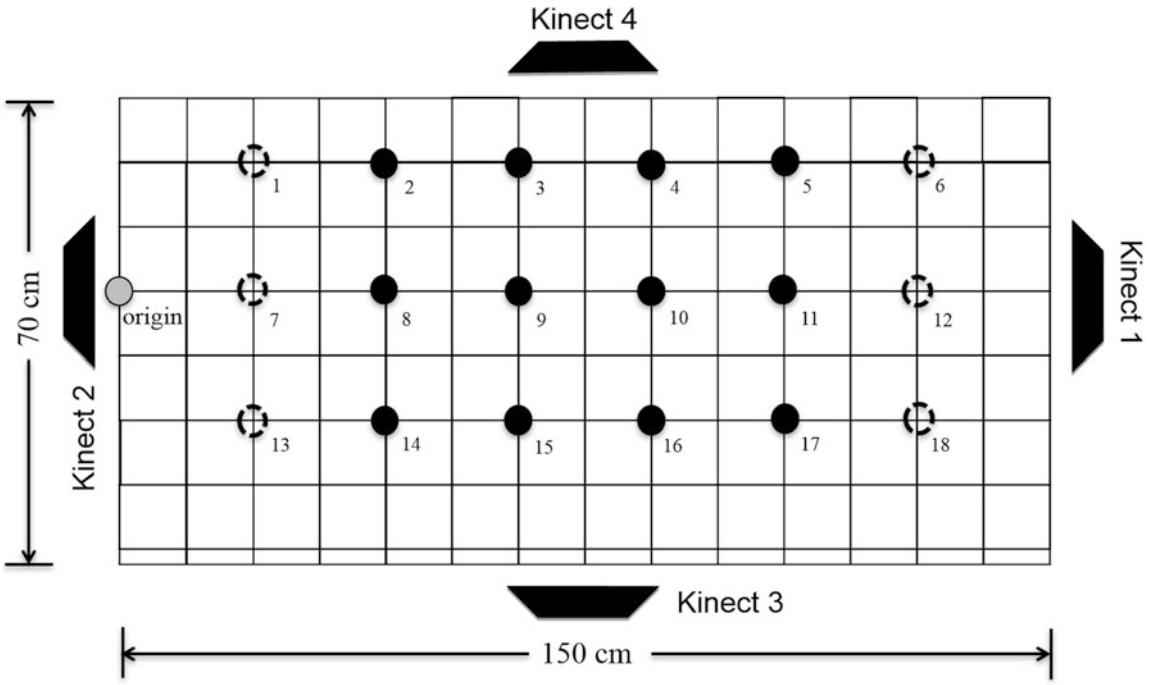

Fig. 2.8 Schematic of test locations

2.2.6 Data Collection

The accuracy and repeatability of the sensing system was found by measuring each of the four containers at all 18 locations highlighted in Fig. 2.8. Approximately 25 point clouds were collected for each container at each of the locations in Fig. 2.8 denoted by a solid circle. Preliminary testing showed that containers located at the positions denoted by a dashed circle were too close to the edge of the grid and were not able to be detected by the sensor array. Therefore, these positions were omitted from our analysis. Each point cloud dataset contained X, Y, and Z coordinates for each observable point on the surface of the cylinder in addition to a calculation of the cylinder's 3D centroid and radius.

2.3 Data Analysis and Results

For the IEWCS to be reliable, it must be able to tell the type and location of each container of interest within the glovebox. To quantify its performance of these requirements, an analysis of the repeatability and accuracy of centroid detection and radius identification was performed.

2.3.1 Cylinder Model Detection

The cylinder segmentation algorithm only produces quality results when the input point cloud contains a fairly complete surface of a cylinder. In many of the 18 total measurement locations, the cylinder could not be detected. Figures 2.9 and 2.10 show how often each cylinder was identified at each location, with and without the use of downsampling. Downsampling is a PCL function that drastically reduces the number of points in a point cloud while maintaining its general shape, reducing computational time greatly. However, it seems that the cylinder segmentation code exhibits higher errors on downsampled data, and does not successfully identify a cylinder nearly as often. Due to this, it was determined not to use downsampled data for any of the following analysis, despite its 12-fold reduction in computation time.

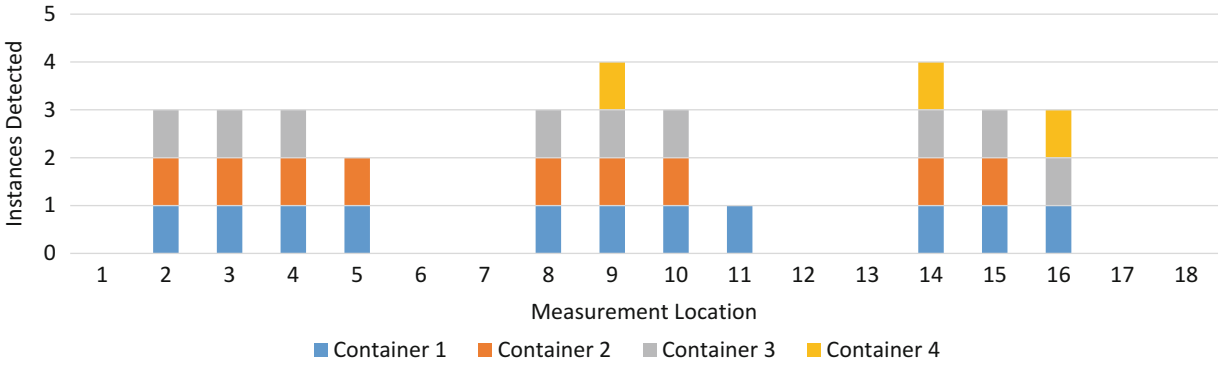

Fig. 2.9 Container detection without downsampling

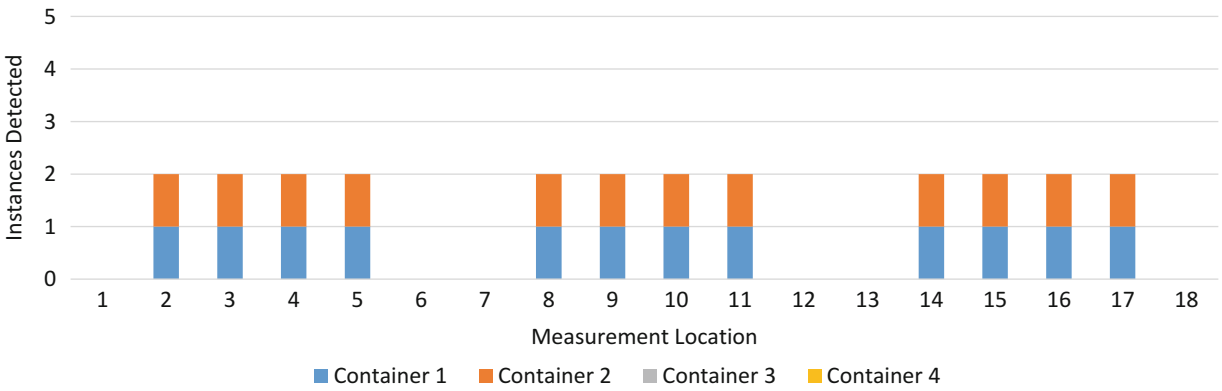

Fig. 2.10 Container detection with downsampling

2.3.2 Position Repeatability

Figure 2.11 shows the mean repeatability of the centroid calculation for each cylinder at each measurement location. Note that for all of the following plots, measurements 12 and 13 of Container 3 at Location 2 were considered outliers and removed from the analysis. Excluding these outliers, all observable locations exhibit a repeatability error of less than 0.4 cm, and all locations but three are less than 0.2 cm. These results are encouraging, as it gives great potential for the accuracy of the system to be very high with proper calibration.

2.3.3 Position Accuracy

Figure 2.12 show the accuracy of centroid calculating algorithm, defined as the distance from the nominal position of the container to the location the algorithm produced. The trends in accuracy seem to be much more a function of position than cylinder size. This is likely due to the Kinect sensor array not having a uniform view of the workspace. Locations 1–6 are better centered between Kinects 3 and 4, giving a more complete view of the container. Likewise, Locations 13–18 are too close to Kinect 3 to be observed well, and suffer the greatest accuracy errors. When part of a container's point cloud is missing, the centroid of the point cloud is weighted towards the completed section. These systematic errors are well observed in Fig. 2.13. The black circles show the nominal position of each container, while the arrows point to the location where the container was measured. A systematic error in the direction of the + X-axis as well as a tendency towards the center of the grid are both observable. Also, the manual refinement of the transformation matrices was imperfect, and directly affected the accuracy of the system at all locations.

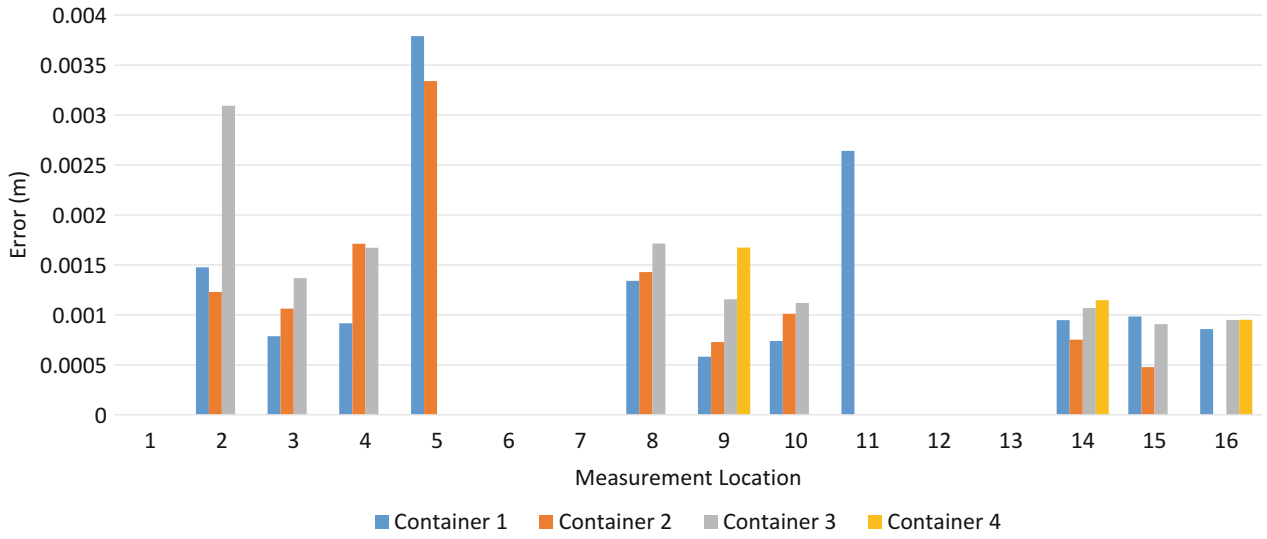

Fig. 2.11 Mean position repeatability error

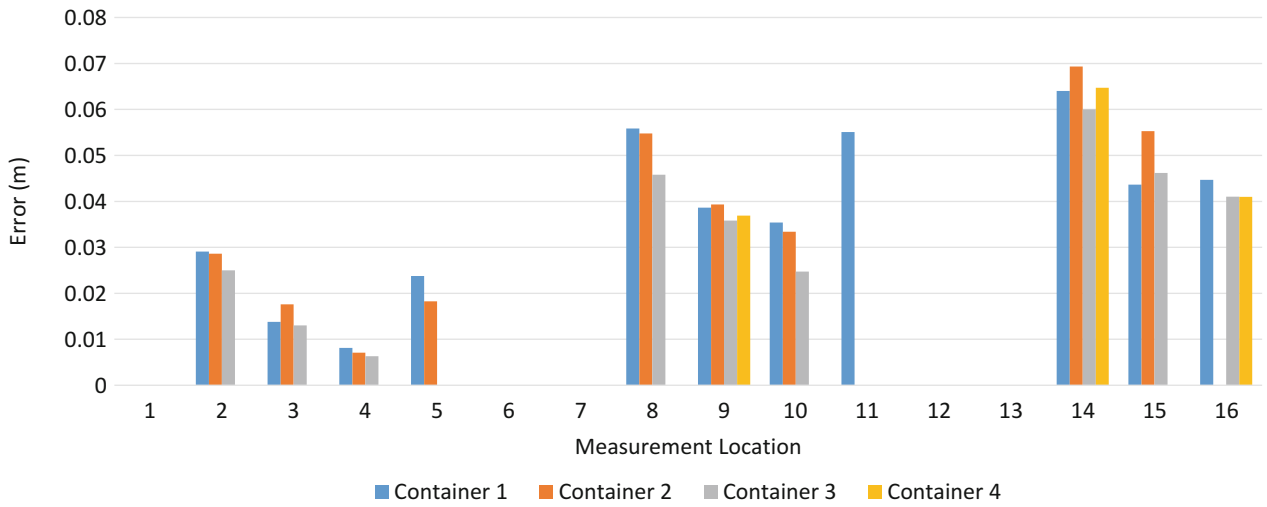

Fig. 2.12 Mean position accuracy error

2.3.4 Radius Repeatability

Radius identification is essential to differentiating between containers, and these results were quite promising in that regard. Figure 2.14 shows that the repeatability of radius identification was less than 0.1 cm in all locations but two. Further analysis was conducted to find what confidence could be assigned to differentiating between Containers 1 and 2, the two most similar containers that do not have identical radii. Figure 2.15 shows all measurements made from Containers 1, 2, and 3 at Location 10 in blue, green, and red, respectively. Each dot shows an individual measurement, the dotted line shows the mean value, the solid lines show plus or minus three standard deviations from the mean. It was determined that even at the most unreliable location, the means of Container 1 and Container 2 measurements are at least 3.6 standard deviations apart. Assuming a standard normal distribution of the data, this would suggest a 99.985 % confidence that the two containers would be successfully distinguished from each other.

Fig. 2.13 Position accuracy

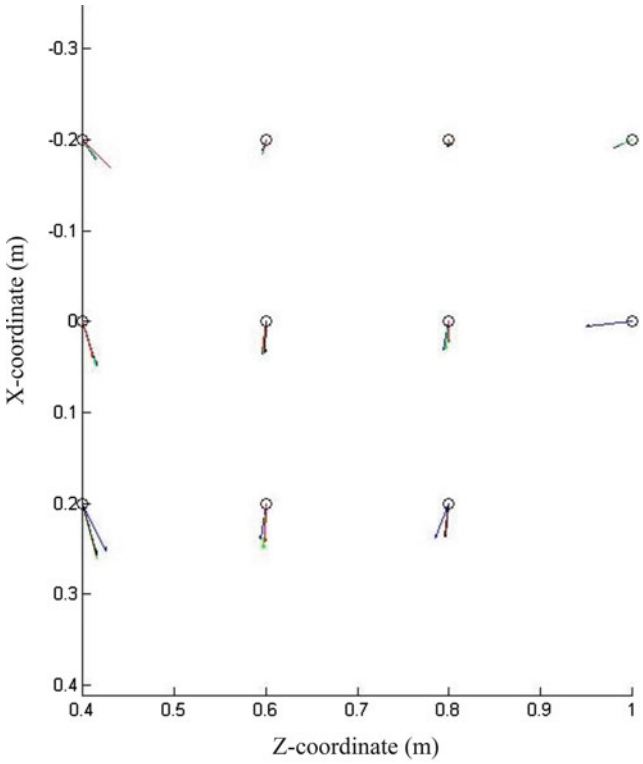

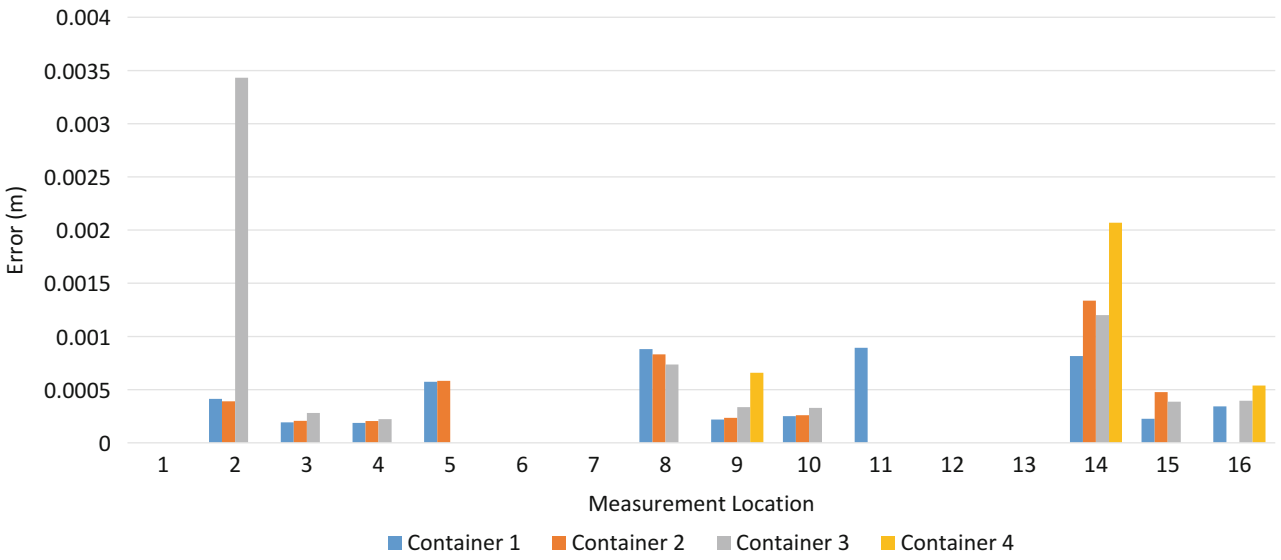

Fig. 2.14 Mean radial repeatability error

2.3.5 Radius Accuracy

Similarly to the position data, radius identification exhibited noticeably higher accuracy error than repeatability, and likely for many of the same reasons. As seen in Fig. 2.16, all locations but two have an accuracy error lower than 0.7 cm. This seems to be an acceptable value, as the difference between radii of Containers 1 and 2 is 0.9 cm.

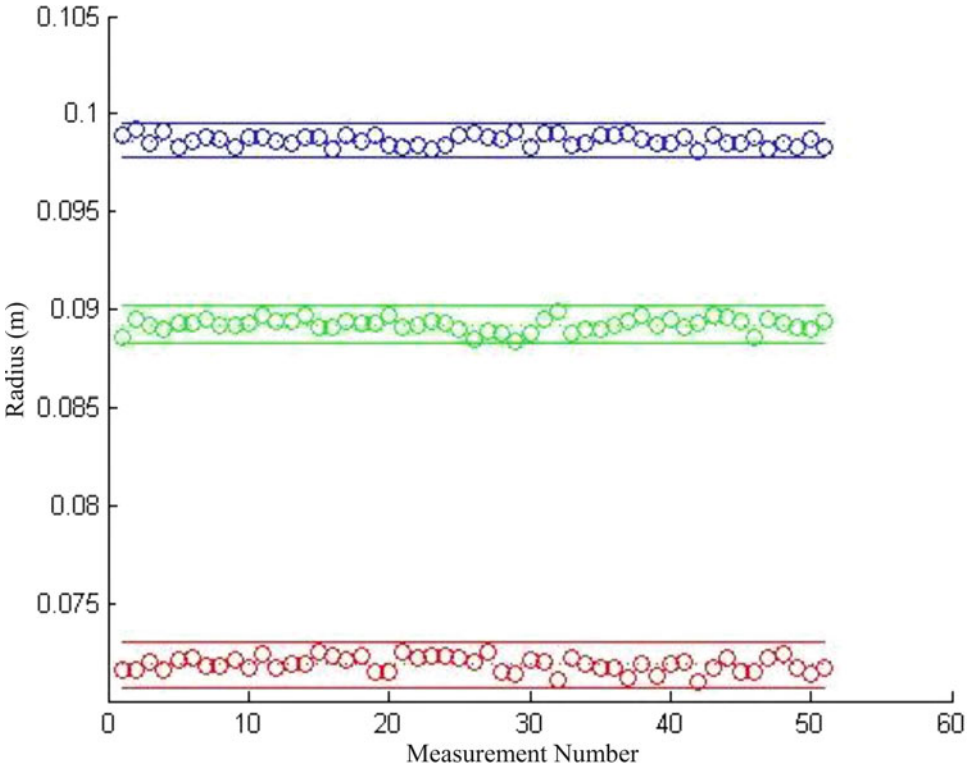

Fig. 2.15 Location radius deviation

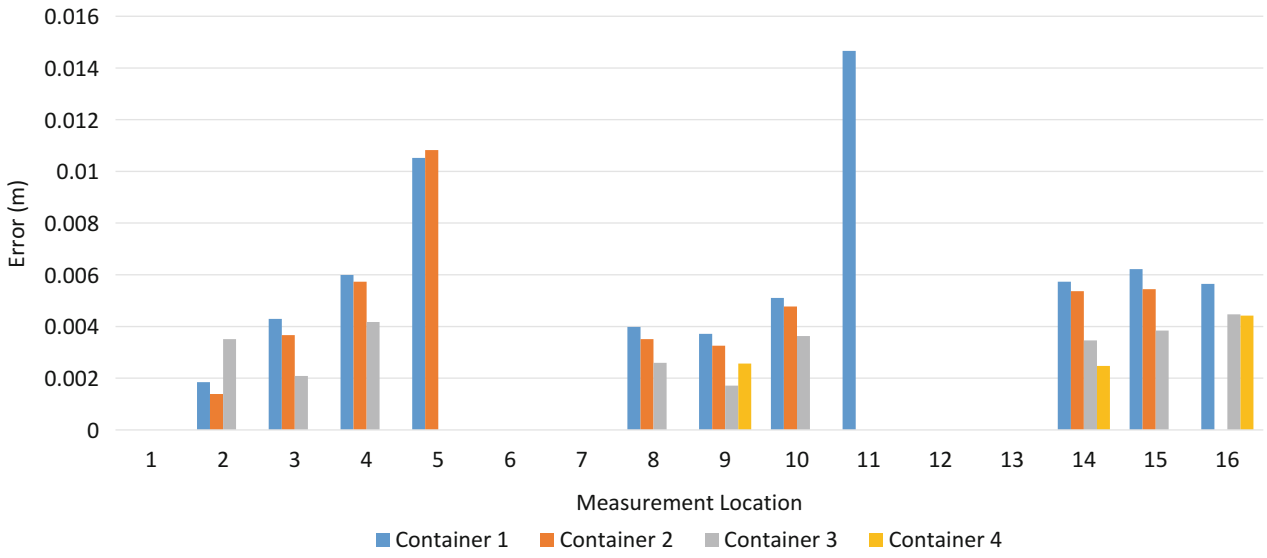

Fig. 2.16 Mean radial accuracy error

2.4 Conclusions

Even at an early stage, the IEWCS system proved very promising as a human-user interface for improving the safety and efficiency of glovebox operations. It's been shown that if the 3D camera array has a good view of the workspace, the measurement repeatability is satisfactorily high, and with a more robust calibration and centroid calculation algorithm, the accuracy could quickly be raised to acceptable levels as well. The overlaid criticality regulation model performed exactly as intended with a much oversimplified nuclear model, and provides a great framework for a more rigorous model to be implemented in the future. Lastly, the virtual reality interface showed promise as an effective method of delivering this modeling information to the user, and made many of the preparations necessary for a later augmented reality system.

Acknowledgements The authors would like to thank Chuck Farrar and André Green of the Los Alamos Engineering Institute. They would also like to thank the Los Alamos National Laboratory Seaborg Institute for their support.

References

1. Photo courtesy of the Advanced Studies Institute at Los Alamos National Lab. [Interview]
2. Sansoni G, Trebeschi M, Docchio F (2009) State-of-the-art and applications of 3D-imaging sensors in industry, cultural heritage, medicine, and criminal investigation. Sensors 9(1):568–601
3. Pennington R (2001) Signs of marketing in virtual reality. J Interact Advert, 2(1)
4. Bergeron B (2003) Virtual reality applications in clinical medicine. J Med Pract Manage 18(4):211–215
5. As Low As Reasonably Achievable (ALARA) Planning: Human Simulation for Radiation Safety Programs, Siemens PLM Software (2014) [Online]. Available: www.plm.automations.siemens.com/en_us/energy-utilities/alara-planning. Accessed 24 June 2014
6. Suganya S, Raajan N (2011) Augmented reality-landmark estimation. In: Recent Advancements in Electrical, Electronics and Control Engineering, Sivakasi
7. Virtual Reality: Definition and Requirements, NASA, [Online]. Available: www.nas.nasa.gov/Software/VWT/vr.html. Accessed 24 June 2014
8. Navab N, Blum T, Wang L, Okur A, Wendler T (2012) First seployments of augmented reality in operating rooms. Computer 45(7):48–55
9. Henderson S, Feiner S (2011) Augmented reality in the psychomotor phase of a procedural task. In: IEEE international symposium on mixed and augmented reality, Basel.
10. Hirotake I (2010) Virtual reality: fundamentals and nuclear related applications. Nucl Saf Simul 1(1)
11. Michel K, Elfman E, Dickens B, Green J, Hypes P (2011) Virtual reality technology applied to planning and design challenges in nuclear safeguards. In: Institute of nuclear materials management 52nd annual meeting, Palm Desert
12. ROS.org, [Online]. Available: wiki.ros.org. Accessed 1 June 2014
13. “Point Cloud Library,” Open Perception, [Online]. Available: http://pointclouds.org/. Accessed July 2014
14. “wiki.rog.org/ar_kinect,” 31 March 2013. [Online]. Available: http://wiki.ros.org/ar_kinect. [Accessed 1 July 2014]

Chapter 3
Practical Calibration Techniques for the Modal Impact Hammer

Tong Wang, Ozan Celik, F. Necati Catbas, and Lingmi Zhang

Abstract Modal impact hammer comprised of a force transducer, a hammer body and different impact tips, is widely used in structural dynamic testing. Users might usually overlook the sensitivity of the impact hammer since it has no influence on the estimation of modal frequency, damping, and mode shape in a Multiple Reference Impact Test (MRIT). However, for the reason of accurate measurement and analysis for estimating the modal scaling factor or measuring the inertial mass of the structure, the calibration process has to be performed in advance. For the majority of off-the-shelf impact hammers, the force transducer cannot be detached. Moreover, the sensitivity of the integrated force transducer is not identical with the hammer because the force is transferred from the sensor to the structure via the impact tip. Therefore, the calibration method for common force transducers is not suitable for the impact hammer. In this paper, on the basis of drop calibration, two practical methods using an accelerometer and a load cell are presented respectively to calibrate the impact hammer and findings are compared with each other. The influence of different impact tips to the sensitivity of the hammer is also discussed.

Keywords Impact calibration • Drop calibration • Modal impact hammer • Accelerometer • Load cell

3.1 Introduction

Modal impact hammer is a commonly used excitation device which can apply a nearly-constant impulse force over a broad frequency range. Therefore all the resonances in that range of tested structures can be excited by simple strikes. The main sensing element of an impact hammer is actually a force sensor, which is mounted on the striking end of the hammer head. Due to the reliability consideration, the sensor is always fixed to the hammer with epoxy adhesive [1] and cannot be disassembled by the user. A variety of impact tips of different stiffness can easily be installed at the striking end of the hammer so as to protect the force sensor from possible damages and to provide different excitation frequency ranges for testing.

In the multiple reference impact test (MRIT) [2], the most widely applied modal testing technique using an impact hammer, one or several accelerometers are fixed at some reference locations and the hammer is moved from one location to another in order to impact the structure. For each impact location, a set of single-input and multiple-output (SIMO) frequency response functions (FRF) can be obtained. According to the Maxwell's reciprocity theorem, a set of multiple-input (equal to the number of reference accelerometers) and multiple-output (equal to the number of impact locations) FRFs can be assembled by combining all the SIMO FRFs that were acquired from that series of hammer-impact locations. The sensitivity of the impact hammer will not affect the identification of modal frequencies, damping ratios, and mode shapes of the tested structure. Mostly, users would prefer to utilize the nominal sensitivity of the hammer which is provided by the manufacturer than to calibrate it by themselves. However, the current demand on the requirement of acquiring modal scaling factors in vast variety of engineering cases gives importance to the correct calibration of the impact hammer.

Calibrating an impact hammer is not an easy job. Firstly, the force on the crystals inside the sensor is less than the force that is acted upon the structure due to the tip being used between the test structure and the force sensor. As a result, the sensitivity of the hammer should be less than the force sensor. Secondly, the impact tips of various stiffness may influence

T. Wang (✉) • L. Zhang
State Key Laboratory of Mechanics and Control of Mechanical Structures, Nanjing University of Aeronautics and Astronautics, 29 Yudao Street, Nanjing 210016, China
e-mail: wt78@nuaa.edu.cn

O. Celik • F.N. Catbas
Department of Civil, Environmental and Construction Engineering, University of Central Florida, 4000 Central Florida Blvd, Orlando, FL 32816, USA

E.W. Sit (ed.), *Sensors and Instrumentation, Volume 5*, Conference Proceedings of the Society for Experimental Mechanics Series, DOI 10.1007/978-3-319-15212-7_3

the transmission of the force from the structure to the sensor because a part of the impact energy may be absorbed by the soft tip. Lastly, as mentioned above, the force sensor is generally integrated into the hammer, and cannot be taken apart except at the factory.

Then how can an impact hammer be calibrated practically? PCB, a famous sensor manufacturer, recommends to calibrate the hammer by hitting a freely-suspended mass instrumented with a reference accelerometer [3]. According to the Newton's second law of motion, the force experienced by the mass is simply the mass multiplied by the measured acceleration. Division of the peak output signal of the hammer by the mass times the peak acceleration gives the hammer sensitivity. Both the output time histories of the accelerometer and the impact hammer to be used in this calculation is recorded via an analyzer. Prior to the hammer calibration procedure, two things should be done primarily: (1) to simulate a freely-suspended mass setup and (2) to get the accurate sensitivity of the reference accelerometer.

The mass can be pendulously suspended or placed on a piece of foam rubber to approximately form the freely-suspended condition. A rotational motion seems difficult to avoid when a pendulously-suspended mass is hit by a hammer, and a big hammer in particular. The stiffness of the supporting foam rubber will reduce the precision of the hammer sensitivity. Besides, the mass cannot stand stably on a soft foam. The most common method of determining the sensitivity of an accelerometer is the back-to-back calibration technique. The accelerometer to be tested is mounted onto a previously calibrated standard reference accelerometer, and then the combined setup of accelerometers are connected to an exciter to sense the same acceleration. The sensitivity of the test accelerometer can easily be calculated by comparing the two outputs. Complicated devices, such as exciter, amplifier, signal generator and voltmeters are needed in this calibration procedure. Most importantly, a sensitivity-known accelerometer is still required.

In this paper, two practical easy-to-realize procedures for calibrating impact hammers are presented. An accelerometer and a load cell are utilized respectively as being reference sensors to calculate the sensitivity of the impact hammer. The real sensitivity of the reference sensors is obtained by the drop calibration method, which is an absolute calibration technique based on the earth's gravitational acceleration. The two procedures are compared with each other, and the influence of impact tips with different stiffness to the sensitivity of the hammer is also discussed.

3.2 Drop Calibration

Drop calibration technique utilizes the earth's gravitational field as reference, that is, a mass experiences a constant 1 g acceleration during free-fall period. The gravitational acceleration is a very good substitution of the standard reference accelerometer in a back-to-back calibration. If the output time history of the to-be-calibrated accelerometer is recorded, the sensitivity of test accelerometer can easily be calculated:

$$s = \frac{U_g - U_z}{g} \tag{3.1}$$

Where U_g is the output voltage during the sensor's free-fall, and U_z is the DC bias voltage when the sensor is in static state. Because a measurement system generally doesn't have the capacity of static response, the output signal in a real system exponentially decays during free-fall, which can be expressed with a time constant T [4]:

$$U(t) = U_g e^{-t/T} \tag{3.2}$$

A special device used for the calibration is called calibration fixture which is easy to design. During the process, a PCB calibration fixture (Model 9961C, shown in Fig. 3.1) is directly used to calibrate a PCB's accelerometer (Model 3801D3FB20G), which is mounted to the bottom of a rigid mass suspended on a taut line. The line is suspended from a junction fixed on the middle of an elastic cord. The line is relaxed by tapping on the junction, and then the mass-accelerometer system begins to fall freely for a brief instant. Subsequently, the line becomes taut again and the mass bounces after the free-fall ends.

A VXI data acquisition system with module VT1432A is utilized to catch the free-fall output signal by the trigger setting. The sampling rate is set to 3.2 kHz. A voltage step response is recorded by the data acquisition system. Figure 3.2 shows the output step response of the accelerometer in the process of calibration, in which the DC bias voltage and the exponential decay are very clearly demonstrated. U_g can be identified by fitting the decay part of the curve with an exponential function. The red bold line indicates the fitted curve. Then the sensitivity of the accelerometer can be obtained by Eq. 3.1. Three tests are performed to get a more accurate result. The final averaged sensitivity obtained from the calibration is 99.40 mv/g.

This technique can also be applied to calibrate a load cell in a similar fashion, but the gravitational acceleration needs to be transferred to force according to the Newton's second law. It can be achieved by mounting the load cell between the rigid

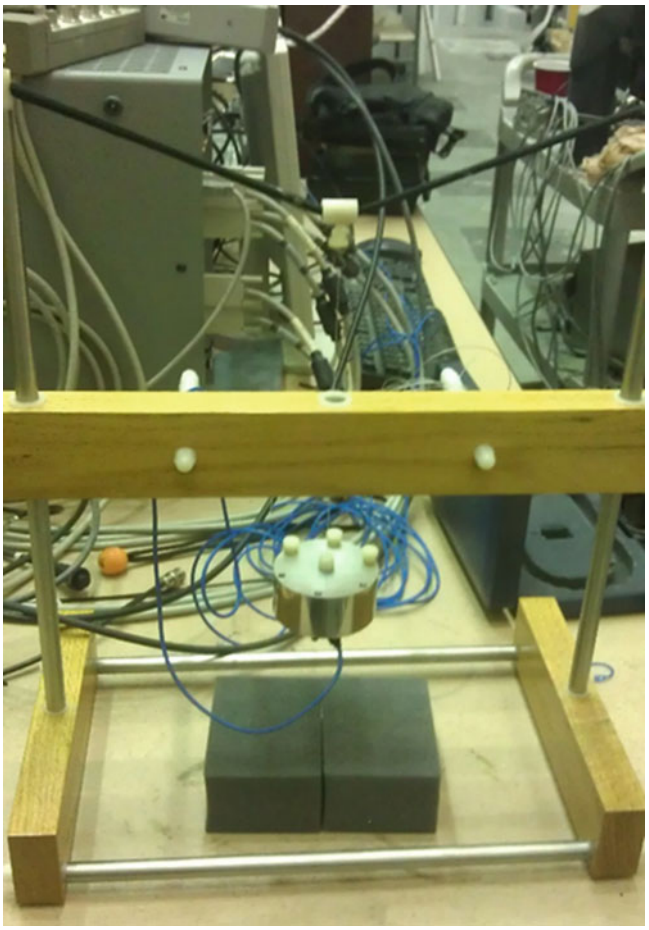

Fig. 3.1 Drop calibration of an accelerometer

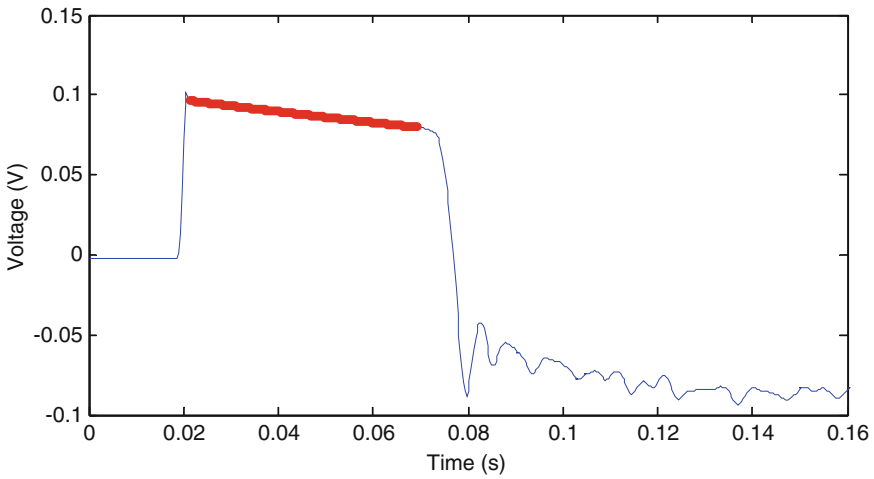

Fig. 3.2 Output signal of the accelerometer during the drop calibration

mass and the taut line (Fig. 3.3). At the static state the force applied on the load cell is equal to the weight of the mass, and this force is removed from the sensor when the mass experiences free-fall. Therefore the sensitivity of test load cell can be calculated by:

$$s = \frac{U_g - U_z}{Mg} \tag{3.3}$$

Figure 3.4 shows the output step response of a load cell (PCB Y208c02) in the process of calibration. U_g is estimated by interpolating the decay part of the curve with an exponential function, and the red bold line indicates the fitted curve. The final sensitivity obtained from the calibration is 10.51 mv/N after performing a three-time average.

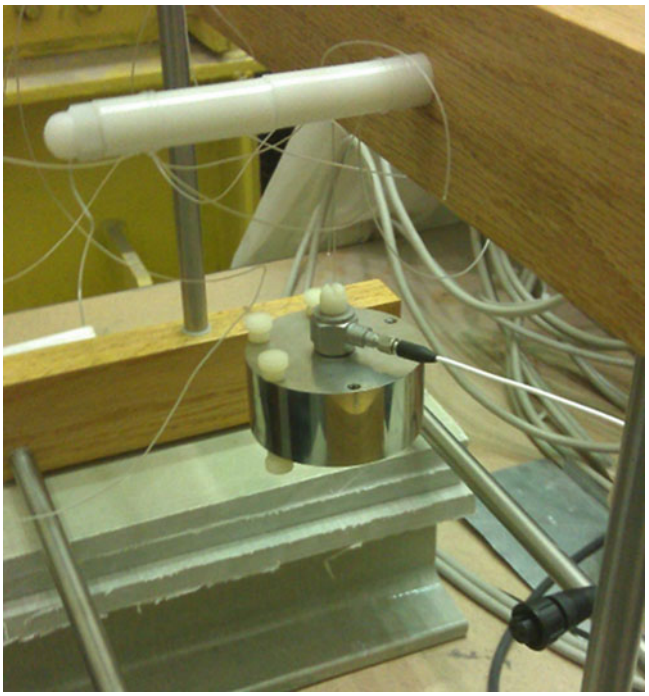

Fig. 3.3 Drop calibration of a load cell

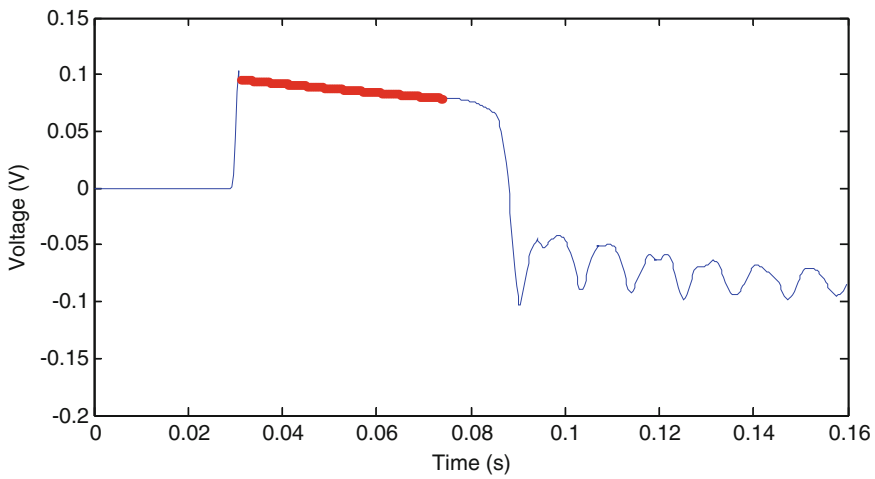

Fig. 3.4 Output signal of the load cell during the drop calibration

3.3 Impact Calibration

Based on the calibrated accelerometer and load cell, two methods are used to calibrate impact hammers. In the first method which is recommended by PCB, the accelerometer is taken as a reference sensor, and the model 9961C calibration fixture is adopted again to suspend a rigid mass freely. The calibrated accelerometer is mounted on one side of the rigid mass and an impact cap on the other side. The suspension is specially designed with the help of six nylon bolts and two lines (shown in Fig. 3.5a) to avoid the rotation motion of the mass. Hit the impact cap with the to-be-calibrated hammer, and record the time history of the two sensors. The hammer's sensitivity may be calculated by:

$$s = \frac{s_a U_{hp}}{M U_{ap}} \tag{3.4}$$

Where U_{hp} and U_{ap} are the peak voltage of hammer and accelerometer respectively, and s_{a} is the calibrated sensitivity of the accelerometer.

In the second method the load cell is taken as a reference sensor. The sensor is mounted on a steel strip, and then the steel strip is fixed on the smooth ground with some instant glue. An impact cap is installed on the top of the load cell to

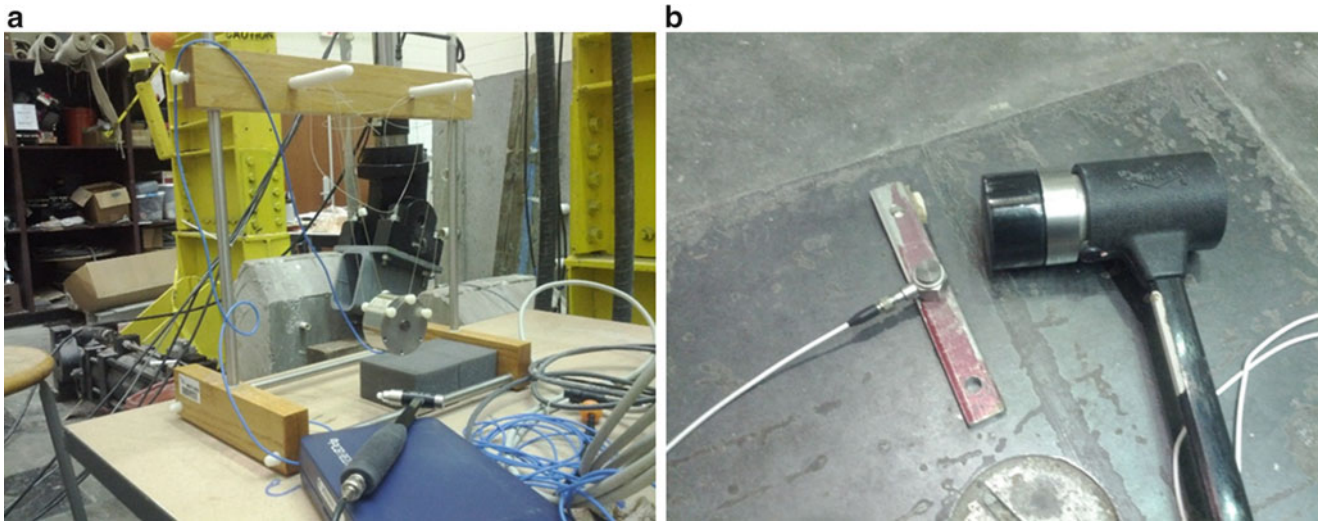

Fig. 3.5 Impact calibration with accelerometer (**a**) and load cell (**b**)

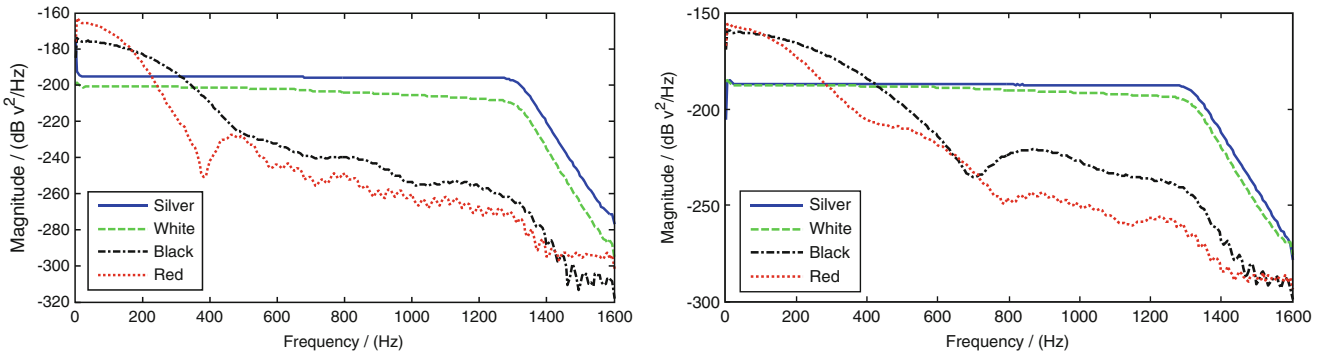

Fig. 3.6 Spectrum of force signal in impact calibration with accelerometer (*Left*) and load cell (*Right*), hammer 086c01

concentrate the hammer impact force. Hit the impact cap with the to-be-calibrated hammer, and record the time history of the two sensors. The hammer's sensitivity may be calculated by:

$$s = \frac{s_l U_{hp}}{U_{lp}} \tag{3.5}$$

Where U_{lp} and s_{l} are the peak voltage and the calibrated sensitivity of the load cell.

One small and one big hammers are set to be calibrated. The small one is PCB 086C01 with a nominal sensitivity of 11.2 mv/N, and the big one is PCB 086D20 with a nominal sensitivity of 0.23 mv/N. 086D20 is too big to be calibrated with the calibration fixture, so only the load cell calibration method is applied. The influence of different impact tips to the sensitivity of the hammer is also discussed.

Figure 3.6 shows the power spectral density functions of the output voltage of hammer 086c01 with its four tips in both of the accelerometer-referenced calibration and load cell-reference calibration. Both graphs clearly reveal the stiffness of the four tips by the different frequency ranges: silver > white > black > red.

In Figs. 3.7 and 3.8 the time histories of the reference sensor and the hammer are demonstrated. A problem can be found in the accelerometer-referenced calibration is that the output of the accelerometer and the hammer is not always synchronized. It may be caused by the suspension style of the rigid mass. Therefore the presented impact calibration method with a reference load cell seems more reliable. Another finding is that a stiffer tip is easier to cause the impact force to be oscillating.

The calculated sensitivity of hammer 086c01 is listed in Table 3.1. Three tests are performed for each case to get the average value. The dispersion of the accelerometer-referenced method is higher than the load cell-referenced method. The general tendency of the sensitivity with different tips is: higher stiffness higher sensitivity.

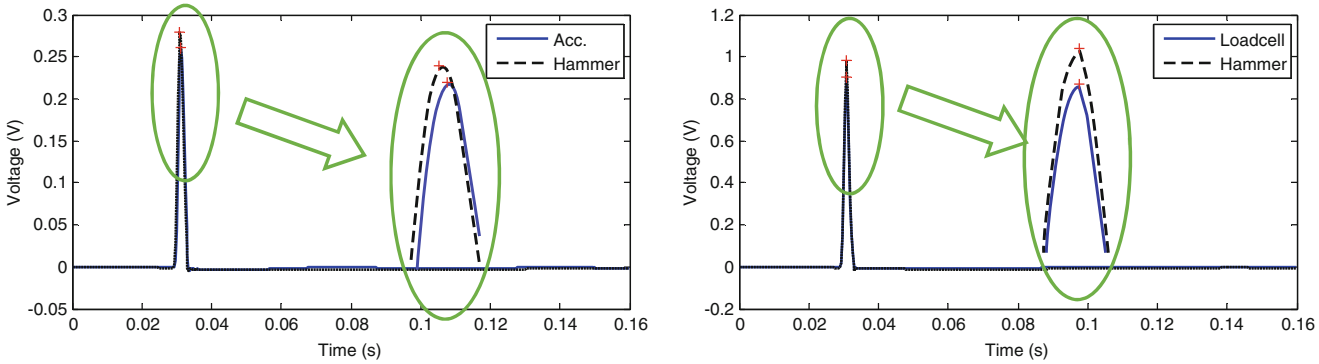

Fig. 3.7 Impact calibration with accelerometer (*Left*) and load cell (*Right*), hammer 086c01, black tip

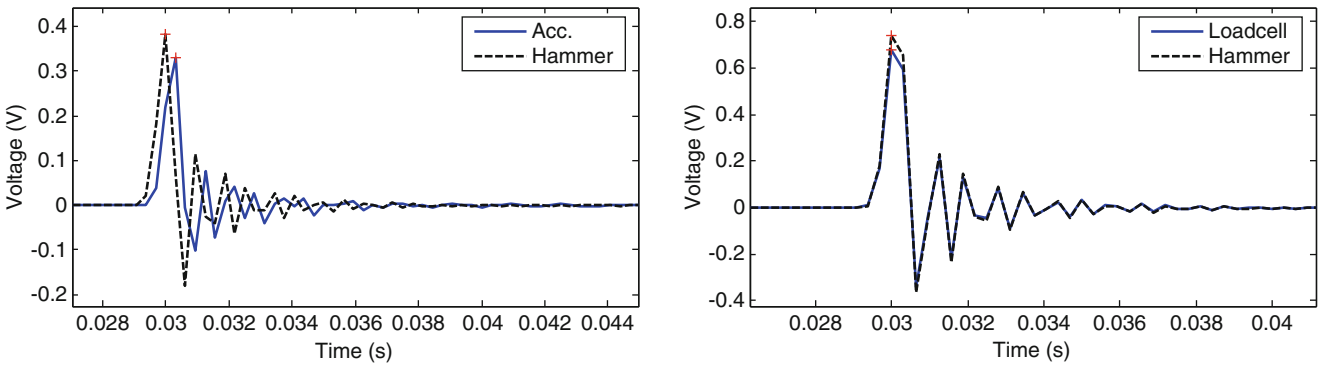

Fig. 3.8 Impact calibration with accelerometer (*Left*) and load cell (*Right*), hammer 086c01, silver tip

Table 3.1 Estimated sensitivity of hammer 086C01

	Accelerometer referenced				Load cell referenced			
Test	Silver	White	Black	Red	Silver	White	Black	Red
1	12.39	11.32	11.28	11.24	11.48	11.15	11.22	11.05
2	12.24	11.85	11.41	11.25	11.32	11.13	11.15	11.03
3	11.94	11.52	11.33	11.26	11.49	11.19	11.06	10.98
Average	12.19	11.56	11.34	11.25	11.43	11.16	11.14	11.02

Fig. 3.9 Spectrum of force signal in impact calibration with load cell, hammer 086D20

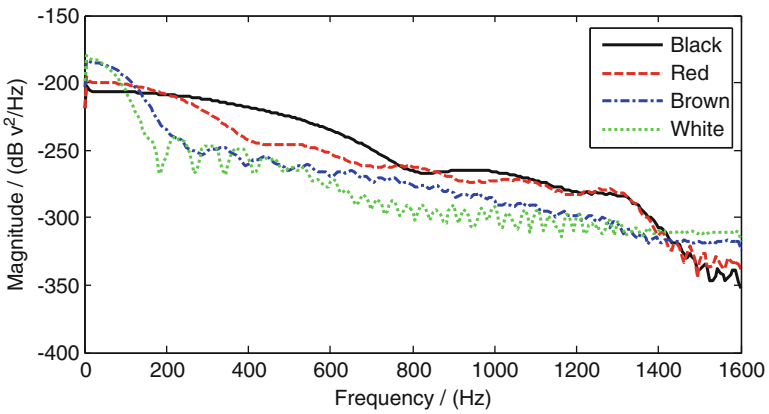

Figure 3.9 shows the stiffness of the four tips of big hammer 086D20: black > red > brown > white, and in Fig. 3.10 the time histories of the reference load cell and the hammer with different tips are showed.

Table 3.2 shows the identification result of hammer 086D20. It also reveals that the harder tip the higher sensitivity.

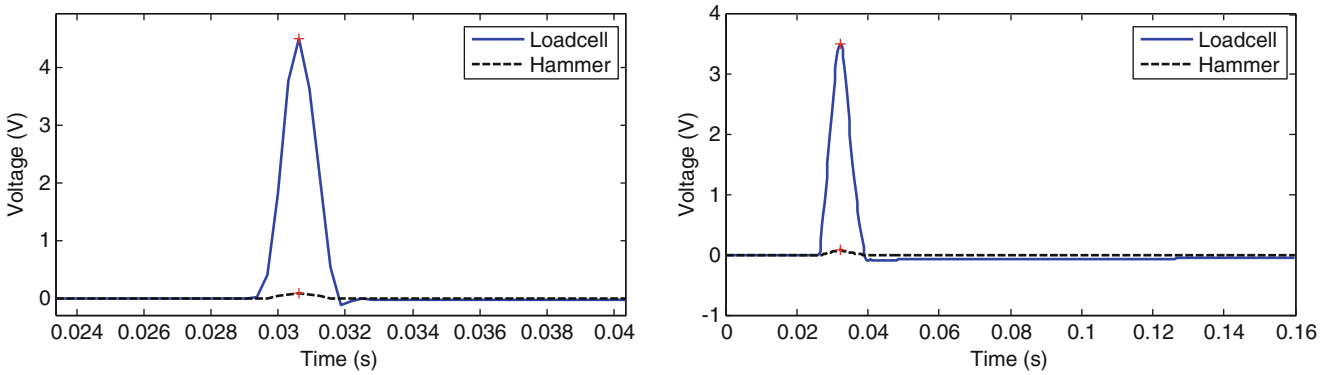

Fig. 3.10 Impact calibration with load cell and black (*Left*)/white (*Right*) tip, hammer 086D20

Table 3.2 Estimated sensitivity of hammer 086D20

	Load cell referenced			
Test	Black	Red	Brown	White
1	0.220	0.215	0.215	0.212
2	0.218	0.215	0.214	0.210
3	0.222	0.218	0.214	0.211
Average	0.220	0.216	0.214	0.211

3.4 Conclusion

An impact hammer can be reliably calibrated by the load cell referenced method. This method is easier and better than the accelerometer referenced method.

Different tips has different stiffness, which vary the hammer's sensitivity. A stiffer tip leads to a higher sensitivity.

Acknowledgement The support from Priority Academic Program Development of Jiangsu Higher Education Institutions (PAPD) is gratefully acknowledged.

References

1. PCB Piezotronics Inc. (2007) Model 086C01, Modally tuned impulse hammer installation and operating manual, PCB Group Inc., NY, USA
2. Tong Wang (2003) Study on multiple input/output frequency domain modal parameters identification of complex structures and its software implementation. Ph.D. dissertation, Nanjing University of Aeronautics and Astronautics
3. The Modal Shop Inc. (2007) Gravimetric calibration fixture user manual model 9961C. The Modal Shop Inc. Ohio, USA
4. Lingmi Zhang (1992) Vibration testing and dynamic analysis. Aviation Industry Press, China

Chapter 4
Frequency Tuning of a Wineglass Resonator Based on Acoustic Testing

Huinam Rhee, Sangjin Park, Sergii A. Sarapuloff, Soon Woo Han, and Jin Ho Park

Abstract A methodology to make a frequency tuning of an arbitrary quasi-axi-symmetric gyroscopic resonator oscillating at its low-frequency flexural modal pair has been proposed. For an ideal axi-symmetric resonator, such a structure has two degenerated modes with identical eigen frequencies and similar modal shapes distinguished by their angular orientation only. However, in reality, due to a small non-uniformity of the structure, the structure has two specific directions corresponding to slightly-different modal properties. Assuming only a mass imbalance, a mathematical formulation has been derived for the tuning by attaching point masses at specific locations. An ordinary wineglass has been chosen to verify this methodology. The principal axes and frequency mismatches were determined using acoustic signals of the free oscillations in air. Then, the magnitude of the point mass calculated by the proposed method has been applied for initial tuning of the imperfect shell resonator. The experimental result shows that the frequency mismatch has been reduced significantly, so, the validity of the proposed method has been verified. The proposed method can be generalized for a fine tuning of a gyroscopic resonator.

Keywords Resonator • Imperfect shell • Principal axis • HRG (Hemispherical Resonator Gyroscope) • Frequency tuning

4.1 Introduction

An HRG resonator has various manufacturing errors such as small overcutting and undercutting, asphericities, variations of thickness and of edge circle, eccentricities, etc. Even if a resonator has a perfectly-fabricated body without any manufacturing error, axial symmetry of its structure can be disturbed due to non-homogeneity of its materials. A really-perfect axi-symmetric resonator has two degenerated modes with identical eigen frequencies and two similar modal shapes distinguished only by their angular orientation. However, a resonator having quasi-axi-symmetric shape and properties has two specific principal axes with slightly-different modal properties. They are contributory causes for an output drift phenomenon in whole-angle regime of gyroscope's operation. In other words, a false output will be measured without any rotation input [1], and, therefore, an HRG resonator needs tuning processes to reach its potentially-high performance. If the resonator has enough small difference of modal properties, a small mismatch of operational modal frequencies can be tuned and stabilized electrically by a feedback and electronic means [2, 3]. Anyway, a mechanical tuning of a frequency mismatch has to be performed for such a case too to make the residual mismatch small enough to do its further electrical tuning. Tuning processes are largely-divided into a tuning of frequencies (inertia-stiffness) and a tuning of dissipation (a mismatch of Q-factors). Since Q-tuning is much more difficult than tuning of frequency, first of all, this paper deals with a study for tuning of "splitted" frequencies only. Actually, methodologies for both tuning processes were already introduced in 1989 [4]. However, the article [5] describes the methods for fine tuning of the frequencies and damping of the resonator performed in a vacuum chamber, using AFR (Amplitude Frequency Response) and PFR (Phase Frequency Response) characteristics of the resonator obtained for its forced oscillations.

H. Rhee (✉) • S. Park • S.A. Sarapuloff
Department of Mechanical & Aerospace Engineering, Sunchon National University, 255 Jungang-ro, Sunchon, Jeonnam 540-742, Republic of Korea
e-mail: hnrhee@sunchon.ac.kr; sergii.sarapuloff@gmail.com

S.W. Han • J.H. Park
Convergence Technology Development, Korea Atomic Energy Research Institute, 989-111 Dae-deog-dae-ro, Yusung-ku, Daejeon 305-353, Republic of Korea

E.W. Sit (ed.), *Sensors and Instrumentation, Volume 5*, Conference Proceedings of the Society for Experimental Mechanics Series, DOI 10.1007/978-3-319-15212-7_4

In the present paper, a simpler methodology to make a frequency tuning of an arbitrary quasi-axi-symmetric resonator, oscillating at its low-frequency flexural modal pair, has been proposed. Even though, a mismatch of frequencies is caused by imbalances of both inertia and stiffness. This paper assumes that only inertia imbalance makes mismatch of the frequencies, and a mathematical formulation is derived for the tuning by attaching point masses at specific locations. In order to verify the proposed methodology, an ordinary wineglass was chosen instead of a high-price HRG resonator. Through acoustic testing to the wineglass in air, dynamic characteristics and positions of principal axes of a wineglass were identified for frequency tuning. Then, when the magnitude of the mass for the tuning was determined through the proposed method, the effectiveness of the proposed method was observed by attaching the calculated mass at principal axes of the wineglass.

4.2 Methodology for Frequency Tuning

First of all, let us follow methodology is based on the papers [4, 6, 7]. Let us suppose that a variation of frequency mismatch of the imperfect hemispherical resonator can be done by a number of point masses only without any influence of them on stiffness and damping. Considering the hemispherical resonator with a point mass m_1 at located point $P_1\ (\theta_1,\ \varphi_1)$ in Fig. 4.1, the total mass of the hemispherical resonator M_{total} is

$$M_{total} = M_0 + \int_S m_1\ h\ \delta_{P_1}\ (\theta, \varphi)\ \ dS, \tag{4.1}$$

where M_0 is a nominal mass, $\delta_{P_1}\ (\theta, \varphi)$ is Dirac's delta-function with its carrier at a point P_1. Velocities of mid-surface are defined as follows:

$$\begin{aligned} \dot{u}_n\ (\theta, \varphi, t) &= U_n\ (\theta)\ [\dot{x}(t) \cos\ (n\varphi) + \dot{y}(t) \sin\ (n\varphi)]\ , \\ \dot{v}_n\ (\theta, \varphi, t) &= V_n\ (\theta)\ [\dot{x}(t) \sin\ (n\varphi) - \dot{y}(t) cos\ (n\varphi)]\ , \\ \dot{w}_n\ (\theta, \varphi, t) &= W_n\ (\theta)\ [\dot{x}(t) \cos\ (n\varphi) + \dot{y}(t) \sin\ (n\varphi)]\ . \end{aligned} \tag{4.2}$$

In order to calculate the frequency of a hemispherical resonator for its n-th flexural mode, one can calculate the effective mass from expression of shell's kinetic energy using expressions (4.2), and obtain

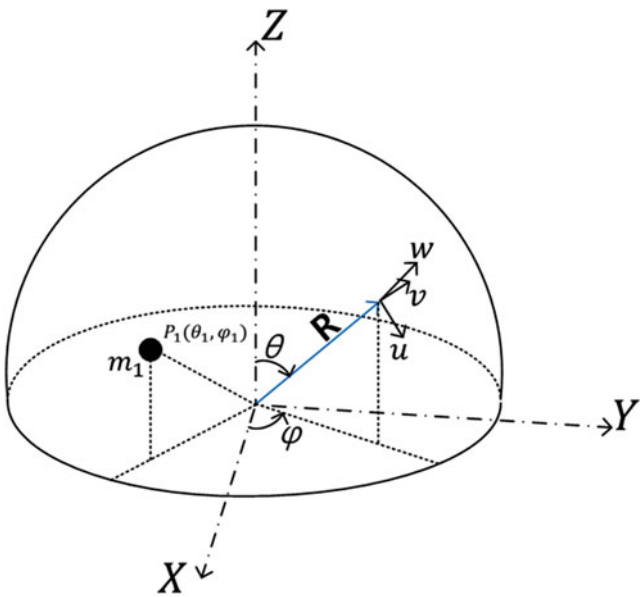

Fig. 4.1 A hemispherical resonator with an attached point mass

$$
\begin{aligned}
m_{\text{effective}} &= M_0 \xi_n(\theta,\varphi) + m_1 \zeta_n(\theta_1,\ \varphi_1),\\
\xi_n(\theta,\varphi) &= \frac{1}{2\pi}\int_0^{2\pi}\int_0^{\pi/2}\left(\dot{u}_n(\theta,\varphi)^2 + \dot{v}_n(\theta,\varphi)^2 + \dot{w}_n(\theta,\varphi)^2\right)\sin\theta \mathrm{d}\theta d\varphi,\\
\zeta_n(\theta_1,\ \varphi_1) &= \frac{1}{2\pi}\int_0^{2\pi}\int_0^{\frac{\pi}{2}}\delta_{P_1}(\theta,\varphi)\left[\dot{u}_n(\theta,\varphi)^2 + \dot{v}_n(\theta,\varphi)^2 + \dot{w}_n(\theta,\varphi)^2\right]\sin\theta \mathrm{d}\theta d\varphi\\
&= \frac{1}{2\pi}\left[\dot{u}_n(\theta_1,\ \varphi_1)^2 + \dot{v}_n(\theta_1,\ \varphi_1)^2 + \dot{w}_n(\theta_1,\ \varphi_1)^2\right]\sin\theta_1.
\end{aligned}
\tag{4.3}
$$

$\xi_n(\theta,\varphi)$ and $\zeta_n(\theta_1,\ \varphi_1)$ tell the contribution to effective mass as non-dimensional coefficients. Especially, $\zeta_n(\theta_1,\ \varphi_1)$ in expression (4.3) is determined by definition of Dirac's delta function and contribution to effective mass can be varied depending on position $(\theta_1,\ \varphi_1)$ of point mass. Therefore, a point mass at principal axes ($\varphi_1 = 0$ or $\frac{\pi}{4}$) of a higher component of n-th flexural mode on the equator ($\theta_1 = \frac{\pi}{2}$) is the best for the effective balancing. Eigen frequency of the hemispherical resonator is expressed as follows:

$$
{\omega_n}^2 = \frac{a_{\text{effective}}}{m_{\text{effective}}} \approx \frac{a_{\text{effective}}}{M_0\,\xi(\theta)}\left(1 - \frac{m_1\,\zeta_n(\theta_1,\ \varphi_1)}{M_0\,\xi_n(\theta,\varphi)}\right) = {\omega_0}^2\left(1 - \frac{m_1\,\zeta_n(\theta_1,\ \varphi_1)}{M_0\,\xi_n(\theta,\varphi)}\right),
\tag{4.4}
$$

where ω_0 is a nominal frequency. Thus, a positive point mass m_1 makes a decrease in the frequency. In other words, if a small magnitude of frequency mismatch $\triangle\omega$ is known, a magnitude of mass for frequency tuning $m_1$can be determined by expression (4.5) derived from expression (4.4)

$$
\frac{m_1\,\zeta_n(\theta_1,\ \varphi_1)}{M_0\,\xi_n(\theta,\varphi)} = \frac{\Delta\omega}{\omega_0}.
\tag{4.5}
$$

If the calculated point mass is attached or trimmed at principal axes of the modal pair, the eigen frequencies of the structure are tuned. In addition, since effective mass is less sensitive to a point mass outside of the principal axes or equator of the resonator, a finer tuning is possible and more than two vibrational modes can be tuned simultaneously. In this paper the case of just one point mass for mass balancing is described, but, for a more general case, this methodology can enough deal with mass balancing by a number of point mass by expanding m_1 to a concept of $\sum_{k=1}^{\infty} m_k$ and point stiffness too.

4.3 Experimental Verification

An ordinary wineglass is chosen for experimental verification instead of usage of a high-price HRG resonator. The wineglass mass is about 64 g without its stem, and its frequencies are 501.5 (ω_{2_first}) and 513.1 Hz ($\omega_{2-second}$) for the 2nd flexural modal pair. Therefore, the frequency mismatch between (ω_{2_first}) mode and ($\omega_{2-second}$) mode is 11.6 Hz as shown in Fig. 4.2a. Then, principal axes of the flexural modal pair were found through the methodology proposed by Rhee et al. [7]. The principal axis of (ω_{2_first}) mode is positioned at approximately 11.5°±0.5° from the readout axis of the 1st microphone. Thus, the principal axis of ($\omega_{2-second}$) mode is positioned approximately at 56.5°, because these two principal axes of the n-th flexural modal pair have phase difference of $\frac{\pi}{2n}$.

By using expression (4.5), the point mass was determined 1.34 g when it is attached at the principal axis of ($\omega_{2-second}$) mode. Then, the point mass was divided into two or four pieces, and attached at opposite pair locations not to change the center of gravity as shown in Fig. 4.2b.

Figure 4.3 shows that $\omega_{2-second}$ mode frequency decreases, and at the same time ω_{2_first} mode frequency decreases less by attaching the point mass to the resonator. Small decrease of ω_{2_first} mode frequency can be caused by two reasons. First, the attached masses have finite sizes, therefore, they are not exactly attached at the principal axis. Second, the attached point mass has an influence on the tangential motion as well as the radial motion, therefore, the tuning mass at the principal axis of $\omega_{2-second}$ mode affects the effective mass of ω_{2_first} mode. After attaching of two 0.32 g-masses (total 0.64 g), the frequency mismatch decreased from 11.6 to 4.5 Hz. Then, by attaching two more 0.32 g-masses (total 1.29 g), the frequency mismatch was reduced to 2.5 Hz, however, $\omega_{2-second}$ was even smaller than ω_{2_first}. Assuming the natural frequency linearly decreases by the tuning mass, total 1.06 g mass is expected to make the frequency mismatch becomes zero. This amount of mass is 20.9 % smaller than the analytical result (1.34 g). This discrepancy can be explained as follows: First the theoretical formulation assumes the resonator is a complete hemisphere and has no stem while the wineglass actually has a stem and its shape is not a hemisphere. Second, the mass of the resonator cannot be clearly defined because it is connected with a stem.

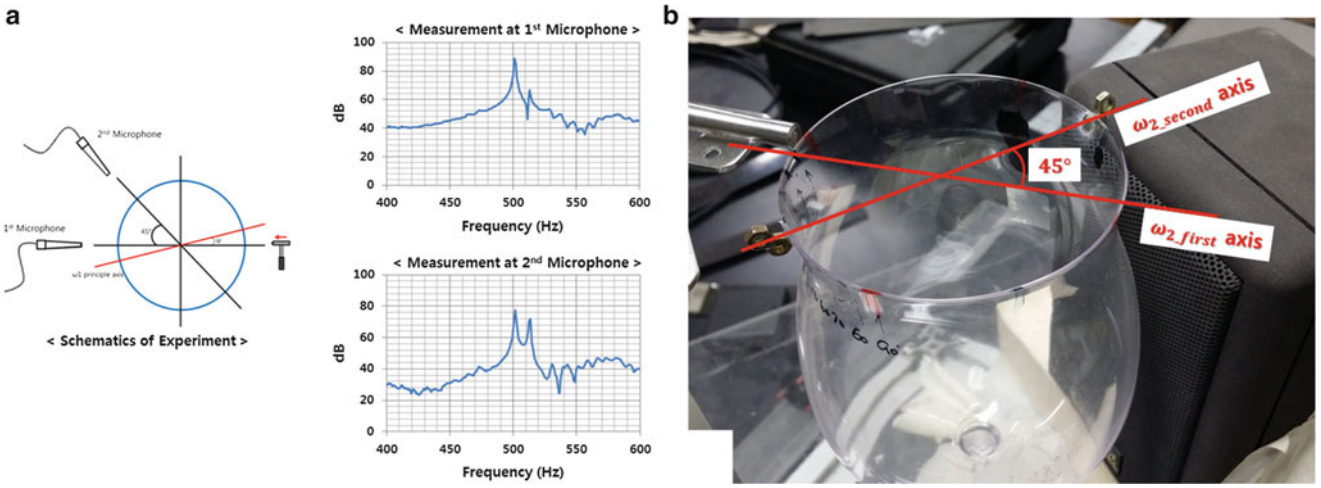

Fig. 4.2 (**a**) Dynamic characteristics of a wineglass, and (**b**) Experiment for frequency tuning

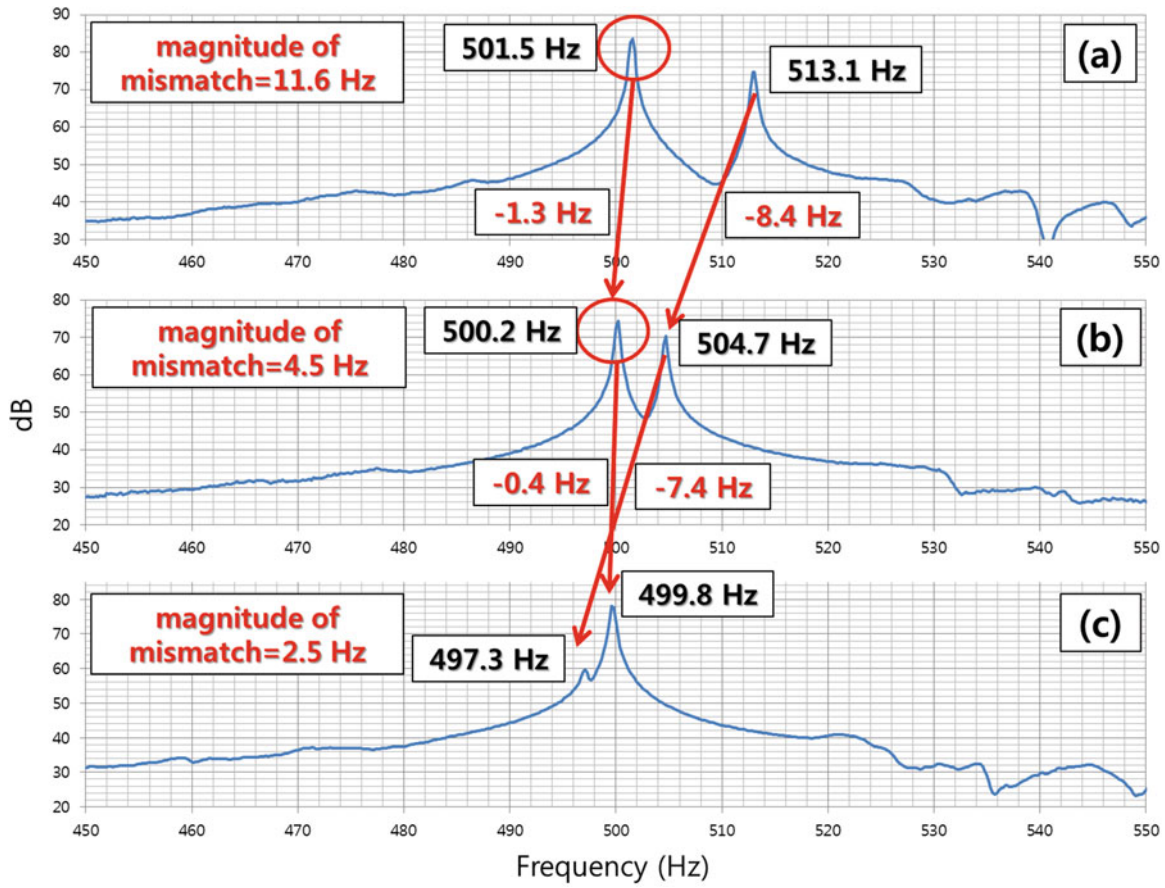

Fig. 4.3 Frequency spectra before and after frequency tuning: (**a**) before tuning, (**b**) after attaching two 0.32 g point masses, (**c**) after attaching four 0.32 g point masses

The mass of the resonator, 64 g, was a rough estimation using a solid CAD model. In addition, the glue used to attach the tuning mass may change the local damping, therefore, it may have influence on tuning. Considering these factors it is judged that the validity of the proposed tuning method has been verified. The proposed method can be generalized for a fine tuning of a gyroscopic resonator.

4.4 Conclusions

This paper develops a methodology for tuning of mismatched eigen frequencies of shell modes of an axisymmetric hemispherical-type resonators by attaching concentrated masses. In order to verify the proposed methodology, an ordinary wineglass was chosen as a resonator, and the frequency tuning was performed. The theoretical results show enough good consistency with the experiments. Thus, the proposed method can be applied to the frequency tuning of a hemispherical type resonator. The present method can be generalized for a mechanical tuning of various kinds of resonators. Finally, as a future research, the study on damping *(Q*-factor*)* tuning of a resonator is also necessary to get higher performance of the gyroscope, and, therefore, it is being performed too.

References

1. Sarapuloff SA, Kisilenko SP, Iosifov AO (1988) Rotation influence on dynamics of an imperfect hemispherical resonator. Collection of Sc. papers on Mechanics of Gyroscopic Systems (MGS), Issue 7, Vyshcha Shkola Publishers, Kyiv, pp 59–66. (In Russian)
2. Sarapuloff SA (1993) Stabilization of oscillations under principal parametric resonance in gyroscopic systems with conservative and dissipative couplings. Collection of Sc. papers on Mechanics of Gyroscopic Systems (MGS), Issue 12. Vyshcha Shkola Publishers, Kyiv, pp 65–74. (In Russian)
3. Lynch DD (1995) Vibratory gyro analysis by the method of averaging. In: Proceedings of the 2nd Saint-Petersburg international conference on gyroscopic technology & navigation, St.-Petersburg, RF, May 1995, pp 24–25
4. Pavlovskii MA, Sarapuloff SA, Kisilenko SP (1989) Dynamic symmetry condition of an imperfect hemispherical shell under free edge perturbation. Appl Mech Kyiv 25(9):102–108. (In Russian)
5. Sarapuloff SA, Kisilenko SP et al (1989) Frequency characteristics of imperfect shell resonator. J USSR's High Educ Establ Ser Instrum Mak XXXII(6):34–40. (In Russian)
6. Fox CHJ (1990) A simple theory for the analysis and correction of frequency splitting in slightly imperfect rings. J Sound Vib 142(2):227–243
7. Rhee HN, Park SJ, Park JS, Lee JC, Sarapuloff SA (2014) Determination of principal axes of a wineglass using acoustic testing. Special topics in structural dynamics. In: IMAC proceedings, conference proceedings of the society for experimental mechanics series, vol 6, pp 295–299

Chapter 5
An Innovative Tribometer for Measurements Between Sport Fabrics and Ice

E. Belloni, D. Milani, and F. Braghin

Abstract Nowadays sport competitions have to deal more and more with the technological developments of sport equipments. In the case of a skier, modern suits have innovative fabrics, usually designed to get high aerodynamic performances, but their frictional performances with snow and ice are not even assessed. The suit cannot help the athlete to stop in case of tumble, resulting in a potentially dangerous situation. Tests in wind tunnel give an estimation of the friction with air, but cannot measure the interaction with the snow. The device here presented provides an estimation of the fabric friction coefficient with snow (or ice), getting rid of the aerodynamic interactions. This tribometer has a light and simple structure, which can be easily dismounted and transported to make measurements directly on site, as well as potentially more flexible in the use with respect to already existing devices.

Keywords Tribometer • Ice friction • Fabrics • Portable structure • In-field tests

5.1 Introduction

Athletes to be more and more competitive must enhance all the aspects of their discipline. If in the past the physical training was the leading aspect, nowadays also technological components of the sport equipment play an important role for the final result. Differences between top athletes are almost minimal, final results are strongly affected by details. Just think to the last Winter Games in Sochi [1]: during the Women's Downhill competition the difference between the first and third place was in the order of 10/100 of a second, that is 3 m in a 2,700 m course. Further the first two athletes had exactly (accurate to a hundredth of a second) the same timing, resulting in the first ex equo gold medal of Winter Olympics. In most part of the disciplines, it is possible to see how big is the difference in performances between athletes with a modern and technological equipment, and the ones without these devices. There is an extended literature about new technologies in sports [2–5] and how it is still possible to improve performances [6, 7]. It is straightforward that this fact has created and still provokes lot of controversies: it enlarges the gap of rich and powerful Nations with respect to less economically strong ones. The ethical aspect about the use of these kind of technologies is not a trivial issue, to give rise to a possible new "*technological*" doping [8, 9].

5.1.1 Ski Fabrics

As pointed out by several researches [10, 11], the aerodynamic performance is improved by several factors: the equipment's aerodynamic properties, the athlete's body position during the activity, the design, styling and fit of the garments and the aerodynamic characteristics of its surface. Laing [12] estimated a drag reduction up to 10 % through the use of a suitable clothing. The problem of fabrics realization and their influence on parameter is not an easy task. In fact different topography and air permeability, in addition to material stretching, affect significantly the critical velocity, that is the moment in which the transition to turbulent regime is completed [13, 14]. A not complete characterization is available on the influence of garment textile parameters (like construction, porosity, tightness or openness, thickness, fibre composition and construction of the yarn) regarding aerodynamic performance [11]. Focusing now on ski fabrics, a leading role for a skier suit is the

E. Belloni • D. Milani • F. Braghin (✉)
Department of Mechanical and Engineering, Politecnico di Milano, Via La Masa 1, Milano (MI) 20156, Italy
e-mail: francesco.braghin@polimi.it

E.W. Sit (ed.), *Sensors and Instrumentation, Volume 5*, Conference Proceedings of the Society for Experimental Mechanics Series, DOI 10.1007/978-3-319-15212-7_5

aerodynamic drag force reduction[1] during a run. Broker [15] created a mathematical model to estimate the effects of F_D reduction on downhill race performance. With a mean velocity of 30 m/s (108 km/h) and a 15° slope of a straight 250 m track, if the F_D decreases of 1.48 N, the skier gains 0.069 s corresponding to 2.521 m. It may appear a small saving, but applied to a real, longer track it can create significant differences between athletes. If one considers that the change in F_D magnitude can be two to three times greater than 1.48 N thanks to the only fabrics, an apparel of this kind must be considered undoubtedly a significant factor in ski race performance [13].

This new kind of equipments allows professional (and amateur) skiers to reach higher velocities with respect to the past, increasing also the number of potentially dangerous accidents [16, 17]. Almost all the literature is based on the aerodynamic properties of fabrics, and not on the interaction between fabrics and ice or snow. That is to say that this garments are optimized for the air interaction, but as a consequence the friction coefficient between fabrics and snow/ice is also very low: if a skier makes an error and crashes on the ground, the suit cannot help him/her to stop, resulting in a virtually dangerous situation, in which a severe injury may happen. The skier safety must be guaranteed both by the track itself and by the equipment. Anghileri et al. [16] presented a detailed analysis on the safety nets installed at the side of a track. Hagel et al. [18] analysed the effect of the helmet on athletes' injury and crashes. A further step can be an optimization of the fabrics contact with ice to stop the skier in a shorter time, preserving its optimal aerodynamic characteristics. The tribometer here presented can measure the friction coefficient with the snow decoupling it by the aerodynamic properties of fabrics.

5.2 Mechanical Characterization

To perform measurements for the friction coefficient with air, a common way to proceed is to use a wind tunnel, simulating the air conditions (type of flow, velocity, boundary conditions, body shape,...) during a run [10, 11, 14]. Unfortunately, this approach is not sufficient to estimate also the second coefficient we are interested in. A dedicated device must be designed, reproducing the athlete fall conditions at high velocity. Some tribometers already exist (see Sect. 5.5), providing a motion to a mass with a piece of fabric attached on it. These tribometers must operate over a frozen floor: most part of these devices are big, complex and expensive, and must operate in dedicated and controlled environment conditions inside a laboratory. Our idea is inspired by this kind of devices, but we have tried to create a lighter structure, that can be disassembled and transported quite easily, and which is potentially more flexible in the use (a global 3D view of the device in Fig. 5.1). There is an external framework, with a mechanical transmission in the middle, which allows to apply a torque to the central beam. The two disks are linked at the beam extremities. The tangential velocity of the masses is similar to an average fall velocity, approaching realistic work conditions.

5.2.1 External Framework

The structure has two bases, with a big surface of contact on the snow/ice, achieving a better weight distribution and ensuring stability. To improve the stability, three holes are made on these bases, where it is possible to place ice nails. Four vertical

Fig. 5.1 Global view of the tribometer

[1]The drag force expression is generally formulated as: $F_D = \frac{1}{2}\rho V^2 C_D A_p$ where ρ is the air density, V is the velocity of the athlete, C_D is the non-dimensional drag coefficient and A_p is the frontal area.

Fig. 5.2 Particular of the external framework of the device

IPE beams (two per side) are rigidly connected to the bases by a soldering process. Other four horizontal IPE beams create the central part of the structure: this time the connection between horizontal and vertical parts of the frame is provided by a series of bolts, therefore it can be dismounted easily. One may note that this orientation of the beams is useful to minimize the elastic deflection of beams under load. In the center, there are two plates (connected to the structure again with some bolts) that are used to place the motor and the other parts of power transmission (see Fig. 5.2).

5.2.2 Transmission

The power transmission chain is placed in the center of the structure and operates in vertical direction. The transmission is composed of (please refer to Fig. 5.3):

- **A**: a brushless three-phase servo motor, powered by an inverter. It can provide a nominal torque of 2.10 Nm with a nominal speed of rotation of 3,000 round/min.
- **B**: a Wittenstein© gearbox with a transmission ratio $i = 40$. In Fig. 5.3 only the bottom part of the transmission is visible, the most part is protected by the horizontal IPE beams.
- **C**: a Wittenstein© gearbox joint, torsionally rigid in order to transmit almost perfectly the torque. It must guarantee an high torsional stiffness to not threaten the final measurements, while a little backlash in other directions is bearable to compensate geometrical and dynamical imperfections.
- **D**: a torque sensor, useful to measure the resistant torque of the downstream part of the chain: it is an indirect way of measure of the friction coefficient.
- **E**: the final hub which connects the shaft of the torque sensor to the rotating structure.
- **F**: an accessory part of the frame, which simply transfers the axial load of the transmission to the external frame by means of two lateral vertical beams. In the center of the plate, a bearing helps to maintain concentric the transmission and is subjected to an axial load.

5.2.3 Disks and Weights

The final hub (part E in Fig. 5.3) performs the transmission of torque to a square tube steel beam. As previously written, at the extremities of the beam, two disks covered with the fabrics are connected. Inside the beam, small aluminium blocks are inserted to contrast the crushing of the metal sheet during bolt fastenings. The whole structure is sized for a beam maximum rotation frequency of 4 Hz. The disk is connected to the beam thanks to a purely linear steel guide, with a lobed profile and a low friction coefficient in order to decrease as much as possible the influence of guide's motion on final measurements. We have chosen a linear guide to compensate the vertical motion of the disks due to a possible not perfect levelling of the surface; moreover it avoids the rotation of the disk itself, which could falsify the measure. One side of the linear guide has a threaded hole and it is connected to the base of the disk with a screw. The piece of fabrics must upholster the base of the disk and is fixed thanks to the two half circled steel part just over the base (they are connected with screws too). In Fig. 5.4 the ocher parts inside the disk are the weights, that together with the rest of the disk reach approximately 23–25 kg: this total weight, over the surface of the base, and with the 4 Hz frequency of rotation, reproduces the fall conditions of an athlete.

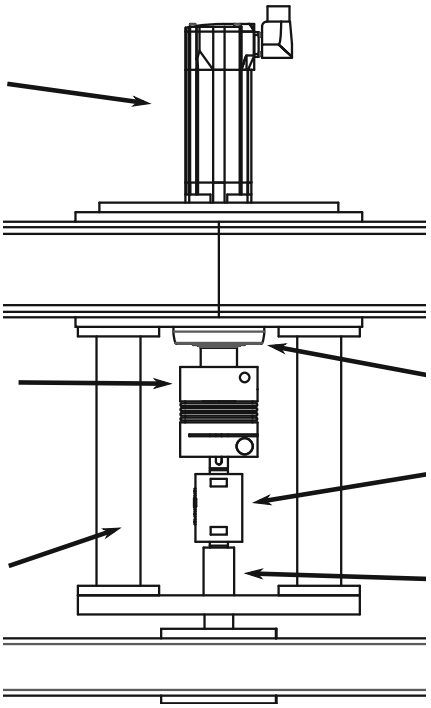

Fig. 5.3 Focus on the power transmission part

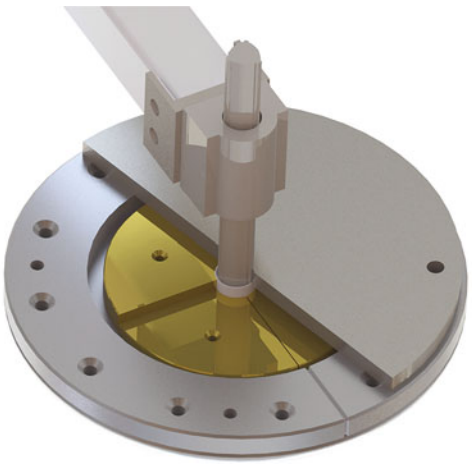

Fig. 5.4 A view of the disk with some weights inside

Two steel half disks cover the disk, this is done to reach the desired weight, to act as an anti-unscrewing device and to enhance the safety of the disk, decreasing the possibility of weights motion and detachment. It is expected to do some tests with the masses raised from the ground for a fine-tuning and equilibration of the structure.

5.3 Dynamics and Measurements

In Fig. 5.5 a schematic representation of the system is provided. It is possible to take advantage of the structure symmetry: only half of the real system is considered to simplify the problem.

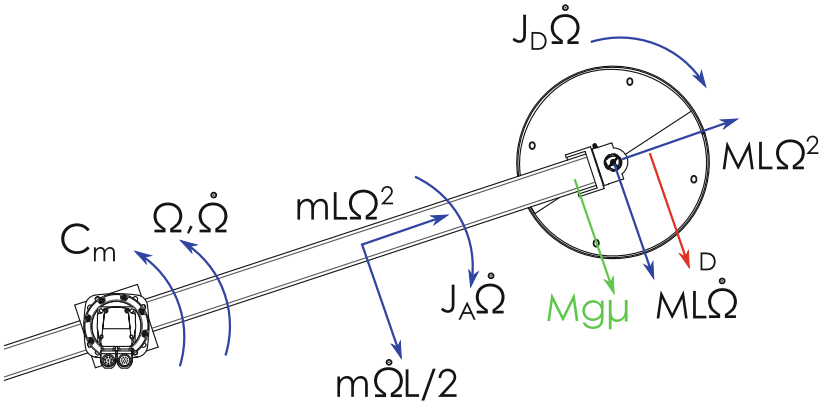

Fig. 5.5 A simplified scheme of the device. Dynamical forces acting on the structures are represented

The equation of dynamic equilibrium is:

$$\frac{C_m}{2} = \frac{1}{3}mL^2\dot{\Omega} + \frac{1}{2}MR^2\dot{\Omega} + \ldots + ML^2\dot{\Omega} + MgL\mu + DL + \frac{mL^2}{4}\dot{\Omega} \tag{5.1}$$

where:

C_m torque generated by the motor;
m beam mass, considered lumped and placed on the center of mass of the beam;
L beam length;
Ω beam rotational velocity;
M disk mass;
R disk radius;
g gravity;
μ friction coefficient;
D drag force acting on the disk.

If one considers $J_A = \frac{1}{3}mL^2$ and $J_D = \frac{1}{2}MR^2$, substituting them in Eq. (5.1):

$$\frac{C_m}{2} = J_A\dot{\Omega} + J_D\dot{\Omega} + (M + \frac{m}{4})L^2\dot{\Omega} + MgL\mu + DL = = \bar{J}\dot{\Omega} + D(\Omega^2)L + MgL\mu \tag{5.2}$$

Equation (5.2) is a compact formulation of the moment equilibrium, where $\bar{J}$ is the equivalent inertia. It is easy to notice the direct dependency of the drag force with the (squared) velocity of the skier. Friction coefficient is as well not constant but velocity dependent. Considering now Eq. (5.2) at its operating speed (so $\dot{\Omega} = 0$), one gets:

$$\frac{C_{m,r}}{2} = D(\Omega^2)L + MgL\mu \tag{5.3}$$

Then, the condition with the mass lifted from the ground is:

$$\frac{C_m}{2} = \bar{J}\dot{\Omega} + D(\Omega^2)L \tag{5.4}$$

and at the operating speed:

$$\frac{C_m, r}{2} = D(\Omega^2)L \tag{5.5}$$

5.4 Measurements

The measuring devices integrated in the system are:

- a *torsiometer*, placed along the power transmission chain (see Fig. 5.3), to measure the transmitted motor torque and the resisting torque due to internal frictions and sliding of the fabrics on the ground;
- *Two wireless accelerometers*, placed on the disk to measure the tangential ($L\dot{\Omega}$) and centrifugal ($L\Omega^2$) accelerations. Alternatively it is possible to integrate in the system a single *encoder*, gaining a further simplification of the system.

Two tests must be performed to get an estimation of the friction coefficient (please refer to Appendix A.1 for further details on ice and snow friction coefficient).

Test I: constant Ω A set of tests are performed with the masses lifted from the ground and in operating speed conditions, keeping constant the Ω and varying it among the tests. Considering Eq. (5.5), it is possible to get the drag force $D(\Omega)$ as function of velocity. Once this parameter is estimated, the same tests must be performed, this time keeping the masses on the ground [see Eq. (5.3)]. The only unknown is the friction coefficient, which is estimated as a function of velocity ($\mu(\Omega)$). The final result of this procedure is a 2D plot of the friction coefficient dependent on the velocity.

Test II: acceleration and deceleration The goal now is to estimate the influence of acceleration and deceleration phases on the friction coefficient, that is $\mu(\Omega, \dot{\Omega})$. Starting with the lifted masses, it is now possible to estimate the equivalent inertia $\bar{J}$ of the system from Eq. (5.4) (the $D(\Omega)$ parameter was estimated above). Finally, thanks to the complete dynamic equation (Eq. (5.2)), an estimation of $\mu(\Omega, \dot{\Omega})$ parameter is possible. This time the diagram of friction coefficient is function of both velocity and acceleration.

5.5 Other Tribometers

With respect to other similar devices, it has many advantages that it is possible to sum up in this section. First of all the whole device is easy to mount and dismount, resulting consequently in a straightforward flexibility in the use. Further, as already underlined, it is dedicated to an outdoor use in variable environmental conditions, characteristic that allows to take data from real conditions, untied from a laboratory with controlled atmosphere. This is an evident advantage, but also a restriction: tests can be performed only if the weather conditions are appropriate (temperatures below 0°C, a suitable icy or snow-clad surface,...) and there is a lower control on parameters, which could vary among the experiments and potentially also during a test itself. Zheng et al. [19] patented a tribometer with a structure easy to disassemble, but it was dedicated for tests on icy roads. Scherge et al. [20] proposed a tribometer for an indoor, environment controlled test of tires on ice. Most part of patents, like the ones of Kenhachi [21], Kentaro [22] and Naoyuki [23], considers only big and non-disassembling structures. In the tribometer we are illustrating, due to these characteristics also the costs for material and manufacturing are small. Further, access to all the parts of the device is allowed: thus it is possible to do a fine-tuning of the system, maintenance and structural modifications. Tuning and balancing of the tribometer is self-guaranteed by the two masses, rotating at the two opposite sides of the beam. Theoretically (structurally it requires several mechanical modifications), one can balance the structure also decreasing the distance of one mass with respect to the center of rotation and increasing its weight (or decreasing the other mass): this allows to perform the tests along two different trails, decreasing the "*digging*" effect of the masses during the tests (which is a problem for some tribometers). Differences with other devices can be found also on other characteristics: the kind of motion of the machine (for example Zheng et al. [19] proposed a device with a linear alternate motion), the possibility to variate the weight on the test material (see Mani et al. [24]) and to apply a variable pre-compression to the material (see Lackman [25]). In our tribometer the contact with the ground is guaranteed by the weight itself of the masses, and the linear guides are useful to compensate eventual misalignments of the ground surface.

5.6 Conclusions and Future Applications

The tribometer here described is an innovative and promising device for the friction coefficient estimation between fabrics and ice or snow. It is affordable, easy to transport and with an intuitive use. Its characteristics allow to estimate the friction coefficient of fabrics with ice and snow, separating this measurements from the aerodynamic influence. It is dedicated for

outdoor in-side tests of fabrics. Its potentialities can overcome this specific application: due to its flexibility, it would be possible to change the extremities (the disks), substituting them with ice skates or tires, in order to estimate the friction coefficient in a totally different situation with respect to the original scope.

Important Notes

The patent for the device here presented is currently in press.

A.1 Appendix: Notes on Ice Friction

In Sect. 5.4 we have illustrated an easy procedure to estimate experimentally the value of friction coefficient μ for different values of velocity and acceleration of the moving part. From elementary concepts of mechanics, the coefficient of friction is the ratio between the tangential friction force to the normal reaction, considering two bodies with a relative sliding motion. This ratio is not a constant values and it depends, besides the $\Omega(t)$ and the properties of the materials, also on pressure and temperature. An important property is the low value of kinetic friction for speed higher than $\sim 0.1\text{ms}^{-1}$ [26]. It is a useful property for some application like winter sport (speed-skating for example), but sometimes exactly the opposite is needed, like in the design of automobile tyres [27] and also the case of fabrics here presented. Evans et al. [28] found a linear dependence of μ on $v^{-1/2}$, testing steel, copper and perspex on ice (see also Oksanen [29], Akkok et al. [30]). Falling the temperature, μ rises for a given speed: the quantity of work needed to raise the interface to melting point is greater. The value of μ decreases with increasing load L, roughly as $L^{-1/3}$ [26]: dissipation depends both from the lubricant viscosity and the shearing of adhesion points and their ploughing [31, 32]. In these experiments a thin layer of water at the sliding interface is considered: Bowden and Hughes [33] conjectured that the local heating was a consequence of the work dissipated by friction. A small part of the heat melts the ice, and the water refreezes behind the slider [26].

In literature one can find detailed models for the sliding of a material on ice: Skouvaklis et al. [34, 35] proposed a model for the sliding of rubber on ice:

$$\mu = \frac{\Delta T}{2v\sigma_n}\sqrt{\lambda C_p \rho}\sqrt{\frac{\pi}{t_c}} \tag{5.6}$$

where ΔT is the temperature difference between the initial temperature and the melting temperature, v is the velocity, σ_n is the normal stress, λ the thermal conductivity, C_p the specific heat capacity, ρ the density and t_c the contact time of the sliding object. It is a heat flow based model, where the friction coefficient is directly connected to the thermal energy transferred to the ice during the sliding motion. Due to the higher thermal conductivity of ice, it is assumed that all the heat is transferred to the ice, while the resulting temperature rising is such that a melt-water layer forms. Another example is provided by Bäurle et al. [36], who proposed a model for the friction of polyethylene on ice. With data from experiments, it would be possible to propose and validate a similar model also for the fabrics tested with the tribometer here discussed.

References

1. http://www.sochi2014.com/en/alpine-skiing-ladies-downhill, 2014
2. Fuss FK, Subic A, Ujihashi S (2007) The impact of technology on sport II. CRC Press, London
3. Haake SJ (2009) The impact of technology on sporting performance in Olympic sports. J Sports Sci 27(13):1421–1431
4. Balmer N, Pleasence P, Nevill A (2012) Evolution and revolution: gauging the impact of technological and technical innovation on Olympic performance. J Sports Sci 30(11):1075–1083
5. Foster L, James D, Haake S (2012) Influence of full body swimsuits on competitive performance. Procedia Eng 34:712–717
6. Berthelot G, Thibault V, Tafflet M, Escolano S, El Helou N, Jouven X, Toussaint JF (2008) The citius end: world records progression announces the completion of a brief ultra-physiological quest. PLoS One 3(2). Doi: 10.1371/journal.pone.0001552
7. Radicchi F (2012) Universality, limits and predictability of gold-medal performances at the Olympic Games. PloS one 7(7). Doi: 10.1371/journal.pone.0040335
8. Miah A (2006) Rethinking enhancement in sport. Ann N Y Acad Sci 1093(1):301–320
9. James D (2010) The ethics of using engineering to enhance athletic performance. Procedia Eng 2(2):3405–3410

10. Barelle C, Ruby A, Tavernier M (2004) Experimental model of the aerodynamic drag coefficient in alpine skiing. J Appl Biomech 20:35–67
11. Oggiano L, Troynikov O, Konopov I, Subic A, Alam F (2009) Aerodynamic behaviour of single sport jersey fabrics with different roughness and cover factors. Sports Eng 12:1–12
12. Laing R (2002) Clothing, textiles and human performance: a critical review of the effect on human performance of clothing and textiles. The Textile Institute, Manchester
13. Brownlie L, Larose G, D'Auteuil A, Allinger T, Meinert F, Kristofic P, Dugas S, Boyd R, Stephens D (2010) Factors affecting the aerodynamic drag of alpine skiers. In: 8th Conference of the international sports engineering association (ISEA) 2010
14. Oggiano L, Roar S, Morten B, Brian H (2012) Air permeability and drag crisis on high tech fabrics for cross-country ski competitions. Procedia Eng 34:15–19
15. Broker J Model of Skiing Aerodynamics for the United States Olympic Committee 1991. Unpublished Report
16. Anghileri M, Eralti D, Milanese A, Prato A, Castelletti L, Giorla M (2014) Nonlinear finite element analysis applied to the development of alpine ski safety net. Int J Crashworthiness 19(2):161–171
17. Giorla M, Berutti G (2002) Progresso tecnologico e sicurezza sulle piste da sci. In: Meeting on technological progress and safety on ski tracks, Luino, Italy
18. Hagel B, Pless IB, Goulet C, Platt R, Robitaille Y (2005) The effect of helmet use on injury severity and crash circumstances in skiers and snowboarders. Accid Anal Prev 37:103–108
19. Zheng M, Peng L, Meng J, Sun Y, Li C (2011) CN202362235U - Simple friction coefficient test device, 2011
20. Scherge M, Böttcher R, Richter M, Gurgel U (2012) High-speed ice friction experiments under lab conditions: on the influence of speed and normal force, Hindawi Publishing Corporation, ISRN Tribol 2013:6
21. Kenhachi MM, Chikahiro S (2000) JP08166339 - Friction Tester, 2000
22. Kentaro K (2011) JP2010249693 - On-ice friction tester and on-ice friction test method, 2011
23. Naoyuki K (2011) JP2011149870 - Friction test device and friction test method, 2011
24. Mani N, Olesky S, Christy D (1999) US6199424 B1 - Portable universal friction testing machine and method, 1999
25. Lackman T (2008) US20080163667 A1 - Device for the evaluation of ski wax, 2008
26. Petrenko VF, Whitworth RW (1999) Physics of ice, p 373. Oxford University Press, Oxford
27. Ahagon A, Koyayashi T, Misawa M (1988) Friction on ice. Rubber Division, American Chemical Society 1988
28. Evans D, Nye J, Cheeseman K (1976) The kinetic friction of ice. Proc Roy Soc Lond A 347. doi: 10.1098/rspa.1976.0013
29. Oksanen P, Keinonen J (1982) The mechanism of friction of ice. Wear 78:315–24
30. Akkok M, Ettles C (1987) Parameters affecting the kinetic friction of ice. J Tribol, Trans ASME 109:552–561
31. Tabor D (1987) Friction and wear - ddevelopments over the last fifty years. In: Institution of mechanical engineers international conference 1987-5 on tribology - friction, lubrication and wear. Fifty years on, 1987
32. Hutchings I (1992) Tribology: friction and wear of engineering materials, chap. 3. Edward Arnol, London
33. Bowden FP, Hughes TP (1939) The mechanism of sliding on ice and snow. Proc R Soc Lond A 172(949):280–298
34. Skouvaklis G, Blackford JR, Koutsos V (2012) Friction of rubber on ice: a new machine, influence of rubber properties and sliding parameters. Tribol Int 49:44–52
35. Higgins DD, Marmo BA, Jeffree CE, Koutsos V, Blackford JR (2008) Morphology of ice wear from rubber-ice friction tests and its dependence on temperature and sliding velocity. Wear 265(5–6):634–644
36. Bäurle L, Szabó D, Fauve M, Rhyner H, Spencer N (2006) Sliding friction of polyethylene on ice: tribometer measurements Tribol Lett 24(1):77–84

Chapter 6
Passive Stress Sensing Using Raman Piezo-Spectroscopy

N.-G. Kim, T. McCulloch, J.-J. Lee, and H.-B. Yun

Abstract The objective of this study is to develop a method to measure stress in a structural member using the Raman Piezo-spectroscopy (RPS) as passive sensors. RPS is a matured non-destructive spectroscopy technology widely used in material science and aerospace engineering to measure stress in various substances. The method uses RPS to provide an innovative solution for stress measurement without supplying external power and installing delicate electronic circuits in field conditions. The RPS system consists of the RPS reader and target. The target can be commercially manufactured with Raman-sensitive metal oxides (e.g., α-Al_2O_3). In the target manufacture, sputtered metal oxides at a high temperature are solidified with a hot isostatic press. Therefore, the target can be used as a passive sensor that does not require external power supply and additional electronic circuits. The RPS reader is a noncontact Raman spectrometer that shoots a low-powered laser beam on the target surface and analyzes the fluorescence beam. This paper will discuss the novel concept of the Raman-based stress sensing and some preliminary testing results.

Keywords Raman spectroscopy • Stress measurement • Piezo-spectroscopy • Passive sensor • NDT

6.1 Introduction

Stress caused by self-weight, thermal stress, and residual stress formed by manufacturing process as well as applied stress have an effect on structural performance and stability of civil infrastructure. Therefore, it is important to develop effective stress measurement techniques in the civil engineering and structural maintenance field. Recently, stress measurement techniques using strain gauge and RPS, X-ray, ultrasonic wave, magnetic field are used for non-destructive stress measurement in the material science field [1]. Since the former technique-using strain gauge-is a highly precise technique, the technique is widely used in the maintenance field, but it measures only relative stress values. The latters of stress measurement technique-using RPS, X-ray, ultrasonic wave, magnetic field-can measure absolute stress values. However, they are not suitable for field experiments because the equipment is complex and sensitive to the uncontrolled field environment. In contrast, with the recent advent of portable-size Raman spectrometers, RPS technique can be applied for field experiments. Forman et al. [2] developed the pressure measurement techniques using luminescence of ruby. Grabner [3] and Lipkin and Clarke [4] used RPS to determine the residual stress of alumina. RPS has been extensively researched in the material science field [5–8]. In contrast, the technique is not applied for stress measurement of civil infrastructure. This work, therefore, introduces the RPS technique to the civil engineering field.

This paper derives a method measuring the thermal residual stress of layered α-Al_2O_3 thin film on SiO_2 on silicon wafer and low carbon steel substrates using RPS technique. The feasibility of the method is verified experimentally through four thin-film samples stressed in tension and compression.

N.-G. Kim • J.-J. Lee
Sejong University, 209 Neungdong-ro, Gwangjin-gu, Seoul, Republic of Korea

T. McCulloch • H.-B. Yun (✉)
University of Central Florida, 12800 Pegasus Drive, Suite 211, Orlando, FL, USA
e-mail: Hae-Bum.Yun@ucf.edu

E.W. Sit (ed.), *Sensors and Instrumentation, Volume 5*, Conference Proceedings of the Society for Experimental Mechanics Series, DOI 10.1007/978-3-319-15212-7_6

6.2 Theoretical Background

6.2.1 Raman Spectroscopy

Spectroscopy is the measurement and interpretation of absorption and emission of electromagnetic radiation when atoms or molecules or ions move from one energy level to another. The spectroscopic method of the different regions of the electromagnetic spectrum are the most powerful and useful techniques available for the understanding of molecular structure, nature of bonding between atoms, conformation analysis, symmetry of molecular groups or ions in crystals, and so forth. In short, spectroscopy has become an indispensable tool to present day physicists and chemists owing to the availability of very sophisticated instruments with data processing arrangements [9].

Among the spectroscopic techniques, Raman spectroscopy provides information about molecular vibrations, without destroying the target sample that can be used for sample identification and quantitation. In Raman scattering measurements a monochromatic light source, usually a single mode laser, is incident on the sample and scattered light is detected. The majority of the scattered light is of the same frequency as the excitation source; this is known as Rayleigh or elastic scattering. Very small amount of the scattered light with lower (Stokes lines) or higher (Anti-Stokes lines) wavelength is shifted in frequencies from the laser frequency due to interactions between the incident electromagnetic waves, and the vibrational energy levels of the molecules in the sample. The energy difference between the incident and scattered light, so called Raman shift and usually expressed in terms of wave number cm^{-1}. This shift is independent of the frequency of the incident light [10].

The typical concept of a Raman spectroscopy system is composed of excitation laser source and Raman spectrometer, which is including collimating mirror, grating, focusing mirror and CCD detector. The schematic of the experimental setup is described in Fig. 6.1.

In the past, the Raman spectroscopy was considered a laboratory technique that involves a large-scale spectrometer. In recent years, with the advent of a laser diode technology combined with a multichannel charged-couple device (CCD), portable-size Raman spectrometers have become commercially available. Therefore it can be applied for field experiments without external power and installing delicate electronic circuits.

6.2.2 Spectroscopic Stress Measurement: Piezo-Spectroscopy

Raman spectroscopy can provide information of stress to which material is subjected through the shift of selected spectroscopic bands. This is knows as the piezo-spectroscopic (PS) effect.

Figure 6.2a shows the emission peaks of α-Al_2O_3 at zero-stress state. When the α-Al_2O_3 is subjected to compressive stress, the R_1 and R_2 peaks are shifted to the left, while when the α-Al_2O_3 is subjected to tensile stress, those peaks are shifted to the right. In other words, the position of peak is related with stress through the piezo-spectroscopic coefficient that allow the wavenumber peak shift to be converted into a stress measurement using linear tensorial equation as,

$$\Delta v = \prod_{ij} \sigma_{ij} \tag{6.1}$$

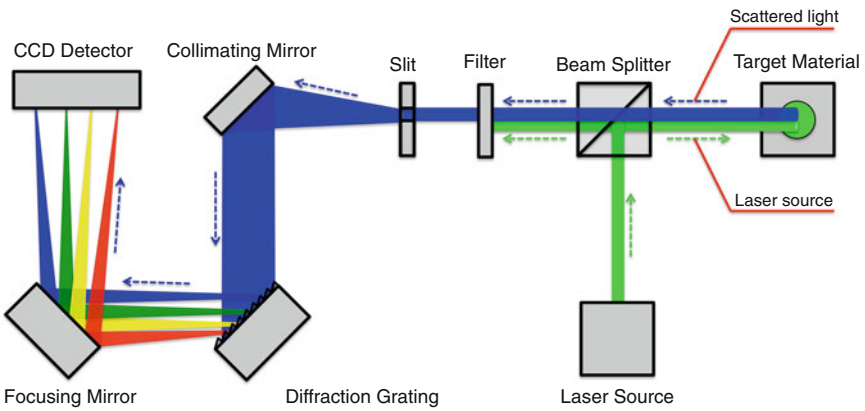

Fig. 6.1 Schematic of general Raman spectroscopy system

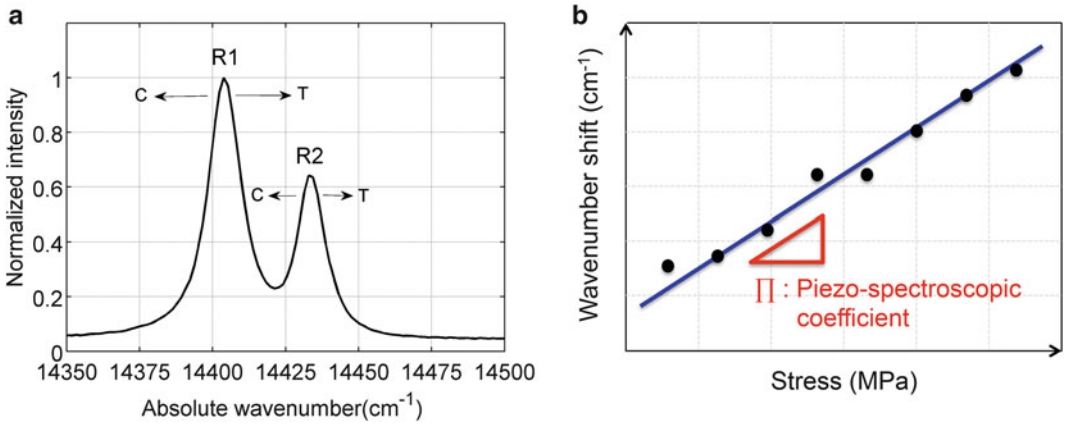

Fig. 6.2 Stress determination using spectroscopy technique (*C*: compressive stress, *T*: tensile stress)

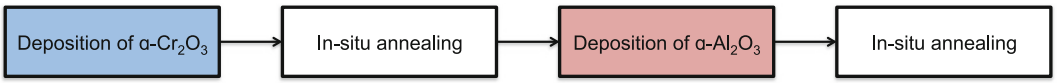

Fig. 6.3 α-Al_2O_3 deposition process

Where Δv is the peak wavenumber shift, σ_{ij} is the stress tensor and $\prod_{ij}$ is the symmetrical matrix of piezo-spectroscopic coefficients as

$$\Pi_{ij} = \begin{bmatrix} \Pi_{xx} & 0 & 0 \\ 0 & \Pi_{yy} & 0 \\ 0 & 0 & \Pi_{zz} \end{bmatrix} \tag{6.2}$$

Hence, the relation of the stress and peak wavenumber shift can be determined with the piezo-spectroscopic coefficients [4].

6.3 Experimental Setup

6.3.1 Sample Preparation

A thin film of α-Al_2O_3 was deposited on a low carbon steel and SiO_2 on silicon substrates. The α-Al_2O_3 deposition was performed at temperatures of 700 and 750 °C through physical vapor deposition (PVD). Thermal residual stresses are introduced between the Al_2O_3 film and substrates upon cooling because there is a difference in their coefficients of thermal expansion: tensile stress for the SiO_2 on silicon substrate sample and compressive stress for the steel substrate sample. These samples contain only thermal loads, which are introduced into the constitutive equations according to the following equation as

$$\sigma = \alpha E \Delta t \tag{6.3}$$

Where σ is the thermal stress, E is the elastic modulus, α is the thermal expansion coefficient, and Δt is the temperature change. The thermal expansion coefficients are 7.6×10^{-6}/°C for α-Al_2O_3, 12.3×10^{-6}/°C for low carbon steel, and 0.5×10^{-6}/°C for SiO_2. Additionally, the α-Cr_2O_3 template is used for aiding the development of α-Al_2O_3 at low transformation temperature. The deposition process involved following steps (Fig. 6.3):

The PVD process was carried out at various substrate temperatures as shown in Table 6.1. Figure 6.4 shows the resulting α-Al_2O_3 thin film on each substrate.

Table 6.1 Sample cases based on type of substrates and deposition temperatures

#	Type of substrate	α-Cr_2O_3 deposition temperature (°C)	α-Al_2O_3 deposition temperature (°C)
1	Polished low carbon steel	700	700
2	SiO_2 on silicon wafer	700	700
3	Polished low carbon steel	750	750
4	SiO_2 on silicon wafer	750	750

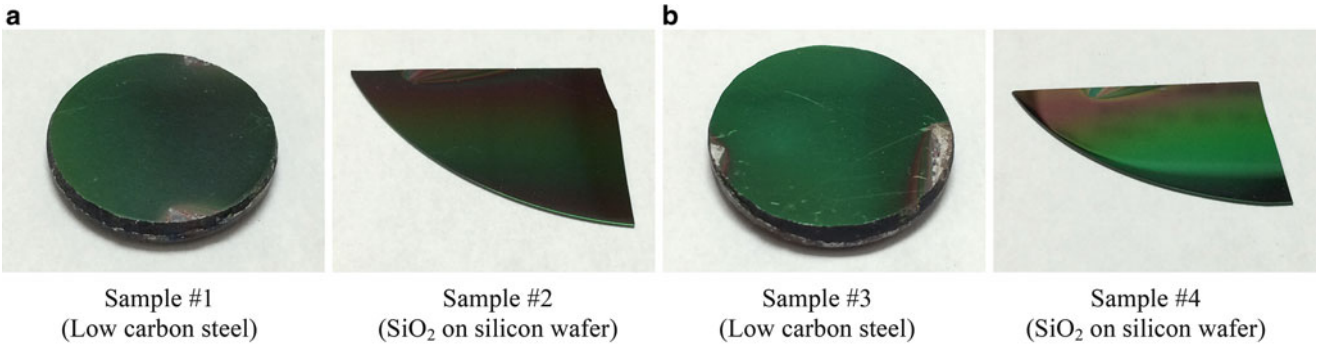

Fig. 6.4 Pictures of α-Al_2O_3 thin film samples

6.4 Experimental Results

6.4.1 Wavenumber Peak Shift

A benchtop Raman spectrometer (Renishaw RM1000b, 1,800 line/mm grating, imaging CCD detector) was used to obtain fluorescence spectra. The excitation source was a 514.5 nm argon ion laser (50 mW output power), and the 50× of objective was utilized to observe the samples through a microscope. The testing parameters included 30 s of integration time and five scans were averaged for each spectrum.

Figure 6.5 shows the resulting wavenumber peak shift. The x- and y-axes represent the absolute wavenumber, and normalized intensity, respectively. In fact, when α-Al_2O_3 is subjected to stress, the intensity and FWHM are changed in addition to the expected peak shift. In this work, peak shift of the wavenumber is considered, for stress estimation without considering intensity values and FWHM. For this reason, y-axis was normalized on the basis of maximum value of intensity.

In Fig. 6.5, the solid lines indicate α-Al_2O_3 spectra at the zero-stress state, and the dotted lines indicate α-Al_2O_3 spectra at non-zero-stress state.

Since the deposition temperatures of the sample #3, #4 are higher than sample #1, #2, the wavenumber peak shifts of sample #3, #4 are greater than the wavenumber peak shifts of sample #1, #2 based on Eq. 6.3. Furthermore, in the case of low carbon steel, wavenumber peak shift indicates compressive stress, but in the case of SiO_2 on silicon wafer, wavenumber peak shift indicates tensile stress.

6.4.2 Estimation of Thermal Residual Stress Based on Spectra

Lipkin and Clarke [4] assumed that the thermal residual stresses are biaxial in oxide scale, such that $\sigma_{xx} = \sigma_{yy} = \sigma_R$ and $\sigma_{zz} = 0$. In this limit, Eq. 6.1 reduces to

$$\overline{\Delta\upsilon} = \frac{2}{3}\prod_{ij}\sigma_R \tag{6.4}$$

In this study, thermal residual stresses are estimated for α-Al_2O_3 thin film samples based on Eq. 6.4, with piezo-spectroscopic coefficients in Table 6.2 and wavenumber peak shift in Table 6.3. The estimated thermal residual stresses are shown on Table 6.3. The stresses are estimated from each of R-lines and then calculated to average stresses using those of results.

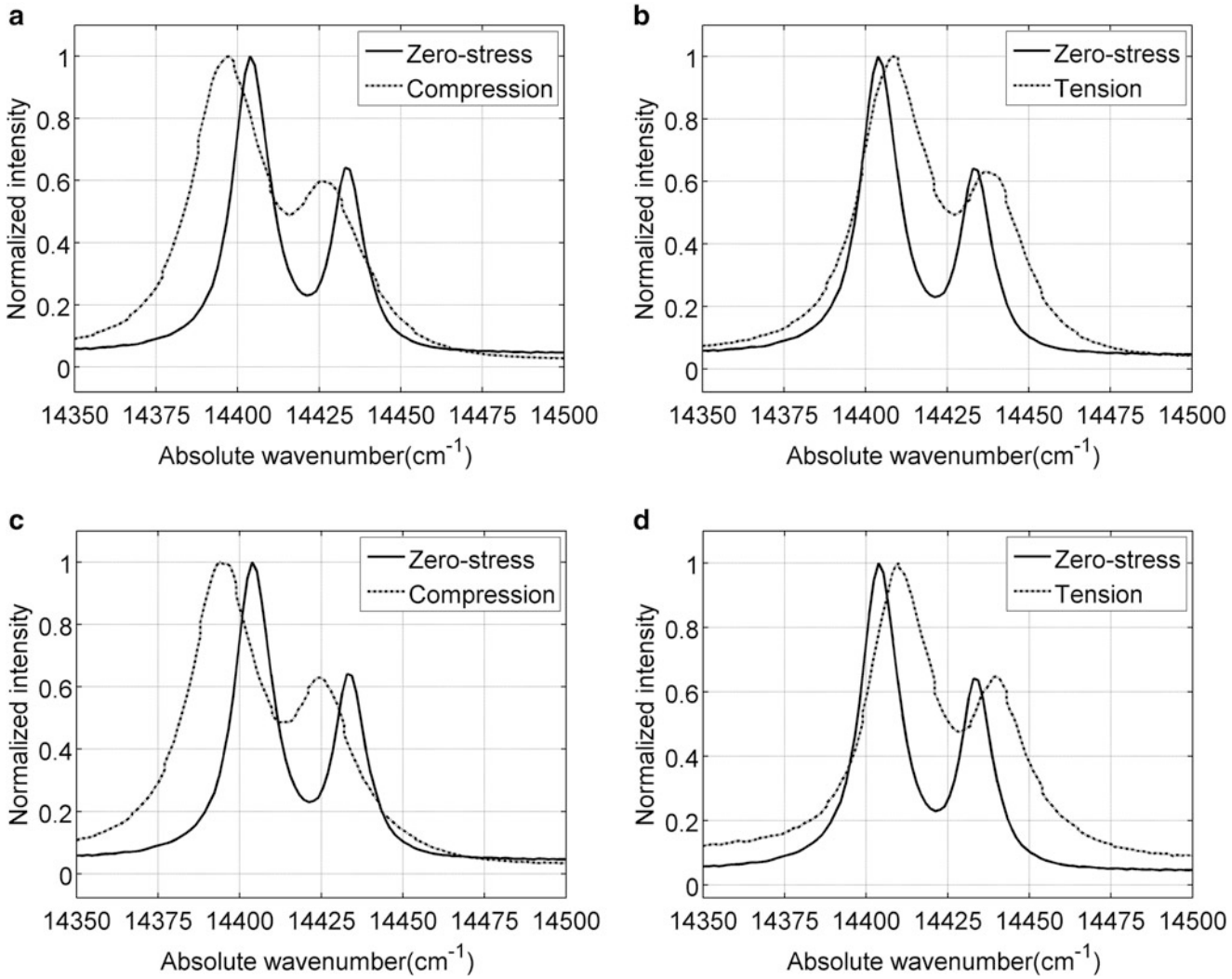

Fig. 6.5 Wavenumber peak shift of α-Al_2O_3 thin film samples

Table 6.2 Piezo-spectroscopic coefficients for α-Al_2O_3

Line	$\prod_{11}$	$\prod_{22}$	$\prod_{33}$	$\prod_{11}+\prod_{22}+\prod_{33}$
$\mathbf{R_1}$	2.56	3.50	1.53	7.59
$\mathbf{R_2}$	2.65	2.80	2.16	7.61

Table 6.3 Estimation of thermal residual stress of α-Al_2O_3 thin film samples

Sample number	R_1 wavenumber peak shift (cm^{-1})	Estimated stress (GPa)	R_2 wavenumber peak shift (cm^{-1})	Estimated stress (GPa)	Estimated average stress (GPa)
#1 (Low carbon steel)	−5	−0.99	−6	−1.18	−1.09 (compression)
#2 (Silicon wafer)	6	1.19	5	0.99	1.09 (tension)
#3 (Low carbon steel)	−8	−1.58	−8	−1.58	−1.58 (compression)
#4 (Silicon wafer)	8	1.58	8	1.58	1.58 (tension)

The compressive stresses were estimated at 1.09 GPa for sample #1 and 1.58 GPa for sample #2. Furthermore, the tensile stresses were estimated at 1.09 GPa for sample #2 and 1.58 GPa for sample #4. These results are represented using linear graph in Fig. 6.6, where the center point designates zero-stress state, and others indicate non-stress state for each case.

Simple 2D axisymmetric finite element models are constructed to validate the trend of thermal residual stress in α-Al_2O_3 results for the thin film samples. The simulation and comparison results are shown in Table 6.4. The error is significant due to the simulation models consider only thermo-elastic stress and assume perfect bonding between each of the layers. However,

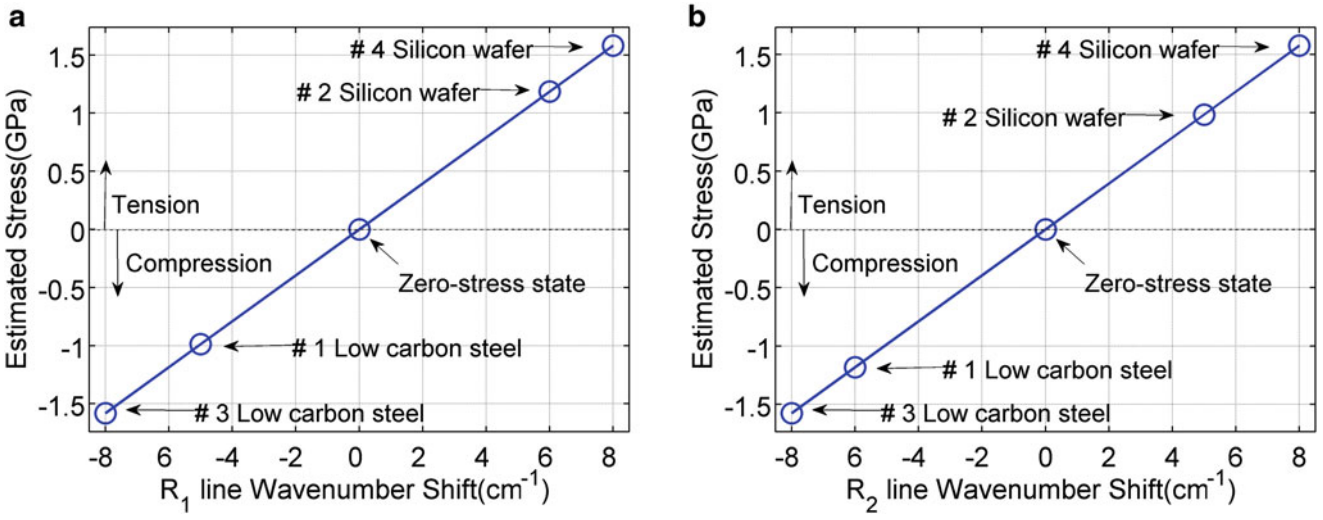

Fig. 6.6 Piezo-spectroscopic relation of R_1 and R_2 lines of α-Al_2O_3 thin film

Table 6.4 Comparison between estimated stress using RPS and simulated results

Sample number	Estimated stress using RPS (GPa)	Simulated results (GPa)	Error (%)
#1 (Low carbon steel)	−1.09	−1.55	42
#2 (Silicon wafer)	1.09	1.64	50
#3 (Low carbon steel)	−1.58	−1.66	5
#4 (Silicon wafer)	1.58	1.76	11

the trends are not significantly different. Therefore, we can expect that the experiments using RPS are well performed for measurement of the thermal residual stress.

6.5 Conclusion

This paper investigated the feasibility of the method estimating the stress in the α-Al_2O_3 thin film samples using RPS. A thin film of α-Al_2O_3 was deposited on low carbon steel and SiO_2 on silicon substrates at temperatures of 700 and 750 °C through PVD. The emission spectra of samples were obtained using RPS technique. Subsequently, the thermal residual stresses were estimated from the spectra using the piezo-spectroscopic coefficient. In this process, tensile and compressive stresses were measured from the α-Al_2O_3 thin film samples using RPS. The maximum estimated stress was 1.58 GPa (Compressive stress/Tensile stress) and the minimum estimated stress was 1.09 GPa (Compressive stress/Tensile stress). Furthermore, the estimated stress using RPS were compared with simulation results, and we found those results had similar trends for stress. Accordingly, RPS technique has potential to be applied to measure the stress of the civil-infrastructure. However, additional studies should be conducted for applying field experiments such as resolution problem and so on.

First, a study on Raman spectrometer hardware is needed. The performance of the spectrometer is closely related to the resolution of stress measurement. Therefore, spectral range and expected stress should be considered for the selection of an appropriate Raman spectrometer.

Second, a study on target materials is needed. We used α-Al_2O_3 thin film as target material in this study, but other materials can be investigated for the target materials. Therefore, the material should be selected with consideration for the type of structure. The stress transfer between the substrate and the target should especially be considered when selecting the target materials.

Third, in order to construct a reasonable finite element model, the growth stresses should be considered as well as the bonding condition for each layer.

References

1. Withers PJ, Bhadeshia HKDH (2001) Residual stress part 1 – measurement techniques. Mater Sci Technol 17:355–365
2. Forman RA, Piermarini GJ, Barnett JD, Block S (1972) Pressure measurement made by the utilization of ruby sharp-line luminescence. Science 176(4032):284–285
3. Grabner L (1978) Spectroscopic technique for the measurement of residual stress in sintered Al_2O_3. J Appl Phys 49(2):580–583
4. Lipkin DM, Clarke DR (1996) Measurement of the stress in oxide scales formed by oxidation of alumina-forming alloys. Oxid Met 45(3–4):267–280
5. Renusch D, Grimsditch M, Koshelev I, Veal BW, Hou PY (1997) Strain determination in thermally-grown alumina scales using fluorescence spectroscopy. Oxid Met 48(5–6):471–495
6. Pardo JA, Merino RI, Orera VM, Pena JI (2000) Piezospectroscopic study of residual stresses in Al_2O_3–ZrO_2 directionally solidified eutectics. J Am Ceram Soc 83(11):2745–2752
7. Dassios KG, Galiotis C (2004) Fluorescence studies of polycrystalline Al_2O_3 composite constituents: piezo-spectroscopic calibration and applications. Appl Phys Mater Sci Process 79(3):647–659
8. Wan KS, Tochino S, Zhu WL, Ohtsuka S, Pezzotti G (2010) Quantitative evaluation of probe response functions for Raman and fluorescence bands of single-crystalline and polycrystalline Al_2O_3. J Phys D Appl Phys 43(20):205501
9. Aruldhas G (2008) Molecular structure and spectroscopy, 2nd edn. PHI Learning, New Delhi
10. Pujala RK (2014) Dispersion stability, microstructure and phase transition of anisotropic nanodiscs. Springer International Publishing, Cham

Chapter 7
Smart Sensors: A Study of Power Consumption and Reliability

James Long, Jeffrey K. Swidrak, Michael Y. Feng, and Oral Buyukozturk

Abstract The development of wireless structural health monitoring systems utilising low-cost MEMS sensors, promises to make the deployment of large scale sensor networks for damage detection economically feasible. However, wireless transmission of full vibration time series is a potentially expensive and difficult bottleneck in the monitoring process. Smart sensors, equipped with microprocessors for computation, allow damage detection algorithms to be executed prior to the wireless transmission of data. This decentralised, parallel computing approach can condense the amount of data to be transmitted, potentially reducing power consumption and increasing transmission reliability. In this paper, several data-based damage detection algorithms are implemented on board a custom built MEMS sensor mote equipped with a microcontroller. A real campus building is instrumented with these sensors, and a quantitative study of the tradeoff between computation and transmission is conducted to investigate the advantages of carrying out part of the damage detection process at the sensor level.

Keywords Smart sensors • Structural health monitoring • Damage detection • Wireless sensor networks • Feature extraction

7.1 Introduction

The advantages of wireless sensor networks (WSNs) over wired networks for structural health monitoring are well documented. WSNs are potentially much easier to install and less expensive than traditional wired networks, and can be deployed in locations without the electrical and telecommunications services required for wired networks.

Initial studies on the use of WSNs for structural monitoring have understandably focused on the goal of emulating the performance of wired networks, by collecting data at sensor nodes and transmitting to a base station computer. Pakzad et al. [1] successfully deployed a network of 64 MEMS sensor nodes on the Golden Gate Bridge and showed that the acquired data could be used to accurately identify the vibration modes of the structures. While studies such as this have demonstrated the feasibility of using WSNs for structural monitoring, they have also highlighted issues with the centralised data acquisition model of monitoring. For example, in [1], the collection of 1,600 s of data at a 50 Hz sampling rate required 9 h for all sensor nodes to complete transmission.

Because power consumption is a key consideration for wireless sensor networks, lengthy transmission times are highly undesirable. One possible solution to this problem is to perform computation on board the sensor node prior to transmission, in order to reduce the volume of data. Rice et al. [2] developed a combined hardware software solution which enables the execution of modal analysis algorithms such as stochastic subspace identification and frequency domain decomposition within the sensor network.

J. Long (✉) • O. Buyukozturk
Department of Civil & Environmental Engineering, Massachusetts Institute of Technology, 77 Massachusetts Avenue, Cambridge, MA 02139, USA
e-mail: jjlong@mit.edu; obuyuk@mit.edu

J.K. Swidrak • M.Y. Feng
The Charles Stark Draper Laboratory, 555 Technology Square, Cambridge, MA 02139, USA
e-mail: jswidrak@draper.com; mfeng@draper.com

E.W. Sit (ed.), *Sensors and Instrumentation, Volume 5*, Conference Proceedings of the Society for Experimental Mechanics Series, DOI 10.1007/978-3-319-15212-7_7

However, in many cases, we may not be interested in conducting modal analysis, and the global nature of these techniques may complicate the execution of algorithms on board the sensor nodes. Farrar et al. [3] proposed a statistical pattern recognition paradigm for data based damage detection. In this paradigm, raw acceleration signals are processed into damage sensitive features. A database of these damage sensitive features is built, and new tests are compared to the database using statistical or machine learning techniques in order to detect damage.

Lynch et al. [4] adopted this approach for smart sensing, noting that if the features can be computed using only data from one sensor, the analysis can be completely decentralised and simplified. In [4], autoregressive analysis is embedded on board a sensor mote equipped with both an 8 bit and 32 bit microprocessor, and up to 50 % savings are achieved by computing the autoregressive coefficients prior to data transmission.

Since this study, the field of data-based damage detection has matured, and more sophisticated statistical and machine learning based methodologies have been developed, with smart sensing applications in mind. For example, Yao and Pakzad [5] combined autoregressive analysis for feature extraction, with Mahalanobis distance based statistical pattern recognition. Kesavan and Kiremidjian [6] suggest the use of wavelet analysis for feature extraction, and hypothesis testing for statistical pattern recognition. Long and Buyukozturk [7], propose the use of one class support vector machine based statistical pattern recognition.

Despite the evolution of data based damage detection, and discussion of its promise for smart sensing, since Lynch et al. [4], there has been little attention given to quantifying the benefits of embedding damage detection algorithms at the sensor node. In this paper we implement several damage detection algorithms on board a custom MEMS based wireless sensor node, and measure the power consumption required. These results are compared to the power required to transmit full time series of data from a 21 story reinforced concrete building, instrumented with 14 sensors.

7.2 Wireless Sensors and Network

A wireless network of 14 triaxial MEMS accelerometers has been installed in the interior of Building 54 (also known as the Green Building) on the MIT campus. As mentioned in the previous section, this is a 21 story reinforced concrete building with the 14 accelerometers installed in the following locations:

- two on the 18th floor,
- two on the 15th floor,
- two on the 12th floor,
- two on the 9th floor,
- two on the 6th floor,
- three on the 3rd floor, and
- one in the basement.

These locations are shown in Fig. 7.1. Each accelerometer has its own wireless mote and a microcontroller. In addition, six wireless motes without an accelerometer or microcontroller are spread throughout the building to serve as intermediate routers. For example, there is a wireless mote without a sensor located in a ventilation shaft to relay data from the basement node to the third floor nodes; the basement node cannot communicate with the manager, i.e. join the network, without this “hop” node. In general, we discovered these 802.15.4 compliant radios cannot transmit through more than three floors reliably.

All accelerometer data is transmitted back to a single node referred to as the manager located on the 6th floor midway between the two and six floor nodes. Accelerometer data is acquired simultaneously every 6 h for one minute at a 1 kHz sampling rate with 16-bit resolution. Only two of the three axes from each accelerometer are utilised to reduce data acquisition, storage, and transmission requirements. We omitted gravity-aligned acceleration, i.e. monitored two orthogonal axes in the plane of each floor, because gravity-aligned acceleration only occurs in rare seismic events. Therefore, each sensor node transmits 120,000 16-bit numbers to the manager after each data collection.

From our deployment on the Green Building, we allocated five minutes to each node to transmit its data set of 120,000 16-bit numbers back to the manager. In the Green Building deployment, end-to-end data transmission rates vary from 6,000 bits per second (bps) to 13,000 bps. Nodes that are more distant from the manager require almost all five minutes while those closer to the manager require about one minute. This is due to the data hopping from node to node to reach the manager. For example, data from the 12th floor is transmitted to the 9th floor and finally to the 6th floor. Even though we did not implement smart sensing on the Green Building, the Green Building deployment provided real world data transmission performance which was used to evaluate the tradeoff between local computation and data transmission.

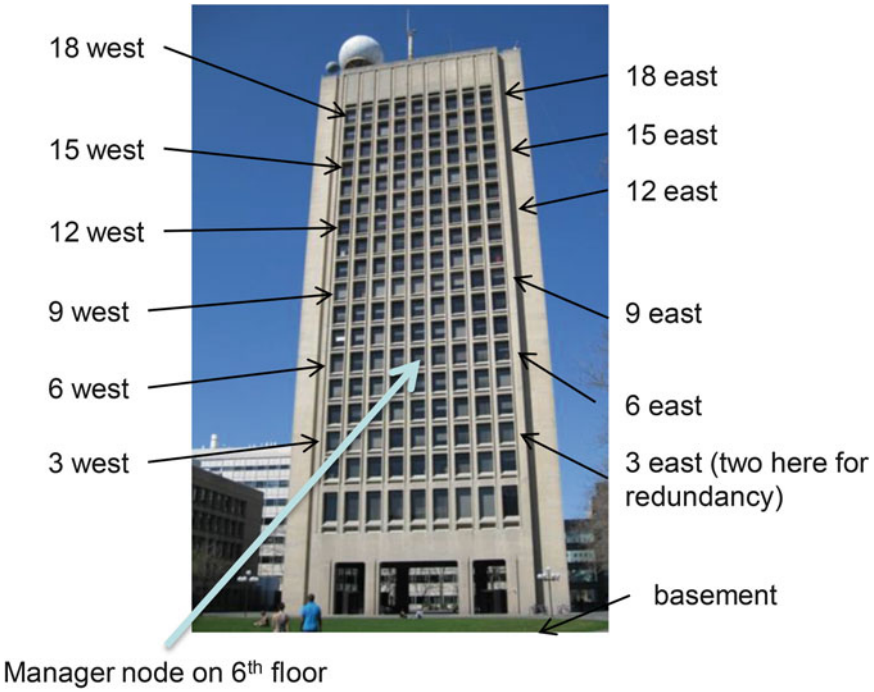

Fig. 7.1 Wireless sensor network on MIT's Green Building

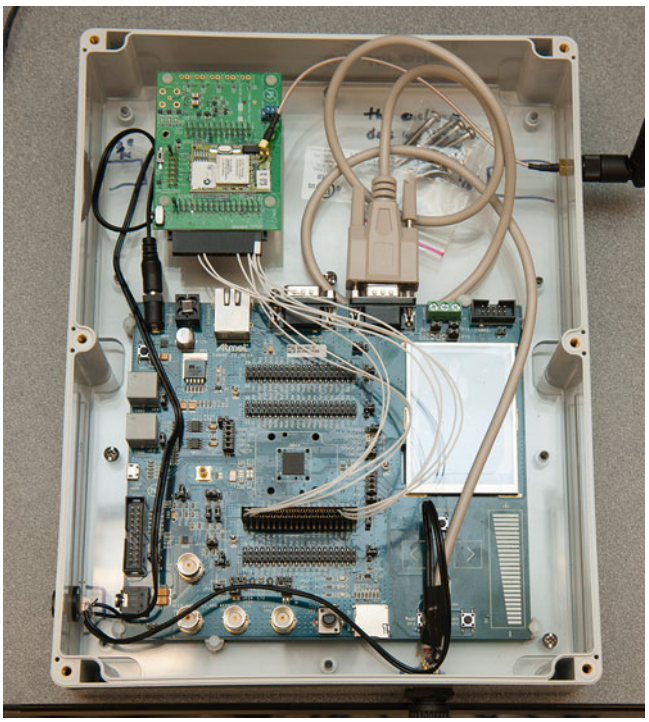

Fig. 7.2 SmartMesh IP wireless mote (circuit board in *upper left*) and SAM4E-EK microcontroller (*bottom*). Enclosure is 23 cm by 30 cm

As previously stated, each triaxial MEMS accelerometer is accompanied by a wireless mote and a microcontroller which are the two primary power consumers. For the Green Building network, we packaged the mote with the microcontroller into a single enclosure as shown in Fig. 7.2. The wireless mote performs the wireless data transmission while the microcontroller controls data acquisition, storage, and formatting for wireless transmission. This is the custom built MEMS sensor mote used for this study.

The wireless mote is an evaluation board for Linear Technology's SmartMesh IP wireless mote which conforms to IEEE 802.15.4e. This is a time slotted, channel hopping standard based on 6LoWPAN [8].

The microcontroller is the Atmel SAM4E-EK which is an evaluation kit for the SAM4E16E microcontroller. The SAM4E microcontroller family is based on the 32-bit ARM Cortex-M4 processor, and the SAM4E16E version was selected for its large 128 kB of SRAM, one of the largest available in a microcontroller. The large SRAM size is intended to execute a fast Fourier transform (FFT) on 10,000 16-bit numbers. The microprocessor also processes data quickly with a maximum clock speed of 120 MHz and has power sleep modes in the microwatt range.

7.3 Damage Detection

The goal of smart sensing is to reduce power consumption and increase system reliability, by interrogating data at the sensor location prior to wireless transmission. How the data is interrogated is clearly crucial to the attainment of this goal. The algorithms embedded at the sensor node must reduce the amount of data to be transmitted, while retaining meaning, and must do so without excessive use of energy for computation.

The distinction between modal analysis and damage detection is an important one for smart sensing. Modal analysis enables the characterisation of the vibration behaviour of a structure from the sensor data in terms of familiar mode shapes and frequencies, which have a clear physical interpretation. However, these quantities are inherently global in nature, requiring information from multiple sensor locations at once, and therefore complicating any smart sensing methodology.

If we are simply interested in knowing whether a structure has been damaged, rather than in understanding fully its dynamic behavior, a damage detection approach may be more appropriate than a full modal analysis. In this case, the implicit structural dynamics underlying the modal analysis approach may reduce sensitivity to local, nonlinear manifestations of damage in our sensor signals, and may require computation that does not improve our ability to detect changes in the structural system. Farrar et al. [3] proposed a paradigm for data-based damage detection, where acquired signals are first processed into features which are sensitive to damage, after which statistical tools are used to compare these features to baseline values, allowing us to infer whether damage may have occurred. This approach has been widely adopted by researchers in SHM, and its suitability for smart sensing has been noted [6, 7]. However, other than the study conducted by Lynch et al. [4] and discussed in the introduction of this paper, little investigation into the quantitative benefits of this type of approach has been conducted. In this paper, such a data-based approach is implemented on board a sensor mote.

7.3.1 Feature Extraction

The first step of data-based damage detection is feature extraction. Many methods exist which produce suitable features for damage detection, but the constraints of implementing these methods on a microcontroller limit the choice. Here, two methods are chosen, for their relative computational efficiency, and their compression properties.

7.3.1.1 Autoregressive Model

Lynch et al. [4], implemented the autoregressive model on board a sensor mote, and demonstrated significant power savings in computing and wirelessly transmitting the coefficients of this model, instead of the full time series. The autoregressive model of order p is given by:

$$x(t) = \sum_{k=1}^{p} \alpha_k x\,(t-k) + e_x(t) \tag{7.1}$$

where x(t) is an acceleration time series, α_k are the autoregression coefficients, p is the order of the model, and $e_x(t)$ is the residual error. As suggested by Lynch et al. [4], here we use the Burg method for estimating the coefficients of this model.

In addition to providing damage-sensitive features, by means of the coefficients of the model, the AR model provides a potential method for data compression. If lossy compression is acceptable, we can simply transmit the coefficients of the model, and recreate the time series according to Eq. 7.1. If the order of the model has been well chosen, a separate topic which is not considered here, the difference between the original and recreated signals, i.e. $e_x(t)$, may be acceptable. Even in the case of lossless compression, the residual error, $e_x(t)$, is likely to consist of much smaller numbers than the time series itself, and may therefore require fewer bits to transmit.

7.3.1.2 Discrete Wavelet Transform

Kesavan and Kiremidjian [6] proposed the use of the Continuous Wavelet Transform with a Daubechies mother wavelet of order 4 (DB4) as the mother wavelet, and showed its efficacy using simulated data from the ASCE benchmark structure. They also noted that the DB4 wavelet was a good choice as it has a Discrete Wavelet Transform (DWT) counterpart which would be more suitable for sensor level processing. It is important to note that although the DWT is much more computationally efficient than the Continuous Wavelet Transform, it may not be as sensitive to damage, as it does not provide the same resolution. Nonetheless, the DWT appears to be better suited to smart sensing applications, and it is implemented using the DB4 mother wavelet in this study.

We define the damage-sensitive features to be the energy contained at the individual DWT scales. For a signal of length n, which must be a power of 2, there will be $\log_2 n + 1$ wavelet scales. Because the first three scales contain so few points we concatenate them into one, leaving $\log_2 n - 1$ features. Similarly to the Autoregressive model, the DWT provides a convenient method for data compression, in addition to damage-sensitive feature extraction. Although the full DWT contains as many points as the original time series, the DWT representation is typically much sparser than the time domain. We can use this for either lossy compression, zeroing all elements less than a threshold, or lossless compression, taking advantage of the reduced bit requirement of smaller components. Therefore, as long as we do not delete the full DWT, we have the choice to use just the damage sensitive features, or to send a compressed DWT representation allowing reconstruction of the time series.

7.3.2 Microcontroller Implementation

7.3.2.1 System Overview

In the Green Building deployment, the two-axis accelerometer data is in the form of 16-bit unsigned words where each word represents acceleration in one axis. For this paper, 10,000 artificial data points in the same format as the Green Building deployment, i.e. raw 16-bit unsigned words, are used for all three tests: data transmission, the autoregressive model, and the Discrete Wavelet Transform. Three different embedded software programs running free RTOS were flashed onto the microcontroller to implement each test. Details of each microcontroller implementation are in the following subsections.

7.3.2.2 Data Transmission

To transmit the 10,000 16-bit unsigned words, the microcontroller retrieves the data from flash memory and then inserts the data into data packets following the SmartMesh IP API. SmartMesh IP transmits data on a packet-by-packet basis where the maximum payload is 84 bytes, i.e. 239 packets. After the microcontroller constructs the data packets, the data packets are sent over a serial interface to the SmartMesh IP mote for wireless transmission to the manager. A “transmission received” message is sent back to the originating mote informing the microcontroller if the message was sent successfully or if the data needs to be retransmitted. This process is repeated until all data has been transmitted successfully. The data being transmitted is the raw format and has not been converted into engineering units. The only constraint on how much data can be sent is the flash memory size, while only a small amount of SRAM is needed.

7.3.2.3 Fixed Point

The SAM4E microprocessor does contain a floating point processor. However, using the floating point processor on 10,000 data samples exceeds the 128 kB of SRAM and creates system errors. A fixed point library was developed that contains 1 sign bit, 15 integer bits, and 16 fraction bits. Both the Autoregressive Model and the Discrete Wavelet Transform are implemented with fixed point calculations rather than floating point calculations.

7.3.2.4 Autoregressive Model Algorithm

The Autoregressive (AR) model algorithm implementation on the microcontroller is performed on the 10,000 16-bit numbers that represent 10 s worth of artificial data. The data is first normalised by subtracting the minimum data value from all the data

points leaving a minimum value of zero in the data series. This data is then used to create fixed point arrays in SRAM that are used in a 10th order AR calculation. When doing the summation a 32 bit integer is used to prevent overflow. Otherwise, all calculations are done using fixed point. The maximum number of data points that can be used with this implementation is 10,000 (10 s at 1,000 Hz) due to SRAM constraints. An AR model of order 10 is estimated in this paper, meaning 10 coefficients need to be transmitted after execution of the algorithm.

7.3.2.5 Discrete Wavelet Transform Algorithm

The Discrete Wavelet Transform Algorithm is also implemented on the microcontroller. The raw artificial data which is in integer form is converted to its corresponding ADC voltage. The DWT requires a zero crossing to work, so conversion to ADC voltage, engineering units, or any other scaling that creates a zero crossing in the data series is necessary. In addition, the DWT requires the data series to be a power of 2 in length. The nearest power of 2 greater than 10,000 samples is 14, so the data series was increased to 2^{14}, i.e. 16,538 samples, by adding 6,538 zeroes. The maximum number of data points that can be used with this implementation is 16,384 due to SRAM constraints. After executing the DWT and computing the damage-sensitive features described in Sect. 7.3.1.2 we are left with 13 damage-sensitive features to be transmitted.

7.4 Power Measurement Test Unit

Because the microcontroller and mote are the two primary power consumers at each wireless node, and the proposed smart sensing trades wireless transmission power for data processing power, we modified a Green Building node shown in Fig. 7.2 to measure only the combined power of the microcontroller component and the mote. The modifications remove the unused functionality of the evaluation kit such as the CAN bus, LCD screen, RS232 transceiver, etc., in order to only measure the power of the microcontroller component itself. As mentioned in the previous section, we used artificial data to leave out the accelerometer to minimise unintended power consumption.

A GW Instek PST 3202 digital power supply provides 3.3 VDC directly to the microcontroller component and the mote in parallel. The digital power supply can measure current with a resolution of 1 mA; a second test instrument, a Keithley 2,700 multimeter, is placed in series with the 3.3VDC power input to measure the current feeding both the microcontroller component and the mote with sub-milliampere resolution.

The power measurement test unit is also located within 1 m of the manager, so wireless transmission is direct and unobstructed resulting in the highest transmission data rate possible with SmartMesh IP.

We measured the current in the three microcontroller implementations: (1) transmitting data at the maximum data rate, (2) the AR model, and (3) the DWT. The combined microcontroller and mote current for all three are listed in Table 7.1.

Examining the results in Table 7.1, we see that the execution of either the AR or DWT algorithm dramatically reduces the power consumed. Although the microcontroller requires more current to execute the algorithms, the time required is much higher for data transmission. The reduced operation time for execution of the AR and DWT algorithms prior to transmission ultimately leads to much lower power consumption.

Table 7.1 Current, processor time, and power consumption

Method	Combined microcontroller and mote current (mA)	Time to complete (seconds)	Combined power consumption (μA-hr)
Data transmission	22	6.5	40
Autoregressive model	32	0.4	3.6
Discrete wavelet transform	32	0.8	7.2

7.5 Results and Discussion

7.5.1 Transmission of Raw Data

Assuming the combined power consumption for the microcontroller and mote is the same regardless of the transmission time, we multiplied the power measured for data transmission on the Power Measurement Test Unit by various transmission times measured in the Green Building. The transmission times are calculated from the data transmission rates which are recorded in the Green Building deployment. These are listed in Table 7.2 along with the probable number of hops and the projected power consumption of transmission expressed in microampere-hours (μA-hr). The projected power consumption of an ideal RF environment which is represented by the laboratory tests with the Power Measurement Test Unit is also included.

Table 7.3 shows a comparison between estimated power consumption for wireless data transmission in a real deployment and 'smart sensing' execution of feature extraction algorithms prior to transmission. The power consumption figures for the AR and DWT are extrapolated from the laboratory measured figures shown in Table 7.1. The assumption here is that the 120,000 number sample is split into 12 segments of 10,000 numbers prior to algorithm execution. This is necessary as samples much larger than 10,000 numbers exceed the available internal microcontroller SRAM. We see that the improvements in power consumption achieved by interrogating the data prior to transmission are even more pronounced than in the laboratory setting.

7.6 Conclusions

In this paper we present quantitative evidence demonstrating that the execution of damage detection algorithms on a microprocessor prior to wireless transmission of data can reduce power consumption in wireless sensor networks. In particular, we compare running an autoregressive analysis and a discrete wavelet transform analysis with transmitting raw time series wirelessly, both in a lab and real life situation.

Under laboratory conditions, for a 10 s sample of data collected at 1,000 Hz, running the AR analysis prior to wireless transmission delivers a 11× reduction in power consumption. Under the same conditions the DWT analysis reduces power by a factor of 5.5 compared with transmission of the full time series. The DWT analysis results may be pessimistic in this case, because the time series length was not a power of 2, requiring zero padding, and as a result execution of the algorithm on a longer time series. This would be easily remedied by capturing a time series with a length equal to a power of 2.

When deployed on a real, 21 story, reinforced concrete building, wireless transmission rates are adversely affected, increasing transmission time, and as a result power consumed. In contrast, we do not expect algorithm execution to vary, and therefore conclude that smart sensing will be even more advantageous in a real life deployment.

Table 7.2 Projected power consumption levels for Green Building

Green building transmission path	Data transmission rate (bps)[a]	Transmission time for 120,000 16-bit numbers (seconds)	Probable # of hops	Projected power consumption (μA-hr)
18th floor to 6th floor manager	5,900	324	6	1,980
12th floor to 6th floor manager	6,900	278	4	1,700
6th floor mote to 6th floor manager	13,500	142	2	868
Laboratory setting (ideal RF environment)	25,000	77	1 (mote direct to manager)	471

[a]Reported data transmission rate for 10/6/14 at 6 p.m. at Green Building

Table 7.3 Comparison of projected power consumption of sensors in Green Building

Green building transmission path	Transmission of 120,000 16-bit numbers (μA-hr)	AR model (μA-hr)	DWT (μA-hr)
18th floor to 6th floor manager	1,980	43	86
12th floor to 6th floor manager	1,700	43	86
6th floor mote to 6th floor manager	868	43	86

In conclusion, a hardware implementation of two feature extraction methods for data-based damage detection has been presented in this paper. The advantages of this approach have been empirically demonstrated by measuring power consumption for data transmission and algorithm execution in both lab and real life situations. The smart sensing approach delivers significant power savings.

Acknowledgements The authors acknowledge the support provided by Royal Dutch Shell through the MIT Energy Initiative, and thank chief scientists Dr. Sergio Kapusta and Dr. Dirk Smit, project managers Dr. Keng Yap and Dr. Yile Li, and Shell-MIT liaison Dr. Jonathan Kane for their oversight of this work. Also, thanks to Brianna Klingensmith for assistance with the power measurement test unit.

References

1. Pakzad SN, Fenves GL, Kim S, Culler DE (2008) Design and implementation of scalable wireless sensor network for structural monitoring. J Infrastruct Syst 14(1):89–101
2. Rice JA, Mechitov K, Sim SH, Nagayama T, Jang S, Kim R, Fujino Y (2010) Flexible smart sensor framework for autonomous structural health monitoring. Smart Struct Syst 6(5–6):423–438
3. Farrar CR, Duffey TA, Doebling SW, Nix DA (1999) A statistical pattern recognition paradigm for vibration-based structural health monitoring. In: 241 Structural health monitoring 2000, Stanford, pp 764–773
4. Lynch JP, Sundararajan A, Law KH, Kiremidjian AS, Carryer E (2004) Embedding damage detection algorithms in a wireless sensing unit for operational power efficiency. Smart Mater Struct 13(4):800
5. Yao R, Pakzad SN (2012) Autoregressive statistical pattern recognition algorithms for damage detection in civil structures. Mech Syst Signal Process 31:355–368
6. Kesavan KN, Kiremidjian AS (2012) A wavelet-based damage diagnosis algorithm using principal component analysis. Struct Control Health Monit 19(8):672–685
7. Long J, Buyukozturk O (2014) Automated structural damage detection using one-class machine learning. Springer
8. Watteyne T, Doherty L, Simon J, Pister K (2013) Technical overview of SmartMesh IP. In: Seventh international conference on innovative mobile and internet services in ubiquitous computing (IMIS)

Chapter 8
A Model-Based Approach for the Dynamic Calibration of Torque Transducers

Leonard Klaus, Michael Kobusch, and Thomas Bruns

Abstract The demand for a traceable dynamic torque measurement increased over the last years. Procedures for a dynamic calibration of torque transducers have been developed in an European metrology research project. In the scope of this project, a dynamic measuring device was developed, and the corresponding mechanical modelling, which also includes the transducer under test, was investigated. The dynamic behaviour of the torque transducer is described by the parameters of its model. These model parameters will be identified from measurement data. The model-based approach for the description of the dynamic behaviour of torque transducers and model parameter identification procedures are described in this paper.

Keywords Dynamic calibration • Mechanical modelling • Model parameter identification • Dynamic measurement • Dynamic torque calibration

Nomenclature

Symbols

$\boldsymbol{D}$	damping matrix	$\mathrm{N \cdot m \cdot s / rad}$
f	frequency	Hz
J	mass moment of inertia	$\mathrm{kg \cdot m^2}$
$\boldsymbol{J}$	mass moment of inertia matrix	$\mathrm{kg \cdot m^2}$
$\boldsymbol{K}$	torsional stiffness matrix	$\mathrm{N \cdot m / rad}$
M	torque	$\mathrm{N \cdot m}$
$\boldsymbol{M}$	load matrix	$\mathrm{N \cdot m}$
n	rotational speed	$\mathrm{s^{-1}}$
P	mechanical power	W
U	voltage	V
t	time	s
λ	wavelength of light	m
φ	angle	rad
$\dot{\varphi}$	angular velocity	rad/s
$\ddot{\varphi}$	angular acceleration	$\mathrm{rad/s^2}$
$\boldsymbol{\varphi}$	angle vector	rad
$\dot{\boldsymbol{\varphi}}$	angular velocity vector	rad/s
$\ddot{\boldsymbol{\varphi}}$	angular acceleration vector	$\mathrm{rad/s^2}$
ω	angular frequency	$\mathrm{s^{-1}}$

L. Klaus (✉) • M. Kobusch • T. Bruns
Physikalisch-Technische Bundesanstalt (PTB), Bundesallee 100, 38116 Braunschweig, Germany
e-mail: leonard.klaus@ptb.de

E.W. Sit (ed.), *Sensors and Instrumentation, Volume 5*, Conference Proceedings of the Society for Experimental Mechanics Series, DOI 10.1007/978-3-319-15212-7_8

Abbreviations

DUT	Device under test
EMRP	European Metrology Research Programme
ICE	Internal combustion engine
LTI	Linear and time invariant
ODE	Ordinary differential equation

8.1 Introduction

The demand for a traceable measurement of dynamic torque signals has increased over the last few years. Up to now, no traceable calibration procedures exist. The same applies to other dynamical measurements of mechanical quantities, e.g. force and pressure. In the joint research project *Traceable Dynamic Measurement of Mechanical Quantities*, which was part of the European Metrology Research Programme (EMRP), nine national metrology institutes carried out joint research in the field of dynamic measurements from 2011 until 2014 [1, 2]. The investigation of a traceable dynamic calibration of torque transducers was part of this research project.

8.2 Need for Dynamic Calibration

Dynamic torque excitations exist in many fields of industry, but the greatest demand for dynamic calibration comes from the automotive industry. There are two important applications with dynamic torque signals, which suffer from lack of traceability in particular.

8.2.1 Screw Fastening Tools

For the production of high quality industrial goods, automatic screw fastening systems are frequently used in assembly lines. They are supposed to fasten screw connections quickly to a specified torque. For safety-relevant connections, a traceable measurement of the fastening torque is necessary. Typical tools for this type of industrial application are impulse wrenches. They fasten the screw connection by applying a sequence of short impulses generated by the release of a pressurised hydraulic fluid. A typical torque pulse is depicted in Fig. 8.1a. The steep pulses limit the operator's exposition to the high fastening

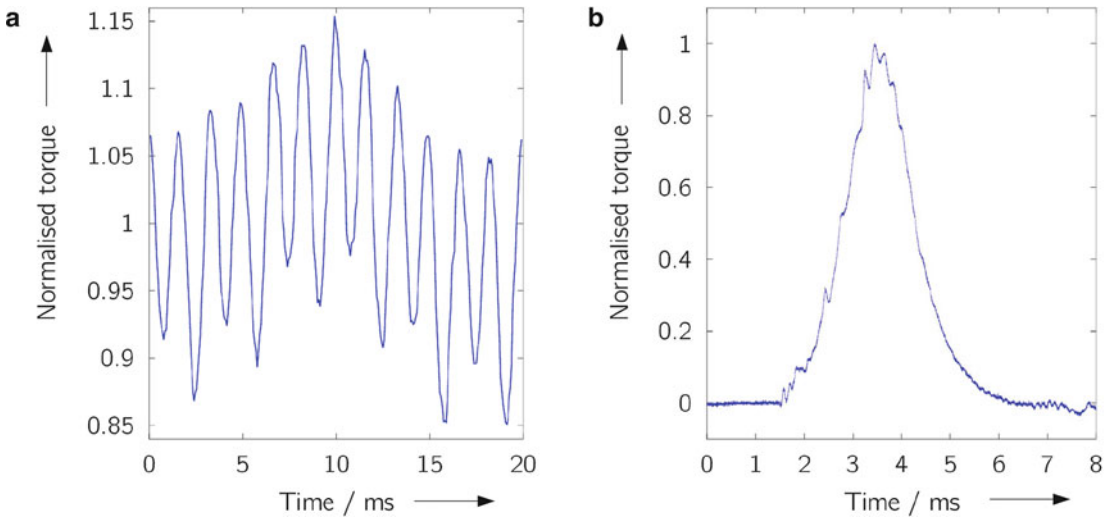

Fig. 8.1 (**a**) Torque output of an impulse wrench and (**b**) of an electric synchronous motor (courtesy of Working Group 3.52 of PTB)

torque due to the tools' inertia. Additionally, these tools feature short fastening times and good reproducibility of the fastening torque. The pulses are in the range of milliseconds and, therefore, have a frequency content of up to several hundred Hertz in the torque output. The generated torque level can range from some Newtonmetres to one Kilonewtonmetre.

8.2.2 Mechanical Output Power Measurements

The mechanical output power P of internal combustion engines (ICE) as well as of electric motors can be measured by means of the rotational speed n and the torque M following

$$P = M \cdot n. \tag{8.1}$$

The torque output of combustion engines is highly fluctuating over time. But electric motors generate dynamic torque components as well. Due to influences from power converters, high frequency torque components can appear in the torque output of electric motors (see Fig. 8.1b). The frequency content of these dynamic components typically ranges from several hundred Hertz, to some Kilohertz both for ICEs and for electric motors. The torque output can amount up to several Kilonewtonmetres.

The higher demands for low emission and for high efficiency, respectively, require a precise measurement of the output power of automotive ICEs, but of electric motors as well.

8.3 Measuring Device

The demands for higher precision in torque measurement require the comprehension of dynamic effects. In order to perform a dynamic calibration of torque transducers, a dedicated measuring device was developed [3]. The device and its working principle are depicted in Fig. 8.2.

The measurement principle is based on Newton's second law. The generated dynamic torque $M(t)$ can be measured by means of the angular acceleration $\ddot{\varphi}(t)$ and the mass moment of inertia J giving

$$M(t) = \ddot{\varphi}(t) \cdot J \tag{8.2}$$

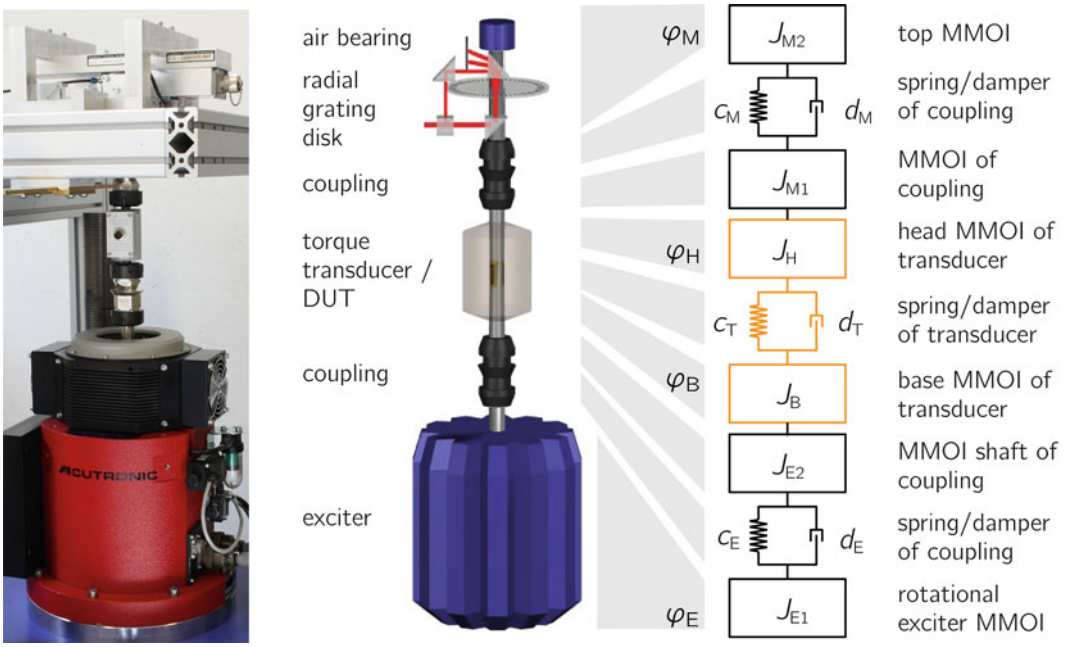

Fig. 8.2 Dynamic torque measuring device (*left*), its schematic representation (*middle*) and model description (*right*), the components of the transducer are marked in *orange*, those of the measuring device are marked in *black*

The dynamic torque is generated by a rotational exciter using monofrequent sinusoidal signals. The mechanical design of the dynamic torque measuring device features a vertical drive shaft connected to further components in series arrangement, which are exposed to the forced rotational excitation. On the bottom, the rotational exciter is mounted on an adjustable platform that can be moved vertically. The transducer under test (device under test, DUT) is mounted between two couplings on top of the rotational exciter. Both couplings are torsionally stiff but flexible to bending, in order to reduce influences from bending moments and lateral forces to the transducer under test. At the top end of the drive shaft, the arrangement of an air bearing and a radial grating disk enables a precise measurement of the time-dependent angular position providing low friction to the rotational oscillations. All components mounted at the top of the transducer under test contribute to the acting mass moment of inertia of Eq. (8.2).

The measurement of the angular position at the top is carried out by a rotational heterodyne Doppler interferometer measuring through the aforementioned radial grating disk. The two laser beams are diffracted by the grating lines, and the first diffraction order is coupled back into the interferometer. At each passing of a grating line, the laser beam with a wavelength λ exhibits a phase shift of 2π, which is analysed for the measurement.

The angular acceleration at the bottom of the transducer is measured by means of an angular accelerometer embedded in the rotor of the rotational exciter.

When carrying out measurements, the rotational excitations on top and on bottom of the drive shaft are acquired simultaneously sampling the output voltage of the transducer successively for different excitation frequencies. These frequencies were chosen according to the recommendations of ISO 266 [4]. All three acquired signals are approximated with a sine-fit of common frequency. For this purpose, the signals are normalised to avoid unwanted weighting effects due to the different numerical magnitudes of the acquired signals. The applied algorithm is a Levenberg-Marquardt nonlinear least squares approach.

8.4 Model

The dynamic behaviour of the torque transducer under test is described by an appropriate mechanical model. Such a model-based approach for the dynamic calibration is necessary, because all torque transducers are coupled to their mechanical environment on both sides at the time of measurement. The mechanically coupled components may influence the transducer's dynamic behaviour.

The model of the transducer is linear and time invariant (LTI). The assumption of a LTI behaviour is valid, because the transducers are designed to be linear and stable over time, which was investigated for static calibration purposes already. The majority of torque transducers use a measuring principle based on strain gages, which leads to a characteristic mechanical design. The transducers are designed to be torsionally stiff, but the measuring element sensing the strain generated by the acting torque is comparably compliant. Therefore, the basic model of the transducer consists of two rigid mass moment of inertia elements connected by a torsional spring and a torsional damper in parallel (see Fig. 8.2).

To be able to identify the transducer's model parameters, the mechanical environment needs to be taken into account. Therefore, the basic model of the torque transducer was extended to a model of the transducer and the measuring device, which is—in case of the calibration—the mechanical environment. The extended model, which includes the measuring device and the transducer under test, is again LTI. The model components were chosen corresponding to the components of the measuring device, to establish a physical model of the whole measuring set-up.

8.5 Model Parameter Identification Procedure

The calibration of the torque transducer under test is going to be carried out by identifying its model parameters by means of measured data. To do so, a sufficiently low number of unknown parameters of the model is desired. Therefore, the model parameters of the measuring device need to be determined prior to the model parameter identification of the DUT as far as possible.

For the purpose of the identification of the model properties of the measuring device, three auxiliary measurement set-ups for the measurands torsional stiffness, mass moment of inertia [5] and rotational damping [6] were developed. With the measurement results from these set-up, all required model parameters of the measuring device were determined. The known and unknown model parameters of the measuring device and of the device under test are given in Table 8.1.

Table 8.1 Model parameters of the measuring device and the transducer under test

	Known model parameters	Unknown model parameters
Mass moment of inertia	J_{M2}, J_{M1}, J_{E2}	J_B, J_H
Torsional stiffness	c_M, c_E	c_T
Damping	d_M, d_E	d_T

The model is mathematically described as an inhomogeneous ordinary differential equation system (ODE) giving

$$\boldsymbol{J} \cdot \ddot{\boldsymbol{\varphi}} + \boldsymbol{D} \cdot \dot{\boldsymbol{\varphi}} + \boldsymbol{K} \cdot \boldsymbol{\varphi} = \boldsymbol{M} \tag{8.3}$$

with the mass moment of inertia matrix $\boldsymbol{J}$, the torsional stiffness matrix $\boldsymbol{K}$ and the damping matrix $\boldsymbol{D}$. The angle vector $\boldsymbol{\varphi}$ describes the angle excitations at different positions in the model, the derivatives $\dot{\boldsymbol{\varphi}}$, $\ddot{\boldsymbol{\varphi}}$ the angular velocity and angular acceleration, respectively. The excitation by the rotational exciter is described by the load matrix $\boldsymbol{M}$. For the model of the measuring device and the device under test, the resulting matrices are the following:

$$\boldsymbol{J} = \begin{bmatrix} J_{M2} & 0 & 0 & 0 \\ 0 & (J_{M1} + J_H) & 0 & 0 \\ 0 & 0 & (J_B + J_{E2}) & 0 \\ 0 & 0 & 0 & J_{E1} \end{bmatrix} \quad \boldsymbol{D} = \begin{bmatrix} d_M & -d_M & 0 & 0 \\ -d_M & (d_M + d_T) & -d_T & 0 \\ 0 & -d_T & (d_T + d_E) & -d_E \\ 0 & 0 & -d_E & d_E \end{bmatrix} \tag{8.4a}$$

$$\boldsymbol{C} = \begin{bmatrix} c_M & -c_M & 0 & 0 \\ -c_M & (c_M + c_T) & -c_T & 0 \\ 0 & -c_T & (c_T + c_E) & -c_E \\ 0 & 0 & -c_E & c_E \end{bmatrix} \tag{8.4b}$$

$$\boldsymbol{\varphi} = \begin{bmatrix} \varphi_M(t) \\ \varphi_H(t) \\ \varphi_B(t) \\ \varphi_E(t) \end{bmatrix} \quad \dot{\boldsymbol{\varphi}} = \begin{bmatrix} \dot{\varphi}_M(t) \\ \dot{\varphi}_H(t) \\ \dot{\varphi}_B(t) \\ \dot{\varphi}_E(t) \end{bmatrix} \quad \ddot{\boldsymbol{\varphi}} = \begin{bmatrix} \ddot{\varphi}_M(t) \\ \ddot{\varphi}_H(t) \\ \ddot{\varphi}_B(t) \\ \ddot{\varphi}_E(t) \end{bmatrix} \quad \boldsymbol{M} = \begin{bmatrix} 0 \\ 0 \\ 0 \\ M(t) \end{bmatrix} \tag{8.4c}$$

Based on this ODE system, the unknown model parameters can be identified by means of the measurement data. For this purpose, it is recommended to acquire all angle positions, angular velocities and angular accelerations given in $\boldsymbol{\varphi}$, $\dot{\boldsymbol{\varphi}}$ and $\ddot{\boldsymbol{\varphi}}$. The excitation with harmonic oscillations (sinusoidal signals) with known angular frequencies $\omega = 2\pi f$ makes it possible to calculate the wanted angle quantities from one measured angle, angular velocity or angular acceleration and vice versa as follows

$$\begin{aligned} \varphi(t) &= \hat{\varphi}\, \mathrm{e}^{\mathrm{i}\omega t} \\ \dot{\varphi}(t) &= \mathrm{i}\omega\, \hat{\varphi}\, \mathrm{e}^{\mathrm{i}\omega t} = \mathrm{i}\omega\, \varphi(t) \\ \ddot{\varphi}(t) &= -\omega^2\, \hat{\varphi}\, \mathrm{e}^{\mathrm{i}\omega t} = -\omega^2 \varphi(t), \end{aligned} \tag{8.5}$$

where $\mathrm{i} = \sqrt{-1}$ denotes the imaginary number.

Technically it is not possible to acquire angle information at all desired positions given in $\boldsymbol{\varphi}$, $\dot{\boldsymbol{\varphi}}$ and $\ddot{\boldsymbol{\varphi}}$. The angle excitation on top and on bottom of the transducer can not be measured directly, but it can be derived from the output signal of the torque transducer. The output signal of the torque transducer is assumed—due to its linear behaviour—to be proportional to the input torque. Strain gage transducers measure strain generated by torsion, therefore the output voltage is proportional to the angle difference $\Delta\varphi_{HB}$ on top and on bottom of the transducer.

$$U(t) \propto M(t) \propto \Delta\varphi_{HB}(t). \tag{8.6}$$

Applying the proportionality parameter ρ gives the direct relation of the measured output voltage and the torsion of the transducer as

$$U(t) = \rho \cdot \Delta\varphi_{HB}(t). \tag{8.7}$$

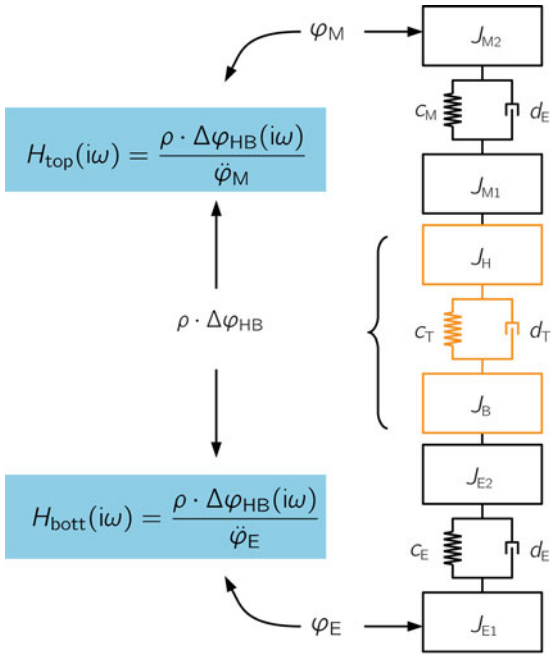

Fig. 8.3 Transfer functions based on the acquired measurands

Two complex frequency response functions can be derived [7] from the acquired signals, which are shown in Fig. 8.3. The frequency response functions consist of the mechanical input of the top part or the bottom part of the measuring device and of the output of the transducer. For the response function of the top part of the measuring device $H_{\mathrm{top}}(\mathrm{i}\omega)$, the frequency response of transducer output and angular acceleration on the top is calculated, and the frequency response of the bottom part of the measuring device $H_{\mathrm{bott}}(\mathrm{i}\omega)$ relate the output signal of transducer and the angular acceleration of the bottom.

The corresponding model parameters for each of the input quantities of the frequency response functions can be derived from the ODE system (cf. Eqs. (8.3), (8.4a), (8.4b), (8.4c)). These two frequency response functions comprise all unknown parameters of the device under test. It is possible to derive J_{H}, c_{T}, d_{T} and ρ from $H_{\mathrm{top}}(\mathrm{i}\omega)$ giving

$$H_{\mathrm{top}}(\mathrm{i}\omega) = -\rho \cdot \frac{J_{\mathrm{M2}} + (J_{\mathrm{M1}} + J_{\mathrm{H}}) \cdot K_{\mathrm{t}}(\mathrm{i}\omega)}{\mathrm{i}\omega d_{\mathrm{T}} + c_{\mathrm{T}}} \tag{8.8}$$

with K_{t} as a set of known parameters of the top part of the measurement device

$$K_{\mathrm{t}}(\mathrm{i}\omega) = \frac{\varphi_{\mathrm{H}}}{\varphi_{\mathrm{M}}} = \frac{\omega^2 J_{\mathrm{M2}} + \mathrm{i}\omega d_{\mathrm{M}} + c_{\mathrm{M}}}{\mathrm{i}\omega d_{\mathrm{M}} + c_{\mathrm{M}}}. \tag{8.9}$$

With K_{b} consisting only of known parameters of the bottom part of the measuring device as

$$K_{\mathrm{b}}(\mathrm{i}\omega) = \frac{\omega^2 J_{\mathrm{E2}} + \mathrm{i}\omega d_{\mathrm{E}} + c_{\mathrm{E}}}{\mathrm{i}\omega d_{\mathrm{E}} + c_{\mathrm{E}}}, \tag{8.10}$$

the transfer function of the bottom parts $H_{\mathrm{bott}}(\mathrm{i}\omega)$ gives

$$\begin{aligned} H_{\mathrm{bott}}^{-1}(\mathrm{i}\omega) = {} & \frac{\omega^2}{\rho} \cdot \left(\frac{-\omega^2 J_{\mathrm{B}}}{\mathrm{i}\omega d_{\mathrm{E}} + c_{\mathrm{E}}} + \frac{\mathrm{i}\omega d_{\mathrm{T}} + c_{\mathrm{T}}}{\mathrm{i}\omega d_{\mathrm{E}} + c_{\mathrm{E}}} + K_{\mathrm{b}}(\mathrm{i}\omega) \right) \\ & - \frac{K_{\mathrm{t}}(\mathrm{i}\omega)}{\rho} \cdot \left(\frac{\left(\frac{-\omega^2 J_{\mathrm{B}}}{\mathrm{i}\omega d_{\mathrm{E}} + c_{\mathrm{E}}} + K_{\mathrm{b}}(\mathrm{i}\omega) \right) \cdot (\mathrm{i}\omega d_{\mathrm{T}} + c_{\mathrm{T}})}{J_{\mathrm{M2}} + (J_{\mathrm{M1}} + J_{\mathrm{H}}) \cdot K_{\mathrm{t}}(\mathrm{i}\omega)} \right). \end{aligned} \tag{8.11}$$

For better readability, the inverse function $H_{\mathrm{bott}}(\mathrm{i}\omega)^{-1}$ is displayed. From this frequency response function, the unknown parameters J_{H}, J_{B}, c_{T}, d_{T} and ρ can be derived. Detailed information about the identification process is given in [7].

The model parameter identification can use least squares procedures and will be carried out in frequency domain. Equations (8.8) and (8.11) for the system descriptions are the basis for the model parameter identification. The model is nonlinear in the parameters, which means that it will be necessary to use corresponding algorithms. Nonlinear regression problems can not be solved directly, they require an iterative process for an estimation of the solution.

Both frequency response equation will be included in the parameter identification process and will used together in one run. The parameter identification will be carried out with the complex measurement data both for the real and imaginary parts of the frequency response equations.

8.6 Influences of Electronic Components in the Measuring Chain

The data needed for the model parameter identification should contain only information of the mechanical system. Therefore, all influences from electronic components in the signal acquisition chain need to be measured first and then compensated for prior to the model parameter identification. This includes the measuring components for the measurement of angle and angular acceleration, signal conditioning amplifiers, filters and analogue-to-digital converters.

Angle measurement/Angular acceleration sensor The measurement of the angle increment is carried out by means of a heterodyne interferometer and software demodulation. With the software demodulation, influences from the electronics can be avoided, and the only remaining influences are the deviations in the grating, the laser wavelength λ and the precision of the time/frequency measurement.

The angular acceleration sensor was calibrated using primary methods. For this purpose, a prism was mounted in a known distance from the axis of rotation. The displacement of the prism was measured by interferometric methods.

Bridge amplifiers The strain gages in the transducers under test are arranged as a Wheatstone bridge. The signal conditioning of those circuits is carried out with bridge amplifiers. For a dynamic calibration of those amplifiers, a dynamic bridge standard was developed at PTB [8]. The dynamic bridge standard enables a dynamic calibration in a frequency range from DC (0 Hz) up to 10 kHz. A more comprehensive overview for the dynamic calibration of measuring amplifiers, including dynamic calibration results for different bridge amplifiers, can be found in [9].

The influences of the conditioning electronics need to be analysed not only for stand-alone bridge amplifiers used with passive torque transducers, but for transducers with integrated electronics need to be analysed as well. This can be difficult, because some transducers are sealed and the access to the circuit board is not possible due to their mechanical design.

Analogue digital converters The analogue digital converters used for the voltage acquisition were calibrated with a Fluke 5700A calibrator. The timing of all channels was compared to PTB's distributed frequency standard.

For each component, the complex frequency response function $H(\mathrm{i}\omega)$ was calculated based on the calibration results with the input $X(\mathrm{i}\omega)$ and the output $Y(\mathrm{i}\omega)$ as

$$H(\mathrm{i}\omega) = \frac{Y(\mathrm{i}\omega)}{X(\mathrm{i}\omega)}. \tag{8.12}$$

Based on the calibration results, the magnitude $A(\omega)$ and the phase $\varphi(\omega)$ of the complex frequency response can be derived.

$$A(\omega) = |H(\mathrm{i}\omega)| = \sqrt{\mathrm{Re}\,(H(\mathrm{i}\omega))^2 + \mathrm{Im}\,(H(\mathrm{i}\omega))^2} \tag{8.13}$$

$$\varphi(\omega) = \arctan\left(\frac{\mathrm{Im}\,(H(\mathrm{i}\omega))}{\mathrm{Re}\,(H(\mathrm{i}\omega))}\right) \tag{8.14}$$

The measurement data Y_{meas} can now be corrected in the frequency domain either for magnitude A and phase φ

$$A_{\mathrm{corr}}(\omega) = A_{\mathrm{meas}}(\omega) \cdot A_{\mathrm{calib}}(\omega)^{-1} \;\text{ and }\; \varphi_{\mathrm{corr}}(\omega) = \varphi_{\mathrm{meas}}(\omega) - \varphi_{\mathrm{calib}}(\omega), \tag{8.15}$$

or for complex signals

$$Y_{\mathrm{corr}}(\mathrm{i}\omega) = Y_{\mathrm{meas}}(\mathrm{i}\omega) \cdot H_{\mathrm{calib}}(\mathrm{i}\omega)^{-1} \tag{8.16}$$

applying a multiplication with the inverse complex frequency response function $H_{\mathrm{calib}}(\mathrm{i}\omega)$.

8.7 Measurement Results

In preparation of the model parameter identification, measurements with different transducers were carried out. The chosen transducers have different mechanical designs, different torque capacities and, therefore, represent the whole range of transducers which could be calibrated in the dynamic torque measuring device.

Three different types of transducers were chosen (see Fig. 8.4).

Shaft type torque transducer of 1 N · m: This very low capacity transducer fits very well to the measuring device's torque generation capabilities. However, it has non-contact signal conditioning and transmission electronics included, which can not be calibrated without a complete disassembly of the transducer.

Shaft type torque transducer of 10 N · m: This passive transducer features direct access to the Wheatstone bridge via slip-rings. It was possible to connect a dynamically calibrated bridge amplifier and therefore to correct for the amplifier's dynamic behaviour.

Flange type torque transducer of 50 N · m: This transducer has the highest capacity of the analysed transducers and has—due to its mechanical design—a high torsional stiffness and a large mass moment of inertia. The torque signals are conditioned by a bridge amplifier in the rotor and transmitted by a telemetry system. The electronic components of an identical transducer were calibrated, because the transducers are sealed and can not be opened without causing damage. Based on the calibration data, the influences of the electronics can be corrected.

The measurement results of the three analysed transducers are depicted in Figs. 8.5, 8.6 and 8.7. The frequency response functions for the top and for the bottom of each transducer are given in magnitude and in phase.

Each transducer was analysed in the dynamic torque measuring device. Depending on the properties (torsional stiffness, mass moment of inertia) of the transducer, the frequency response will behave in a characteristic manner. Frequencies higher than the resonance frequency of the drive shaft are difficult to excite because of a declining sensitivity at the top. The higher the frequency, the smaller is the relative magnitude at the top of the measuring device. Therefore practical frequency limit exists somewhat beyond the transducer's resonance frequency in the given configuration. Moreover, even before this limit is reached, the magnitudes of excitation at the top ($\ddot{\varphi}_{\mathrm{M}}$) will be very small and will show comparably high noise levels causing deviations in the sine fit results.

It gets obvious from the experimental measurement results that knowledge about the influence of the signal conditioning electronics is essential. The frequency response function of the low capacity transducer (see Fig. 8.5) has, despite of the comparably small range of excitation frequencies, clearly a phase lag which can not be explained by mechanical influences. These effects can not be found in the results of the two other transducers, where the influences from signal conditioning is compensated.

Fig. 8.4 Analysed torque transducers, 1 N • m shaft type (*left*), 10 N • m shaft type (*middle*), and 50 N • m flange type (*right*).

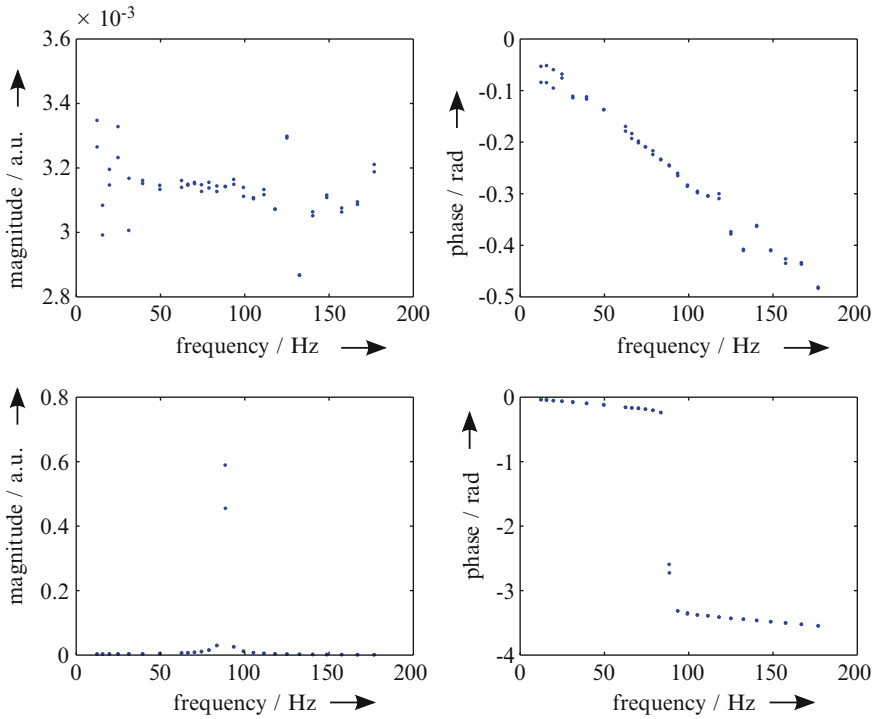

Fig. 8.5 Frequency response function H_{top} (*top*) and H_{bott} (*bottom*) in magnitude and phase measured with a shaft type transducer of 1 N • m nominal load

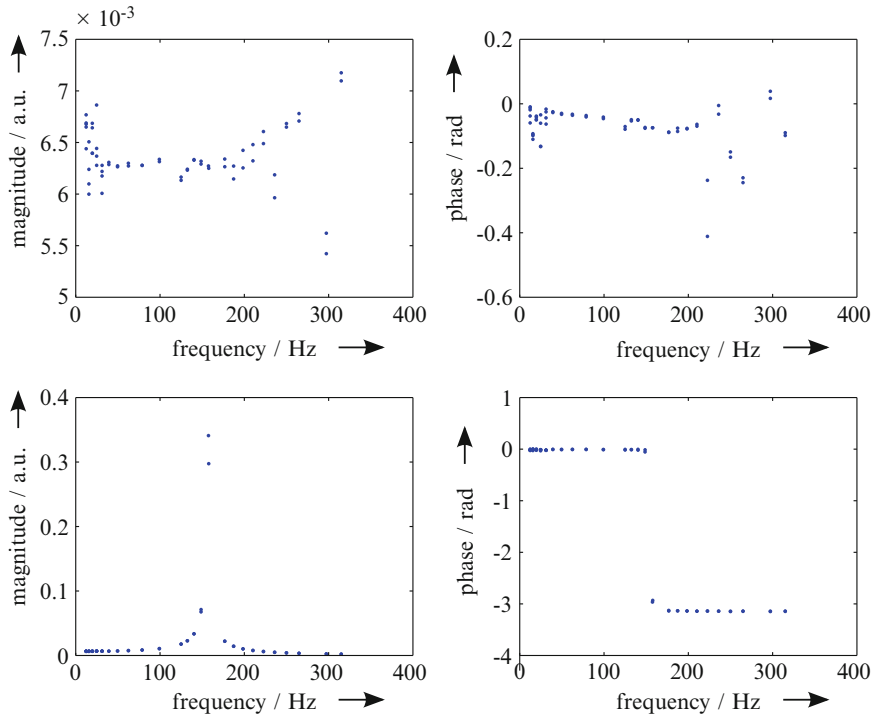

Fig. 8.6 Frequency response function H_{top} (*top*) and H_{bott} (*bottom*) in magnitude and phase measured with a shaft type transducer of 10 N • m nominal load

8.8 Simulation Results

The frequency response of the modelled system was analysed using calculated simulations. For this purpose, the two frequency response functions were calculated using Eqs. (8.8) and (8.11). The mechanical properties of the measuring device (i.e. the known model parameters from Table 8.1) were used to compute the frequency response functions with expected parameters of transducers. The result for the 10 N m shaft type transducer can be found in Fig. 8.8.

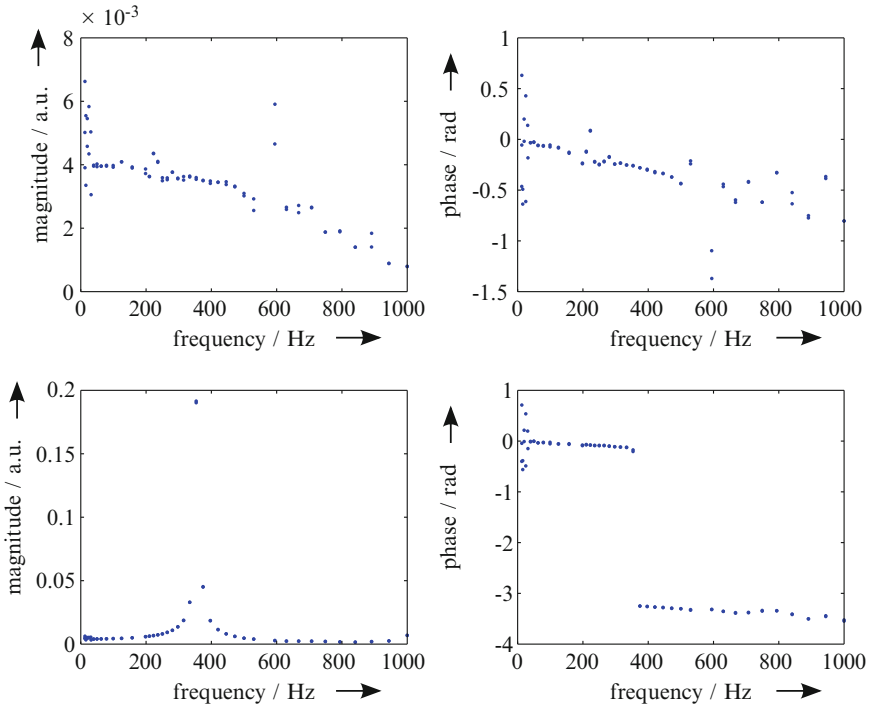

Fig. 8.7 Frequency response function H_{top} (*top*) and H_{bott} (*bottom*) in magnitude and phase measured with a flange type transducer of 50 N • m nominal load

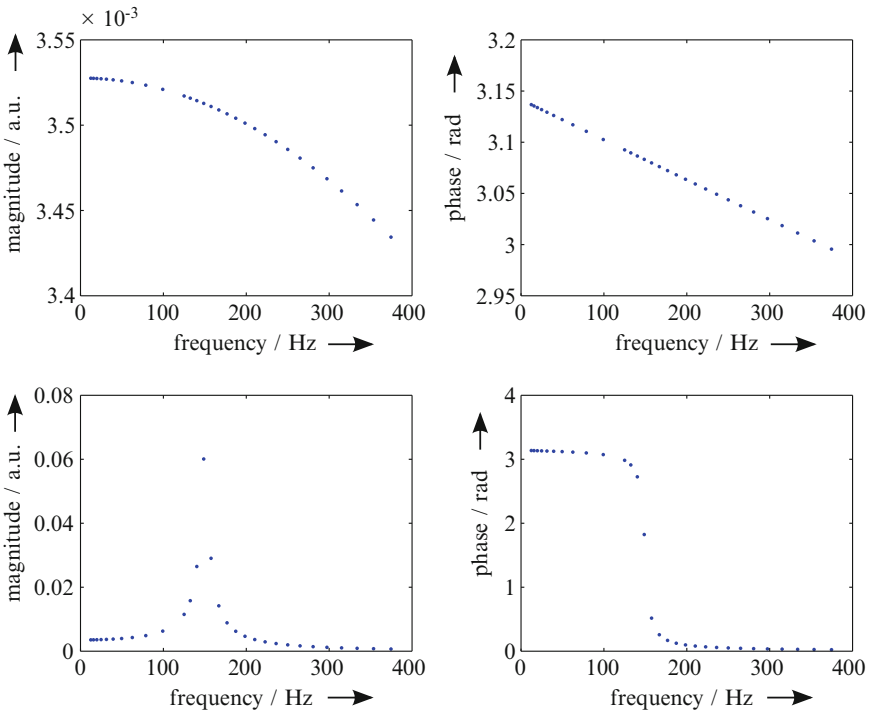

Fig. 8.8 Simulation results for the 10 N • m shaft type transducer. Frequency response function H_{top} in magnitude and phase (*top*), frequency response function H_{bott} in magnitude and phase (*bottom*).

A good agreement between the results of simulation and the measurement are found. A sensitivity analysis of the resulting frequency response functions to changes in parameters showed that only those parameter changes are good to be identified which affect the frequency response function of the whole drive shaft correspondingly [10]. The influence of the parameters of the device under test on the frequency responses are therefore dependent on the mechanical design of the measuring device as well.

8.9 Conclusions

A dynamic calibration of torque transducers is important for various applications in industry, in particular for efficiency measurement of electric motors and internal combustion engines, as well as for screw fastening tools with dynamic torque outputs.

In this paper, a model-based approach for the description of torque transducers, a measuring device and the corresponding model description of the transducer under test is presented. Procedures for the compensation of the effects of signal conditioning and transmission electronics are explained. The model parameter identification using two frequency response functions of the measuring device and a nonlinear least-squares approximation enables a determination of the properties of the transducer under test by means of measurement data. Dynamic measurement results of three torque transducers demonstrate capability and limitations of the actual measuring setup. Calculations of simulated system responses calculations confirm the model assumptions of a torsional spring-mass-damper system.

Acknowledgements The authors would like to thank their colleague Barbora Arendacká from Working Group 8.42 *Data Analysis and Measurement Uncertainty* of PTB for the helpful recommendations and the support for system simulation and model parameter identification.

This work is part of the Joint Research Project IND09 *Traceable Dynamic Measurement of Mechanical Quantities* of the European Metrology Research Programme (EMRP). The EMRP is jointly funded by the EMRP participating countries within EURAMET and the European Union.

References

1. Bartoli C, et al. (2013) Traceable dynamic measurement of mechanical quantities: objectives and first results of this European project. Int J Metrol Qual Eng 3(3):127–135. doi:10.1051/ijmqe/2012020
2. Bartoli C, et al. (2014) Dynamic calibration of force, torque and pressure sensors. In: Proceedings of joint IMEKO international TC3, TC5 and TC22 conference 2014, Cape Town, South Africa, Feb 2014
3. Bruns T (2003) Sinusoidal torque calibration: a design for traceability in dynamic torque calibration. In: Proceedings of XVII IMEKO world congress–metrology in the 3rd millennium, Dubrovnik, Croatia, Jun 2003
4. ISO TC 43, ISO 266:1997, Acoustics: preferred frequencies for measurements. International Organization for Standardization (ISO), Geneva, Switzerland, 1997
5. Klaus L, Bruns T, Kobusch M (2012) Determination of model parameters for a dynamic torque calibration device. In: Proceedings of XX IMEKO world congress, Busan, Republic of Korea, Sep 2012
6. Klaus L, Kobusch M (2014) Experimental method for the non-contact measurement of rotational damping. In: Proceedings of joint IMEKO international TC3, TC5 and TC22 conference 2014, Cape Town, South Africa, Feb 2014
7. Klaus L, Arendacká B, Kobusch M, Bruns T (2014) Model parameter identification from measurement data for dynamic torque calibration. In: Proceedings of joint IMEKO international TC3, TC5 and TC22 conference 2014, Cape Town, South Africa, Feb 2014
8. Beug MF, Moser H, Ramm G (2012) Dynamic bridge standard for strain gauge bridge amplifier calibration. In: Proceedings of conference on precision electromagnetic measurements (CPEM), pp 568–569, Washington DC, United States, Jul 2012. doi:10.1109/CPEM.2012.6251056
9. Klaus L, Bruns T, Volkers H (2015) Calibration of bridge-, charge- and voltage amplifiers for dynamic measurement applications. Metrologia 52(1):72–81. doi:10.1088/0026-1394/52/1/72
10. Klaus L, Arendacká B, Kobusch M, Bruns T (2015) Dynamic torque calibration by means of model parameter identification, ACTA IMEKO (2015 in press)

Chapter 9
Smart Tyre Induced Benefits in Sideslip Angle and Friction Coefficient Estimation

F. Cheli, D. Ivone, and E. Sabbioni

Abstract Smart tyres are an emerging technology able to turn tyres into sensors able to provide information about tyre-road contact. It is straightforward to understand how this technology can promote the development of new active control strategies and/or improve the present ones through the enhancement of estimation of unknown quantities, such as tyre-road friction coefficient and vehicle sideslip angle which are crucial for stability and safety control systems (ABS, ESP, etc.). Specifically the present paper investigates how smart tyres can improve sideslip angle and friction coefficient estimation and evaluates robustness of estimation to road bank angle. The considered smart tyre is based on three tri-axial accelerometers glued on the inner liner. The adopted sensor presents the advantages of tiny dimensions, low weight, minimal impact on the production process, wide bandwidth, high reliability and the robustness required to withstand the impulses occurring when the sensors enter and exit the footprint. Available measurements, which are provided once per wheel turn by the smart tyre, are the longitudinal, lateral and vertical contact forces.

To evaluate the effect of these additional measurements on sideslip angle and friction coefficient estimation, an Extended Kalman Filter based on a single-track vehicle model was implemented.

Keywords Smart tyre • Sideslip angle estimation • Friction coefficient estimation • Extended Kalman Filter (EKF)

9.1 Introduction

A proper estimation of sideslip angle is fundamental for vehicle stability control. Stability control systems in fact prevent vehicles from spinning and drifting out by controlling the yaw rate and the sideslip angle. High values of sideslip angle could reduce the ability of the tyres to generate lateral forces and consequently the vehicle's performances [1, 2]. Hence, in addition to the yaw rate control, the sideslip angle control is fundamental in order to ensure an effective control of the vehicle. The yaw rate is measured directly on board meanwhile the sideslip angle can only be measured by very expensive devices, which result unsuitable for ordinary vehicles implementation so that it must be estimated. In literature, several estimators based on state observer/Kalman filter that use the measures of yaw rate and steering angle, have been proposed for the sideslip angle estimation [3–6]. Obtained results are satisfying if high friction surfaces are considered but they get worse when the tyre-road friction coefficient decreases. To address this issue several methodologies are proposed in the literature: observers with parameters update [7–10], estimators based on neural networks [11–13], GPS systems [14], etc. However sideslip angle and friction coefficient estimation is still an open issue.

Aim of the present paper is to investigate how smart tyres can improve sideslip angle and friction coefficient estimation and to evaluate robustness of estimation to road bank angle. Smart tyres are an emerging technology aimed at turning the tyre into a sensor able to provide information about tyre-road contact. Among the different types present in the technical literature, a smart tyre constituted of two three-axial MEMS accelerometers directly glued on the inner liner is considered in this study. Available measurements, which are provided once per wheel turn by the adopted smart tyre, are assumed to be longitudinal, lateral and vertical contact forces.

To evaluate the effect of these additional measurements on sideslip angle and friction coefficient estimation, an Extended Kalman Filter (EKF) based on a single-track vehicle model was implemented. A five degree-of-freedom (5 dofs) model accounting for the lateral, yaw, pitch, and roll motions of the vehicle was used to assess the capability of the proposed observer to estimate the vehicle sideslip angle and the friction coefficient. Specifically, several handling maneuvers on variable adherence surface were simulated. Robustness of the observer to road bank angle and tyre parameters variation is also discussed.

F. Cheli • D. Ivone • E. Sabbioni (✉)
Department of Mechanical Engineering, Politecnico di Milano, Via La Masa 1, 20156 Milan, Italy
e-mail: edoardo.sabbioni@polimi.it

E.W. Sit (ed.), *Sensors and Instrumentation, Volume 5*, Conference Proceedings of the Society for Experimental Mechanics Series, DOI 10.1007/978-3-319-15212-7_9

9.2 Smart Tyre

In recent years, different types of smart tyres were presented in technical literature [15–24]. Aim of these devices is to turn the tyre into a sensor, able to provide direct information about the contact dynamics. Different technologies were proposed: optical device fixed on the rim measuring the displacement of a LED installed on the inner liner [16], sensors embedded inside the tread based on surface acoustic wave [17] or on Hall effect [18]. Other authors used the tyre structure itself as a sensing devices by measuring the variation of impedance between the steel wires associated with the change of spacing between them produced by contact forces [19]. Several smart tyres presented in literature are built by fixing a measuring device directly on the inner surface of the tyre; polyvinylidene sensors in [21] and accelerometers in [15]. These approaches are all characterized by a simple installation of the sensor and by the direct measurement of the deformation of the tyre structure. A scheme similar to the one proposed in [22–24] is considered in this study. It is based on 2 three-axial MEMS accelerometers (9.1a) directly glued on the inner liner. The measured directions are the radial (r), lateral (l) and the tangential (t) (see Fig. 9.1b). The adopted sensors present the advantages of tiny dimensions, low weight, minimal impact on the production process, wide bandwidth, high reliability and the robustness required to withstand the impulses occurring when the sensors enter and exit the footprint. Data recorded and processed by smart tyres are sent on board through an RF transmission. The smart tyre considered in this work is able to provide data relevant to the contact conditions only once per revolution [15]. Through post-elaboration of the acquired acceleration signals it is possible to determine, among others:

- the dimensions and shape of the footprint area;
- the vertical, longitudinal and lateral tyre-road contact forces;
- the angular speed.

While some of these quantities are directly determined from the shape of the accelerations (such as the dimensions of the footprint area), some others require sophisticated algorithms developed through preliminary indoor calibration tests. For instance, Fig. 9.2 shows the capability of the considered smart tyre of estimating the normal and longitudinal contact

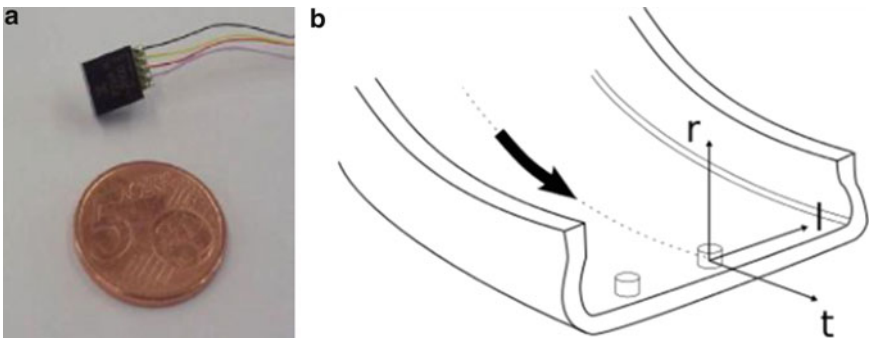

Fig. 9.1 (**a**) Reference system; (**b**) Orientation

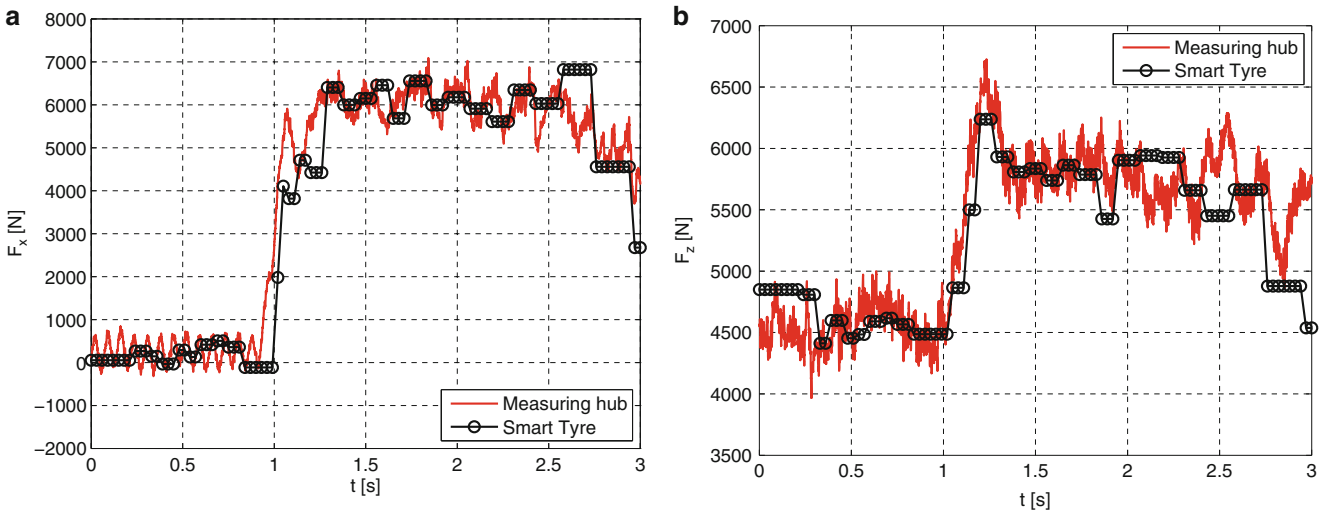

Fig. 9.2 Comparison between forces measured by a commercial dynamometric hub and the smart tyre during a ABS braking maneuver: (**a**) vertical force, (**b**) longitudinal force

forces during an ABS braking manoeuvre performed on straight track; the comparison between the forces measured with a dynamometric hub and the corresponding values produced by the smart tyre, clearly points out the ability of the sensor to provide reliable estimations of contact forces; since the estimation is provided once per wheel revolution a small time shift is revealed.

Due to industrial privacy reasons, it is not allowed to publish further information and data analysis with respect to the already mentioned articles in the bibliography.

9.3 Vehicle Model

To design the state observer and check its performance, a five degree-of-freedom (5-DOF) model accounting for the lateral (y), yaw (ψ), pitch (θ), and roll (ρ) motions of the vehicle is considered. This is the simplest platform allowing a good state reproduction during cornering while also providing physically realistic load transfers. Making reference to Fig. 9.3, the equations of motion of the model are:

$$\begin{cases} mA_x = -\left(Fy_{fl} + Fy_{fr}\right) sin\delta \\ m\left(A_y + gsin\Phi\right) = \left(Fy_{fl} + Fy_{fr}\right) cos\delta + \left(Fy_{rl} + Fy_{rr}\right) \\ J_z\ddot{\psi} = \left(Fy_{fl} + Fy_{fr}\right) cos\delta\ a - \left(Fy_{rl} + Fy_{rr}\right)\ b \\ m\left(A_y + gsin\Phi\right) h_g = J_x\ddot{\rho} + C_\rho\dot{\rho} + \left(K_\rho - mgh_g\right)\rho \\ mA_x\left(h_g - h_b\right) = J_y\ddot{\vartheta} + C_\vartheta\dot{\vartheta} + K_\vartheta\vartheta \end{cases} \tag{9.1}$$

where Φ is the road bank angle.

Since in the following only coasting manoeuvres are considered, no traction or braking forces are applied and so no longitudinal forces appear into the equations of motion. However, to consider the most general case pitch and longitudinal dynamic equilibrium equations are considered into the model. The vertical load acting on each tyre can be calculated according to:

$$\begin{cases} Fz_{fl,r} = Fz0_{fl,r} - \frac{\left(C_{\vartheta f}\dot{\vartheta} + K_{\vartheta f}\vartheta\right)}{2a} \pm \frac{\left(C_{\rho f}\dot{\rho} + K_{\rho f}\rho\right)}{c_f} \\ Fz_{rl,r} = Fz0_{rl,r} - \frac{\left(C_{\vartheta r}\dot{\vartheta} + K_{\vartheta r}\vartheta\right)}{2b} \pm \frac{\left(C_{\rho r}\dot{\rho} + K_{\rho r}\rho\right)}{c_r} \end{cases} \tag{9.2}$$

where $Fz0_i = Fz0_i\left(\Phi\right)$ is the static vertical load applied on each tyre according to the position of the center of gravity of the vehicle and the bank angle of the road.

The slip angle of the *j-th* tyre of the *i-th* axle is calculated as:

$$\alpha_{ij} = \arctan^{-1}\left(\frac{V_{yij}}{V_{xij}}\right) \tag{9.3}$$

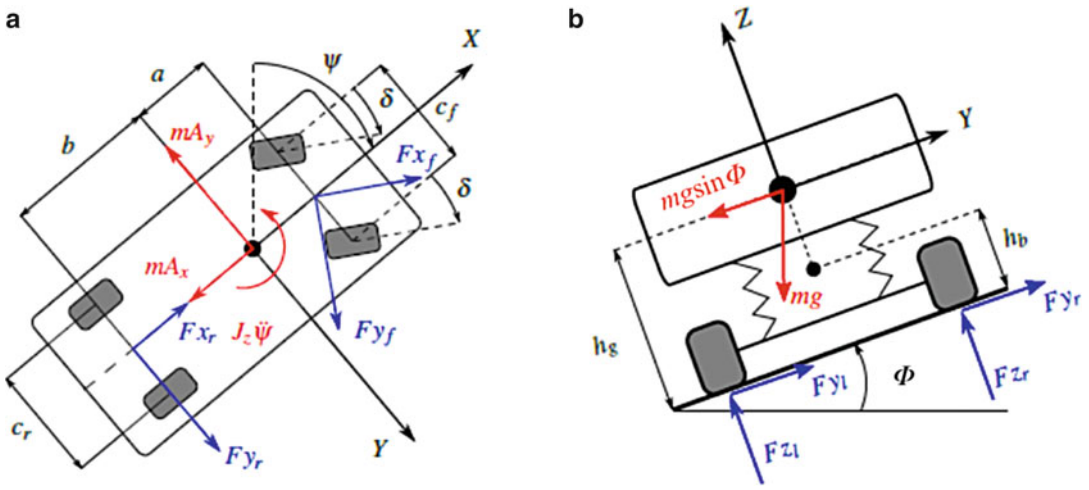

Fig. 9.3 5 dofs vehicle model

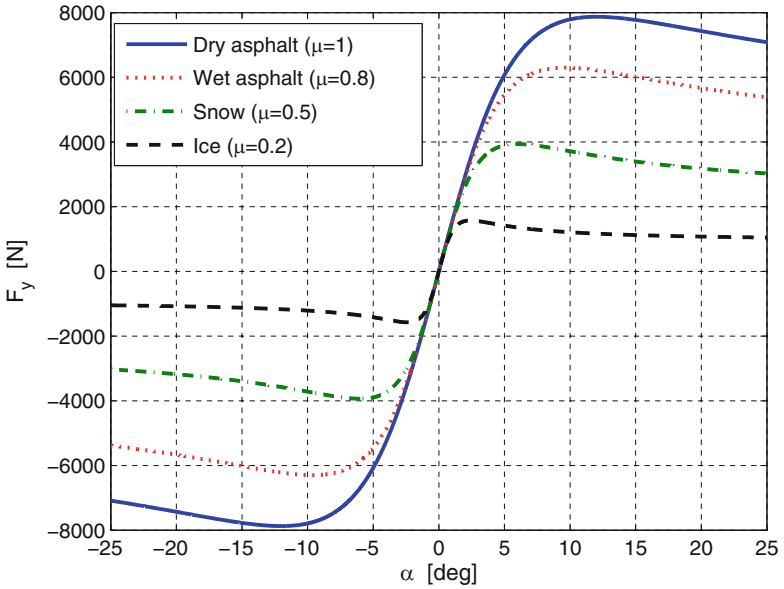

Fig. 9.4 Force versus tyre slip angle curve for different adherence conditions

being V_{xij} and V_{yij} the longitudinal and lateral velocities of the tyre. The sideslip angle is defined as:

$$tan\beta = \frac{V_y}{V_x} \tag{9.4}$$

being V_x and V_y the projections of the vehicle speed along the axes of the reference system moving with the vehicle.

9.3.1 Tyre Model

The cornering force of the i-th tyre is calculated according to the MF-Tyre model [25] for pure lateral conditions:

$$\overline{F}_{yi} = D_i sin\left(C_i arctan\left(B_i\alpha_i - E_i\left(B_i\alpha_i - arctan\left(B_i\alpha_i\right)\right)\right)\right) \tag{9.5}$$

where α_i is the tyre slip angle.

Scaling factors λ_i are introduced to account for different friction conditions [25–27]. Figure 9.4 shows the tyre characteristic curve for different adherence conditions. As it can be seen, cornering stiffness, K, does not change as adherence varies (see Eqs. 9.6, 9.7, 9.8, 9.9, and 9.10, [25]).

$$D = \mu F_z;\ \mu = \lambda_\mu\left(p_{Dy1} + p_{Dy2}F_z\right) \tag{9.6}$$

$$C = \lambda_{Cy}P_{Cy} \tag{9.7}$$

$$K = p_{Ky1}sin\left[2atan\left(F_z/p_{Ky2}\right)\right] \tag{9.8}$$

$$B = \frac{K}{CD} \tag{9.9}$$

$$E = \lambda_{Ey}P_{Ey} \tag{9.10}$$

The transient response of a tyre to a sudden change of the slip angle is taken into account by introducing the relaxation length L_y into the tyre model. A first order time lag is thus introduced, depending on the vehicle speed V:

$$\frac{L_y}{V}\dot{F}_y + F_y = \overline{F_y} \tag{9.11}$$

9.3.2 Smart Tyre Sensor Emulator

In order to embed a real-like measure into the vehicle model and then investigate the response/robustness of the state observer when the measurements are affected by an error, a sensor emulator was modelled. The goal of the emulator is to reproduce some typical built-in characteristics of a smart tyre sensor as follows:

- measurement frequency: the information provided by the sensor are updated with a variable frequency depending on the wheel speed and not continuously during the rotation of the wheel. The measure is in fact assumed to be available only one time for every complete revolution of the wheel. The information is kept constant until the new wheel turn is completed.
- time delay τ: the signal measured at time t is available at the control unit only after a time gap τ, due to the transmission and the processing of the measured data. During the simulations the time delay τ has been assumed to be equal to one turn.
- resolution: quantized measure due to the digital sensor architecture.
- systematic error: expressible as mean value of Gaussian distribution which represents the error affecting the measure. The mean value is assumed equal to 0, since it may affect a possible offset in the measured value with respect to the actual one, but it can be supposed to be filtered after a sensor calibration.

The value of the time delay τ and of the parameters of the Gaussian distribution meant to simulate the measuring error propagation were gained from an experimental campaign of data acquisition with a prototype of the considered smart tyre.

9.4 Extended Kalman Filter

To estimate the sideslip angle β, the friction coefficient μ and the road bank angle Φ, an Extended Kalman Filter (EKF) was implemented. The backbone of the filter is a single-track vehicle model whose equations of motion are (see Fig. 9.5):

$$\begin{cases} m\left(A_y + gsin\Phi\right) = m\left(\dot{\psi}V + V\dot{\beta} + V\beta + \dot{g}sin\Phi\right) = F_{yf} + F_{yr} \\ J_z\ddot{\psi} = F_{yf}a - F_{yr}b \end{cases} \tag{9.12}$$

m is the vehicle mass, J_z the yaw moment of inertia, a and b the distance of the cog from the front and the rear axle respectively, $\dot{\psi}$ is the yaw rate, A_y is the lateral acceleration and V the speed. Axles' contact forces are introduced through the MF-Tyre model:

$$\overline{F}_{yi} = D_i sin\left(C_i arctan\left(B_i\alpha_i - E_i\left(B_i\alpha_i - arctan\left(B_i\alpha_i\right)\right)\right)\right) \tag{9.13}$$

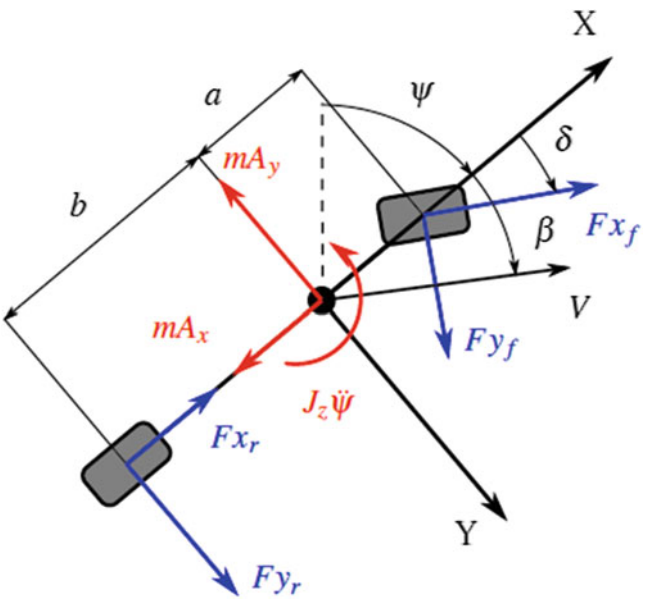

Fig. 9.5 Single-track vehicle model

where α_i is the slip angle of the i-th axle. It must be pointed out that parameters C_i and E_i are constant while coefficients B_i and D_i are defined as:

$$D_i = \lambda_\mu D_{i0} \tag{9.14}$$

$$B_i = B_{i0}/\lambda_\mu \tag{9.15}$$

The nonlinear Eq. 9.12 can be rewritten as:

$$\begin{cases} \dot{\underline{x}}(t) = f\left(\underline{x}(t),\ \underline{u}(t), \lambda_\mu(t), \Phi(t)\right) + \underline{w}(t) \\ \underline{y}(t) = h\left(\underline{x}(t),\ \underline{u}(t), \lambda_\mu(t), \Phi(t)\right) + \underline{v}(t) \end{cases} \tag{9.16}$$

where $\underline{w}$ and $\underline{v}$ are the process and the measurement noise, $\underline{x} = \left[\beta\ \dot{\psi}\right]^T$ is the vehicle model state vector, $\underline{u} = [V\ \delta]^T$ the input vector containing the steer angle and the vehicle speed (which are supposed to be measured) and finally $\underline{y}$ is the measurement vector which will be defined later on. Assuming that the unknown friction coefficient and road bank angle can be modelled as integrated white noise, Eq. 9.16 can be rewritten as:

$$\begin{cases} \dot{\underline{z}}(t) = \begin{Bmatrix} \dot{\underline{x}}(t) \\ \dot{\underline{\vartheta}}(t) \end{Bmatrix} = \begin{bmatrix} f\left(\underline{x}(t),\ \underline{u}(t), \underline{\vartheta}(t)\right) \\ \underline{0} \end{bmatrix} + \begin{bmatrix} \underline{w}(t) \\ \underline{w}_\vartheta(t) \end{bmatrix} \\ \underline{y}(t) = h\left(\underline{x}(t),\ \underline{u}(t), \underline{\vartheta}(t)\right) + \underline{v}(t) \end{cases} \tag{9.17}$$

where $\underline{z}$ is the extended state vector, containing the model parameters to be estimated, which are collected in vector $\underline{\vartheta} = \left[\lambda_\mu\ \Phi\right]^T$. Since the EKF can be regarded as a state observer and the friction coefficient and the road bank angle have been introduced as states, they can be estimated if the vehicle response is measured. A minimum mean-square error of the augmented estimated state vector $\widehat{\underline{z}}$ is in fact provided by the EKF minimizing the difference between the vehicle response $\underline{y}$ and the model response $\widehat{\underline{y}}$:

$$\begin{cases} \dot{\widehat{\underline{x}}} = f\left(\widehat{\underline{x}},\ \underline{u}, \widehat{\underline{\vartheta}}\right) + [K_x]\left(\underline{y} - \widehat{\underline{y}}\right) \\ \widehat{\underline{\vartheta}} = [K_\vartheta]\left(\underline{y} - \widehat{\underline{y}}\right) \\ \widehat{\underline{y}} = h\left(\widehat{\underline{x}},\ \underline{u},\ \widehat{\underline{\vartheta}}\right) \end{cases} \tag{9.18}$$

The filter gain matrices $[K_x]$ and $[K_\vartheta]$ are obtained by solving a suitable Riccati equation which can be obtained linearizing the equation of motion around the last available state estimation. The main assumption is to consider the same friction coefficient for all the wheels. Regarding the measurement vector y, two cases are taken into account and compared. In both cases y contains the measures of lateral acceleration, yaw rate and front and rear axles' cornering forces. However, while in one case cornering forces are measured once per wheel turn by the smart tyres (Case 1), in the other they are estimated based on the lateral acceleration measurement A_{ym} (Case 2). It must be noticed that A_{ym} includes the projection of the gravitational acceleration due to the road bank angle.

$$A_{ym} = A_y + g sin\Phi \tag{9.19}$$

Case 2 represents a state-of-the-art observer for sideslip angle estimation, which does not have available contact force measurements. It thus constitutes a reliable term of comparison to evaluate the benefits induced by the additional information provided by smart tyre on sideslip angle estimation purposes.

9.4.1 Case 1: Contact Forces Measured by Smart Tyres

In this case, (F_{yi}) are directly measured by the smart tyre. It must be pointed out that measurements are provided once per wheel turn. Sample-and-hold is algorithm used in between two wheel turns:

$$\underline{y}_1 = \left[A_{ym}\ \dot{\psi}\ F_{yf}\ F_{yr}\right]^T \tag{9.20}$$

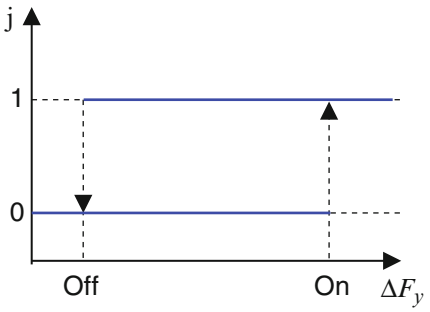

Fig. 9.6 Relay with hysteresis to select proper measurement noise variance

9.4.2 Case 2: Contact Forces Estimated Through Lateral Acceleration Measurement

In this case, front and rear axles' cornering forces ($\tilde{F}_{\mathrm{yi}}$) are not directly measured, but they are calculated based on lateral acceleration measurement considering the steady-state equation of the single-track vehicle model:

$$\underline{y}_2 = \left[A_{ym}\ \dot{\psi}\ \tilde{F}_{yf}\ \tilde{F}_{yr}\right]^T \tag{9.21}$$

where:

$$\begin{cases} \tilde{F}_{yf} = mA_y \dfrac{b}{(a+b)} \\ \tilde{F}_{yr} = mA_y \dfrac{a}{(a+b)} \end{cases} \tag{9.22}$$

9.4.3 Covariance Matrix: Nonlinearity Evaluation

To speed up augmented state vector estimation, the measurement noise covariance matrix $[R_n]$ should continuously be modified, especially when vehicle behaviour is nonlinear. Evaluation of nonlinearity of the system is achieved through measures/estimates of cornering forces. When the vehicle exhibits a nonlinear behaviour, noise associated with axles' contact forces is reduced to amplify the correspondent gains in matrix $[K_\vartheta]$. Estimation of vector $\widehat{\underline{z}}$ is consequently speed up during hard cornering.

On this purpose, the hysteresis loop shown in Fig. 9.6 was implemented to modify the diagonal elements of matrix $[R_n]$ associated with axles' cornering forces and lateral acceleration. As long as the difference between the contact forces included into the measurement vector (F_{ym}) and the contact forces calculated by the reference model of the EKF ($\widehat{F}_{yi}$)

$$\Delta F_{yi} = \left|\widehat{F}_{yi} - F_{ym}\right| \tag{9.23}$$

remains lower than the ON threshold, elements of matrix $[R_n]$ are kept constant. Otherwise they are linearly increased until the value ΔF_{yi} drops under the OFF threshold.

9.5 Results

Performance of the observers has been verified through several handling manoeuvres simulated with the previously described 5 DOF vehicle model.

As an example, Fig. 9.7 shows the results of the observers during a step-steer manoeuvre carried out at 100 km/h on a low-adherence surface ($\mu = 0.4$). To reproduce vehicle behaviour on a low-adherence surface, scaling factors have been used in the MF-Tyre model (see Eqs. 9.6, 9.7, 9.8, 9.9, and 9.10 and Fig. 9.4).

Sideslip angle, yaw rate and lateral acceleration of the model are compared with the estimated ones in Fig. 9.7a. Friction coefficient and road bank angle are instead shown in Fig. 9.7b. As it can be seen both the observers provide satisfactory

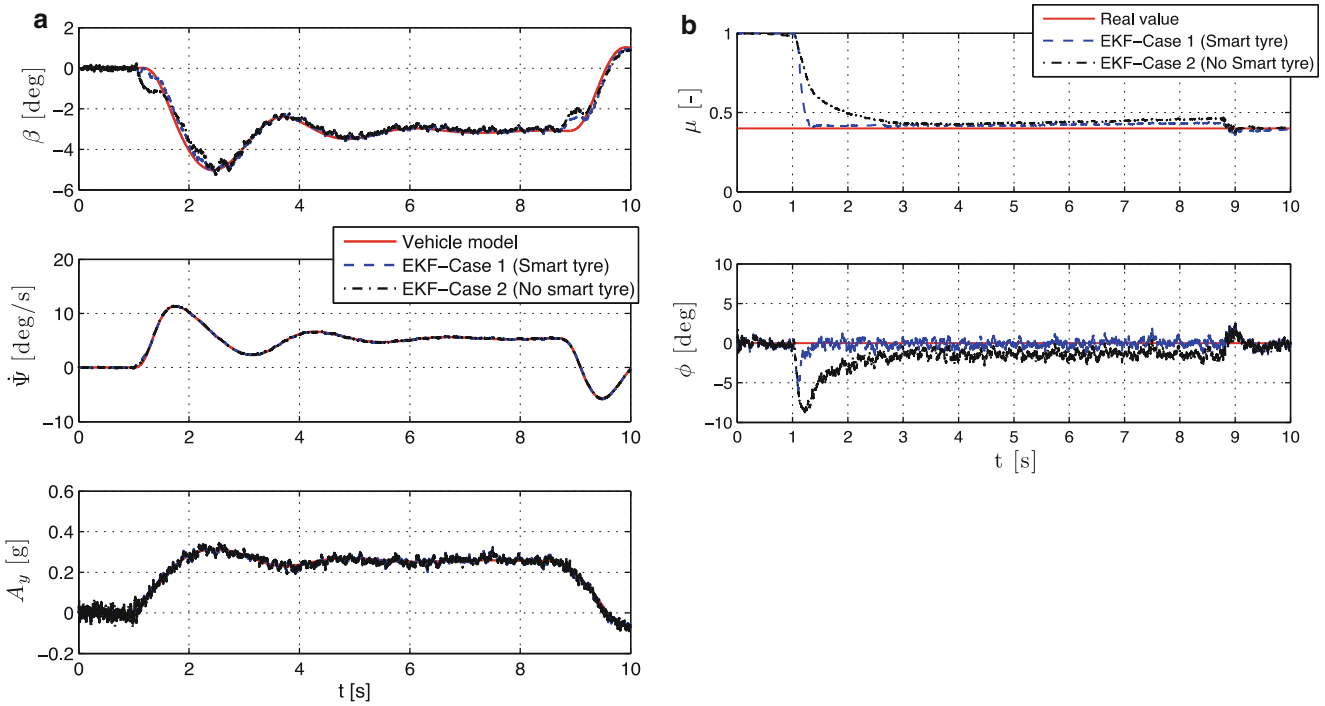

Fig. 9.7 Step steer, V = 100 Km/h – μ = 0.4 – Φ = 0. Time histories of sideslip angle, yaw rate lateral acceleration (**a**), friction coefficient and road bank angle (**b**)

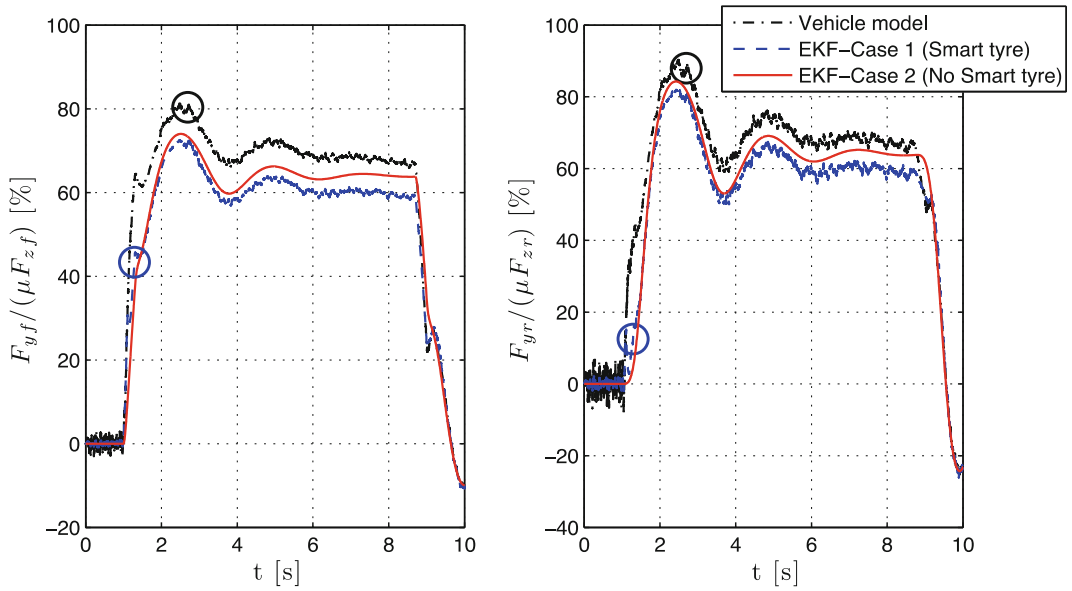

Fig. 9.8 Percentage of front and rear forces when an error of 5 % on μ estimation is reached

results. However the observer including the measurement of cornering forces provided by smart tyres (blue dashed line) allows a faster estimation of friction coefficient. This leads to a more accurate estimation of vehicle response and road bank angle during the transient part of the manoeuvre.

Figure 9.8 shows when the friction coefficient is identified with an error lower than 5 %. Time histories of cornering forces of front and rear axles normalized by their possible maximum value are depicted on the purpose. As it can be seen, the 40 % of the maximum value of F_{yf} must be reached before friction coefficient is correctly estimated by the EKF when smart tyres' measurements are available (Case 1). If these measurements are not available (Case 2), the peak value (i.e. the

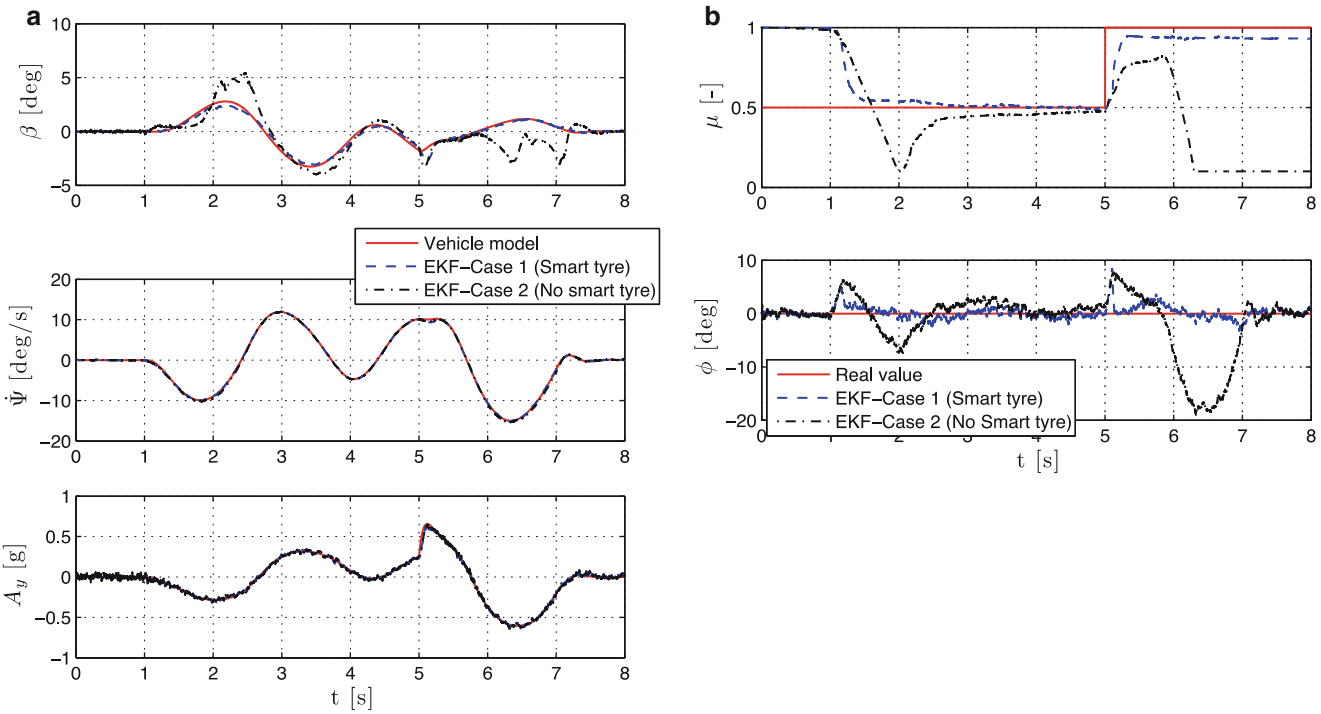

Fig. 9.9 Double-lane change, V = 90 Km/h – μ_jump – Φ = 0. Time histories of sideslip angle, yaw rate lateral acceleration (**a**), friction coefficient and road bank angle (**b**)

80 % of the maximum possible value) of front and rear cornering force must be reached for a successful friction coefficient estimation. This result is coherent with the findings of [5] concerning the longitudinal dynamics of the vehicle. It must be noted that, obviously, estimation of λ_μ begins only after the vehicle has started the manoeuvre.

In Fig. 9.9 a double-lane change at 90 km/h on a variable adherence surface is instead presented. Specifically the friction coefficient jumps (μ-jump) from 0.5 to 1 after 5 s. The same quantities of Fig. 9.7 are shown. Significant differences can be noticed between Case 1 and Case 2. The direct measure of the contact forces allows the EKF to correctly estimate vehicle states and unknown parameters. On the contrary Case 2 is not able to accurately estimate the friction coefficient and road bank angle, this leading to significant errors in sideslip angle estimation.

Similar results have been obtained in all the other performed handling manoeuvres carried out at speeds higher than 30 km/h. Under this speed, quality of sideslip angle estimation of Case 1 significantly gets worse due to once per wheel turn measures of tyre-road contact forces provided by smart tyres.

Finally, robustness of implemented observer to road bank angle changes was investigated. As an example, Fig. 9.10 shows a step-steer manoeuvre on a low-friction surface ($\mu = 0.4$) during which road bank angle is varied in the range $\pm 5°$. As it can be noticed, Case 2 is not capable of evaluating the portion of lateral acceleration due to road bank angle and consequently estimation of vehicle sideslip angle and friction coefficient is not satisfactory. In Case 1, the direct measure of contact forces allows the state observer to correctly estimate road bank angle and consequently the friction coefficient.

9.6 Concluding Remarks

An EKF to estimate vehicle sideslip angle and tyre-road friction coefficient is presented in this paper. To assess the benefits induced by a smart tyre able to measure tyre-road contact forces once per wheel turn, the EKF is alternatively fed with an estimate of the cornering forces based on the lateral acceleration or with the measures provided by a smart tyre. If friction

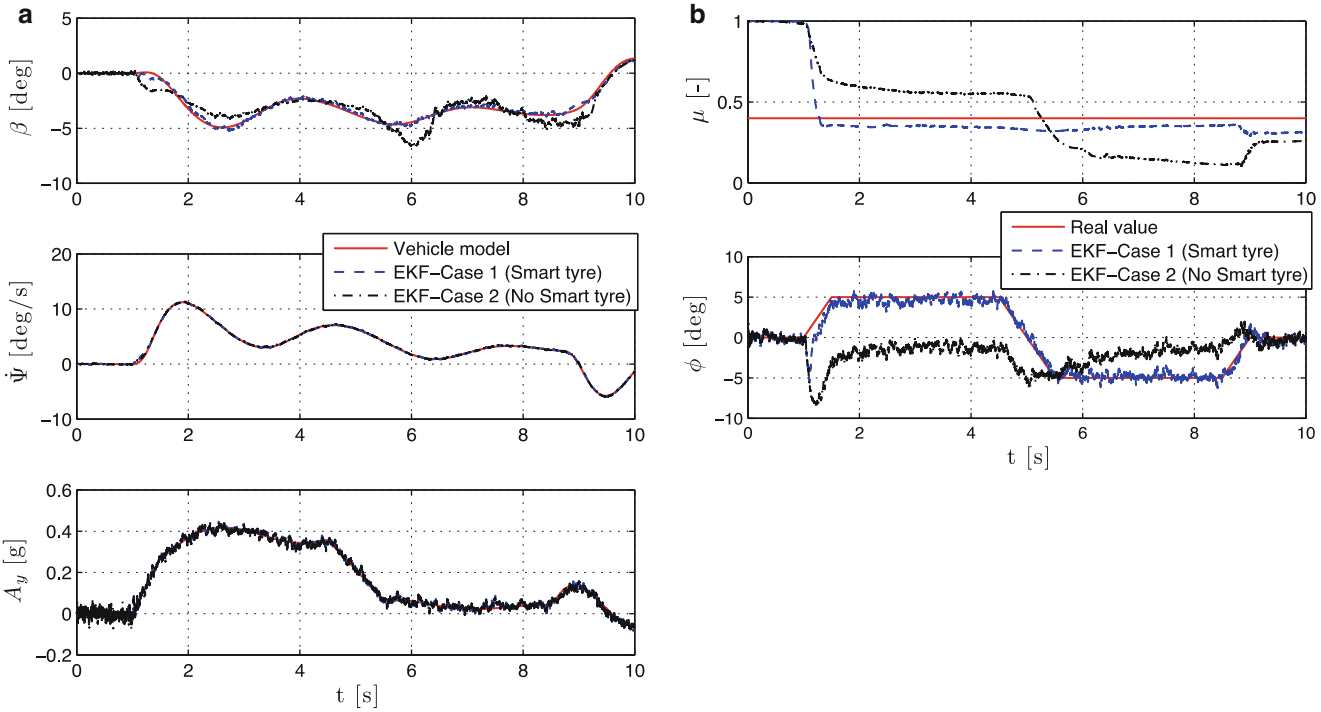

Fig. 9.10 Step steer, V = 100 Km/h – μ = 0.4 – varying bank angle. Time step steer, V = 100 Km/h – μ = 0.4 – Φ = 0 of sideslip angle, yaw rate lateral acceleration (**a**), friction coefficient and road bank angle (**b**)

coefficient is constant during the manoeuvre no significant differences can be noticed in the estimation, even if the correct value of μ is reached before when cornering force measurement is available. On the contrary, significant improvements can be noticed when a μ-*jump* is present during the manoeuvre. The measurement of the cornering forces makes the implemented EKF robust to road bank angle, tyres' parameters variation and vehicle's parameters variation.

Acknowledgments Authors greatly acknowledge Pirelli Tyres for the support in this research.

References

1. van Zanten AT, Pfaff G (1996) Control aspects of Bosch-VDC. In: Proceedings of AVEC international symposium on advanced vehicle control, Aachen
2. van Zanten AT (2000) Bosch ESP systems: 5 years of experience. SAE technical paper 2000-01-1633
3. Kiencke U, Daib A (1997) Observation of lateral vehicle dynamic. Control Eng Pract 5(8):1145–1150
4. Venhovens PJ Th, Naab K (1999) Vehicle dynamics estimation using Kalman filters. Veh Syst Dyn 32(2–3):171–184
5. Muller S, Uchanski M, Hedrick K (2004) Estimation of the maximum tire-road friction coefficient. J Dyn Syst Meas Control 125(4):607–617
6. Yi K, Hedrick K, Lee SC (1999) Estimation of tire-road friction using observer based identifiers. Veh Syst Dyn 31(4):233–261
7. Gaoa X, Yua Z, Neubeckb J, Wiedemannb J (2010) Sideslip angle estimation based on input-output linearization with tire-road friction adaptation. Veh Syst Dyn 48(2):217–234
8. Cheng Q, Correa-Victorino A, Charara A (2008) A new nonlinear observer using unscented Kalman filter to estimate sideslip angle, lateral tire road forces and tire road friction coefficient. In: IEEE intelligent vehicles symposium, Baden, 5–9 June, pp 709–714
9. Aleksander H, Simpson MD (2000) Estimation of vehicle sideslip angle and yaw rate. Tech. rep. SAE technical paper 2000-01-0696
10. Cheli F, Melzi S, Pesce M, Sabbioni E (2007) A methodology for vehicle sideslip angle identification: comparison with experimental data. Veh Syst Dyn 45(6):549–563
11. Melzi S, Sabbioni E (2011) On the vehicle sideslip angle estimation through neural networks: numerical and experimental results. Mech Syst Signal Process 25(6):2005–2019
12. Sasaki H, Nishimaki T (2000) A sideslip angle estimation using neural network for a wheeled vehicle. Tech. rep. SAE technical paper 2000-01-0695
13. Abdulrahim M (2006) On the dynamics of automobile drifting. Tech. rep. SAE technical paper 2006-01-1019
14. Ryu J, Gerdes JC (2004) Integrating inertial sensors with global positioning system (GPS) for vehicle dynamics control. J Dyn Syst Meas Control 126(2):243–254

15. Mancosu F, Brusarosco M, Cheli F, Melzi S (2008) Method for determining at least one parameter representative of at least one interaction along a longitudinal direction between a tyre for vehicle and the ground. Patent no. PCT WO 2008/65465
16. Tuononen AJ (2008) Optical position detection to measure tyre carcass deflections. Veh Syst Dyn 46(6):471–481
17. Pohl A et al (1999) The "intelligent tire" utilizing passive saw sensors – measurement of tyre friction. IEEE Trans Instrum Meas 48(6):1041–1046
18. Yilmazoglu O, Brandt M, Sigmund J, Genc E, Hartnagel HL (2001) Integrated InAs/GaSb 3D magnetic field sensors for "the intelligent tire". Sensors Actuators A Phys 94(1–2):59–63
19. Sergio M, Manaresi N, Tartagni M, Canegallo R, Guerrieri R (2006) On a road tyre deformation measurement system using a capacitive-resistive sensor. Smart Mater Struct 15(6):1700–1706
20. Yi J (2008) A piezo-sensor-based 'smart tire' system for mobile robots and vehicle. IEEE/ASME Trans Mechatron 13(1):95–103
21. Matsuzaki R, Todoroki A (2007) Wireless flexible capacitive sensor based on ultra-flexible epoxy resin for strain measurement of automobile tires. Sensors Actuators A Phys 140(1):32–42
22. Cheli F, Leo E, Melzi S, Sabbioni E (2010) On the impact of "Smart Tyres" on existing ABS/EBD control systems. Veh Syst Dyn 48(1):255–270
23. Cheli F, Braghin F, Brusarosco M, Mancosu F, Sabbioni E (2011) Design and testing of an innovative measurement device for tyre-road contact forces. Mech Syst Signal Process 25(6):1956–1972
24. Cheli F, Sabbioni E, Sbrosi M, Brusarosco M, Melzi S, D'Alessandro V (2011) Enhancement of ABS performances through on-board estimation of the tyres response by means of smart tires. Tech. rep. SAE technical paper 2011-01-0991
25. Pacejka HB (2006) Tyre and vehicle dynamics, 2nd edn. Butterworth-Heinemann, Oxford (cit. on p. 4)
26. Braghin F, Cheli F, Sabbioni E (2006) Environmental effects on Pacejka's scaling factors. Veh Syst Dyn 44(7):547–568
27. Braghin F, Cheli F, Sabbioni E, Arosio D (2010) Identification of Pacejka's scaling factors from full-scale experimental tests. Veh Syst Dyn 43(1):457–474

Chapter 10
Rotational Accelerometers and Their Usage in Investigating Shaker Head Rotations

M. Dumont and N. Kinsley

Abstract In many applications such as structural testing or vehicle collision studies, rotational data are required. Modal analysis will mainly use it to identify rotational Degrees of Freedoms (DOFs) where crash testing will mainly look into rotational inertia. Measuring rotational acceleration can be done by computing measurements from linear sensors but this leads inevitably to an increase in measurement errors. The Kistler quartz rotational accelerometers types 8838 and 8840 have been developed for direct measurement of angular acceleration. In the first part of this paper, we are going to compare the internal design of the rotation accelerometers type 8838 and 8840 to solutions based on computing measurements from linear sensors. We will look into optimization of the assembly as well as a calibration procedure. In the second part of this paper we will focus on how the rotational sensors have been used to identify and investigate shaker planar rotation. We will then look into how these undesirable planar rotations can influence linear sensor measurement.

Keywords Rotational accelerometers • Angular acceleration • Rotational motions

10.1 Introduction

The acceleration experienced by a rotating member or structure is often a very important parameter during system design. An automobile crash imparts tremendous energy into the occupants typically in the form of significant rotational inertia. Mechanical structures deform dynamically at resonant frequencies and the resulting stresses can cause tremendous damage. The fields of study referred to as Impact Dynamics and Modal Analysis investigate the characteristics of these mechanical systems or structures. Finite Element Analysis (FEA) is typically employed to form a mathematical model of the system. This analysis relates the deformation at one surface of a discrete elemental section to the surface deformation at opposing elemental surfaces using an appropriate stress/strain relationship. Surface displacements and rotations are considered in the computer model where each of them represents a degree of freedom (DOF) of the system. Attachments such as welds, bolted joints, etc. can introduce a significant error into the FEA model because the required stiffness estimates are generated from engineering judgment and empirical data. The stiffness at these connections is dependent on many variables such as weld homogeneity, weld thickness, mounting torque, etc. A dynamic measurement or analysis must be performed when the results may have critical consequences. Correlation can be forced between the experimental and analytical study and by applying a modification or 'assumption adjustments' to the computer model. Once this correlation is obtained and the model assumptions are verified, an accurate prediction can be made with confidence regarding improvements to the existing design.

Measurement techniques have been used to estimate rotational DOFs but a sensor designed specifically for these measurements is very rare on the marketplace. Kistler quartz rotational accelerometers 8838 and 8840 employ sensing technology having the salient feature requirements to create an accurate rotational accelerometer. Also, assembly and calibration procedures have been developed to optimize the sensors for application within a specific field of study.

M. Dumont (✉)
Product Manager - T&M Acceleration, Kistler Instrument Corporation, 75 John Glenn Drive, Amherst, NY 14228-2171, USA
e-mail: marine.dumont@kistler.com

N. Kinsley
Kistler Instrument Corporation, 75 John Glenn Drive, Amherst, NY 14228-2171, USA

E.W. Sit (ed.), *Sensors and Instrumentation, Volume 5*, Conference Proceedings of the Society for Experimental Mechanics Series, DOI 10.1007/978-3-319-15212-7_10

10.2 True Rotational Accelerometer Versus Linear Accelerometers Solutions

A dynamic experimental study is typically performed on a structure using linear accelerometers attached at appropriate measurement sites. If they are in close proximity to each other, the difference between their linear outputs can provide an estimate of the rotation present in the system. This spatially narrow array provides a means to estimate rotational acceleration but it's still difficult to obtain an accurate measurement near interfaces such as bolted joints, etc.

These interfaces often have considerable relative rotation and minimal displacement. Therefore, a direct measurement of the rotation is important. Historically, measuring this dynamic rotational data has not been straightforward due to the lack of a convenient measurement device, or rotational accelerometer [1].

There has been a variety of techniques attempted which use a pair of spatially separated, sensitivity matched, accelerometers to determine rotational acceleration. When attached to a fixture, at a prescribed distance apart, the output signal difference between them is proportional to rotational acceleration (Fig. 10.1).

If the path between them is short and rigid, such that there is no local rotation between the matched accelerometers, the rotation at the base of the fixture can be computed. This approach can be used in many situations to obtain a reasonable estimate, under favorable conditions, but not in all circumstances. "There is a major problem that is encountered, which derives from the fact that the prevailing levels of output signal generated by the translational components of the structure's movement tend to overshadow those due to the rotational motions, a fact which makes the differencing operations above liable to serious errors" [1].

1. This undesirable ratio places a high precision requirement on the sensitivity matching process. The effect of sensitivity mismatch error has been analyzed and shown that an error in sensitivity matching as small as ¼ % can contribute 12.3 % error in the computed rotational acceleration even on a simple cantilever beam structure.
2. This error analysis was performed with the assumption that an infinitely rigid attachment was present between the two sensors. Also, transverse influences were excluded from the study by an appropriate selection of specimen and test conditions. It is clear that producing an accurate rotational accelerometer from commercially available hardware is a very challenging task.

Manufacturers of accelerometers have better control over the sensitivity matching process and can incorporate technologies which have the qualities required by the design constraints of an accurate rotational accelerometer. The design of an accelerometer always involves the optimization of a 'parameter compromise'. There is not a single accelerometer that fulfills all realms of acceleration measurement. Application specific designs are tailored for their best fit into the field of interest. As an example, Experimental Modal Analysis (EMA) is a field of study which predominately incorporates a sensor well suited for the following conditions/characteristics: low frequency range of <1,000 Hz; moderate and controlled environmental conditions; excellent immunity to transverse inputs; lightweight package; and high output sensitivity with low noise.

The next part will allow us to look into such a design by investigating piezoelectric quartz based Kistler 8838 and 8840 Rotational Acceleration sensors.

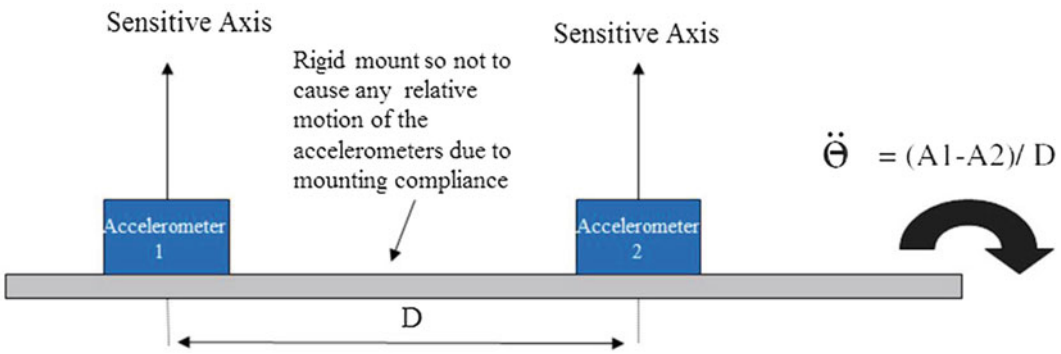

Fig. 10.1 Rotational acceleration measurement using 2 linear accelerometers

10.3 Piezoelectric Quartz Based Rotational Accelerometer 8838 and 8840 Designs

Quartz is an extremely rigid material having natural piezoelectric characteristics based on fundamental properties of its molecular structure. These characteristics are absolutely stable. They do not change. Quartz can be cut into various configurations where the characteristics, or piezoelectric coefficients, are dependent on the resulting orientation of the crystalline lattice with respect to the physical geometry. A common orientation, referred to as the shear cut, integrates well into an accelerometer design which is optimized for low transverse sensitivity and negligible base strain effects. This shear mode material then makes for an ideal sensing element for a rotational accelerometer. It becomes possible to create a convenient package rigidly supporting two spatially separated quartz element assemblies. An example construction is shown in Fig. 10.2.

We then need to accommodate the required rugged post processing signal conditioning. The solution lies in the fundamental design of the transducer itself. Also, a dramatic simplification to the overall sensitivity matching can be realized by appropriate management of the primary charges generated within each half of the seismic system.

Refer to Fig. 10.2 below and consider the piezoelectric plates on the right side of the symmetric package to be inverted with respect to the opposite side. Also, the total mass on each side is adjusted to be exactly equal therefore the output is equal and opposite when a linear acceleration is applied to the base. During a rotation, the acceleration experienced by each half will be different and a resulting voltage will exist at the input to the impedance converter. This voltage will be proportional to the rotational acceleration by a constant related to both the element separation and the total capacitance of the input network. The electrical arrangement of this system is very simple and the controlling factor regarding charge generation, mass, is easily measured with extreme accuracy. This is a simple, static, weighing measurement.

The sensitivity of the device is dependent on the total mass and input capacitance of the seismic system. Its measurement will be detailed in the next section. 180° rotation of the unit yields a signal with same amplitude but inverted phase as compared to the reference.

Within the sensor are signal processing electronics that convert the charge generated by the mechanical system into a high voltage signal level at a low impedance output. These accelerometers do not use standard voltage mode piezoelectric sensor couplers (IEPE Types), but are powered by any commercially available (20–30 VDC) power supply. A picture of this optimized assembly is shown in Fig. 10.3.

The internal orientation of the quartz elements enables type 8838 accelerometer to respond to oscillations occurring about the unit's mounting axis when installed in a non-rotating test application. The element structure of type 8840 accelerometer is such that the unit will accurately measure the acceleration magnitude of oscillations laterally induced to its mounting base.

For more than 10 years, Kistler has been able to manufacture in its factory in Switzerland its own synthetic crystal called PiezoStar®. This crystal allows for higher sensitivity and improved temperature coefficient of sensitivity. In a continuous product improvement effort, Kistler has decided to incorporate this crystal into the next generation of rotational accelerometer, which will show a very stable sensitivity response to temperature (Fig. 10.4), an increased sensitivity as well as an extended frequency response (Fig. 10.5).

Such a unique sensor design requires a very specific calibration method that has been patented by Kistler. This method is described in the following section.

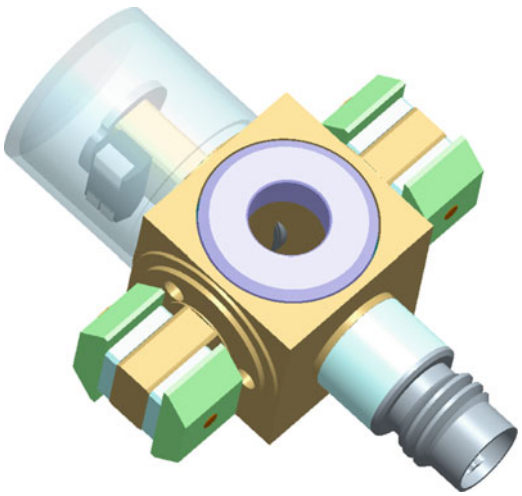

Fig. 10.2 Internal view of quartz rotational accelerometer

Fig. 10.3 Rotational accelerometer with self contained electronics

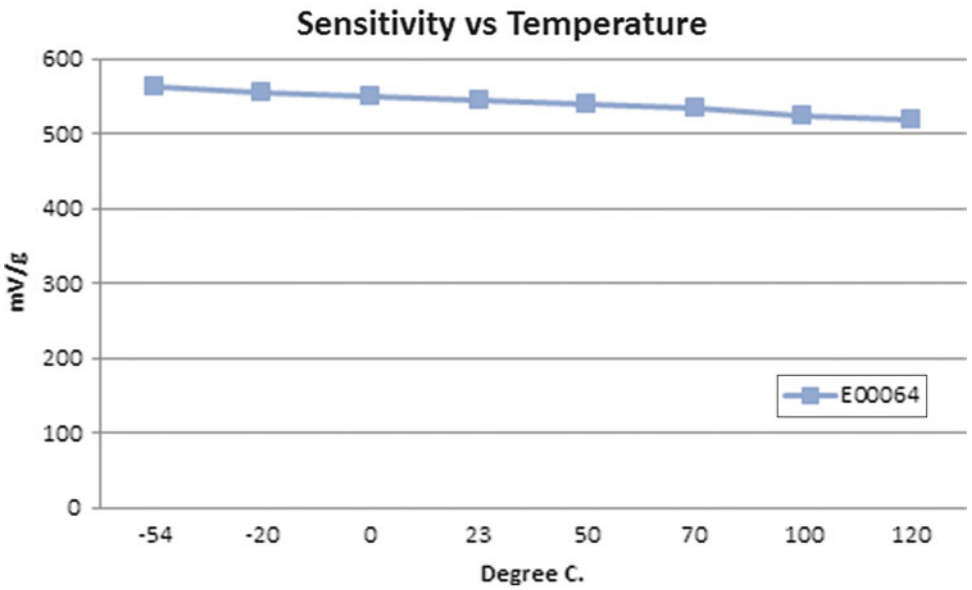

Fig. 10.4 E00064 prototype sensitivity deviation versus temperature

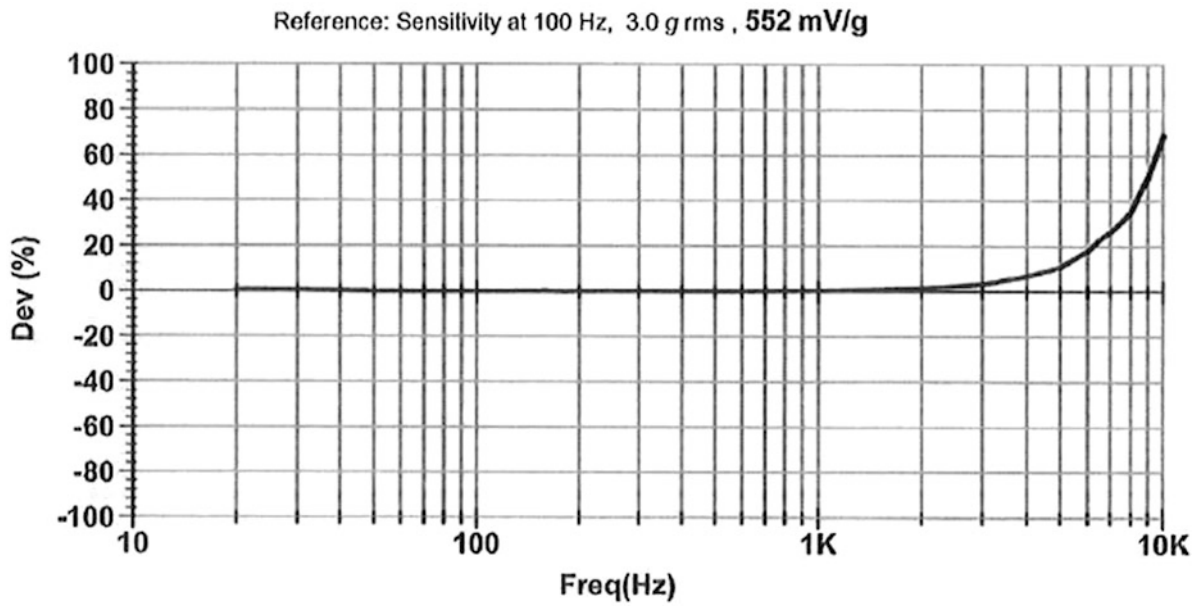

Fig. 10.5 Prototype frequency response plot generated by using an exact copy of the 8838B, with the PiezoStar® plates orientated differently in order to produce linear output

10.4 Calibration

A typical accelerometer calibration is performed with the test accelerometer connected directly to a back-to-back reference accelerometer and excited by a calibration shaker at the common reference frequency of 100 Hz. For calibration of a rotational accelerometer, input motion from a linear shaker system drives a lever arm about a central fulcrum. Figure 10.6 presents a rotational test fixture driven by a shaker through a flexible attachment rod or stinger.

The oscillating bar is rigid, within the measurement frequency range, and a reference accelerometer is used to determine the input acceleration. The fixture is driven at 12.5 Hz so that a significant input level is presented to the unit without distortion. A measurement of the rotational sensitivity is performed with the test unit mounted as shown in Fig. 10.6.

Because their measurement axes are different, the 8838 (Axial) and 8840 (Lateral) must be mounted differently (Figs. 10.7 and 10.8).

Now that we understand better the working concept of a rotational accelerometer and its calibration and resulting high accuracy, we will show in the next section how such an accurate instrument can be used for investigation of Shaker head rotations linked directly to shaker quality.

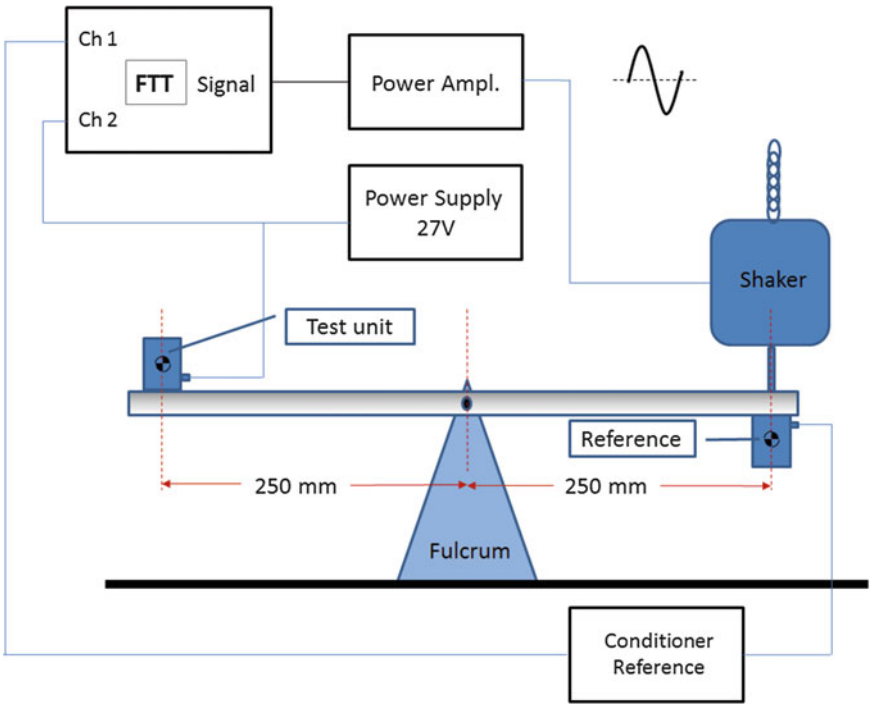

Fig. 10.6 Rotary oscillating fixture

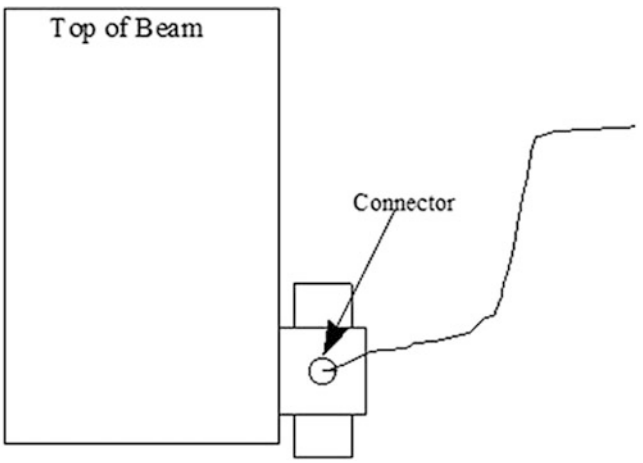

Fig. 10.7 8838 mounting

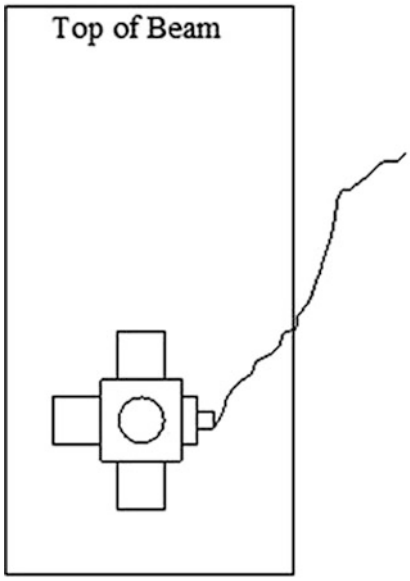

Fig. 10.8 8840 mounting

10.5 Investigation of Shaker Performances Regarding Shaker Head Rotation Using Rotational Accelerometers

Shakers are designed to ideally generate a uniaxial sinusoidal excitation movement at a given frequency. In reality, the movement generated by a shaker also contains components perpendicular to the oscillation axis, introducing what we call shaker head rotation. Depending on shaker quality/performance, those shaker head rotations can be significant, especially at some specific frequency range that could influence results of calibration or modal analysis.

A comparison between two shakers has been performed using an 8840 rotational accelerometer mounted at the shaker center (Fig. 10.9). A frequency sweep has been performed between 20 and 10,000 Hz for different orientation of the 8840 sensors (from 0° to 180° with steps of 22.5°).

Figure 10.10 shows the output of the rotational accelerometer when mounted to shaker type A. The graph shows very low rotational acceleration output (<2.5 rad/s^2). Figure 10.11 shows the rotational accelerometer mounted to shaker type B. This graph shows much higher rotational accelerations especially between 3,200 and 6,000 Hz as well as toward the high frequency limits (<40 rad/s^2). This shows that shaker type B is inducing 16 times more shaker head rotation than shaker type A. It should not be used for high accuracy calibration or high accuracy modal analysis investigations.

In one study, it was demonstrated how shaker head rotations can influence results on calibration data or on modal analysis results [3]. Shakers with high rotational outputs can affect accelerometer calibration results. The sensitivity of the sensor to these rotations can be dependent on the sensor element design.

The optimization of linear accelerometer features for specific applications has resulted in a wide selection of potential accelerometers for any application. Modal analysis sensor designs have been created with emphasis on minimizing size, weight and cost which has resulted in the use of asymmetric seismic systems within the sensor. These designs may have an inherent sensitivity to rotational inputs [2].

When these asymmetric design accelerometers are calibrated or qualified, the rotational acceleration of the shaker head cause measurement artifacts and are apparent in the transfer functions or calibration curves at the most rotationally active frequencies [3]. An understanding of their existence and influence by investigating them with rotational accelerometers is important. When measurement of highly flexible structures at nodal points is of interest, special attention should be paid to the rotational susceptibility of the measuring sensor.

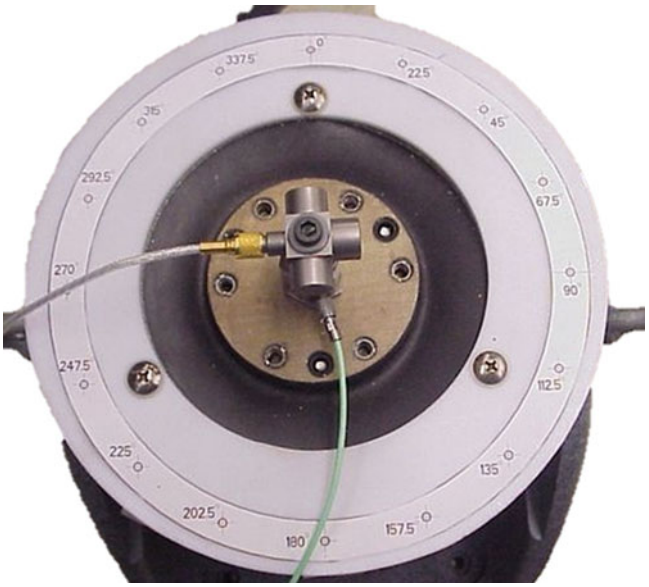

Fig. 10.9 Measurement setup. 8840 sensor mounted on top of the shaker under investigation

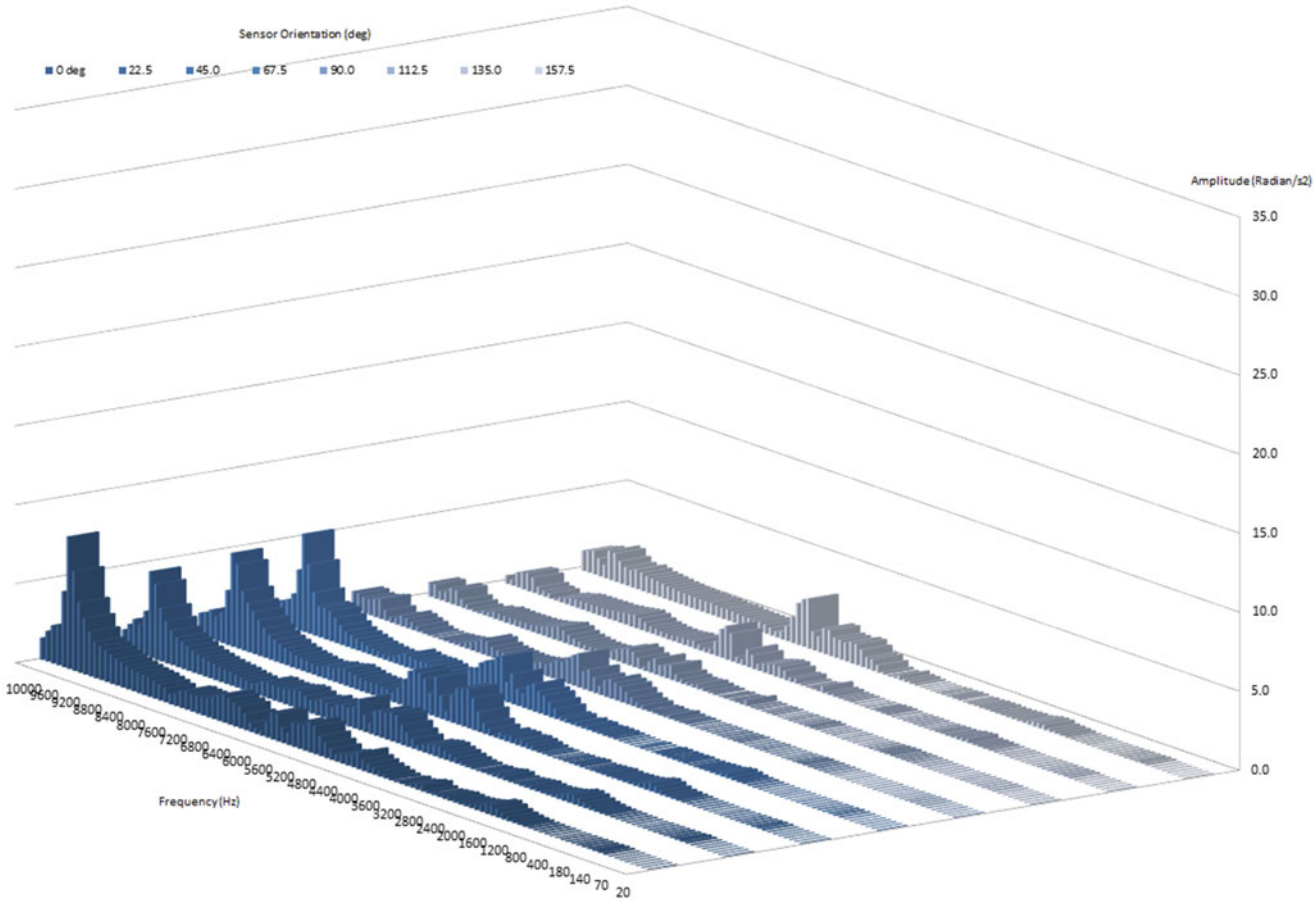

Fig. 10.10 Shaker type A. Rotational acceleration versus frequency versus 8840 sensor orientation

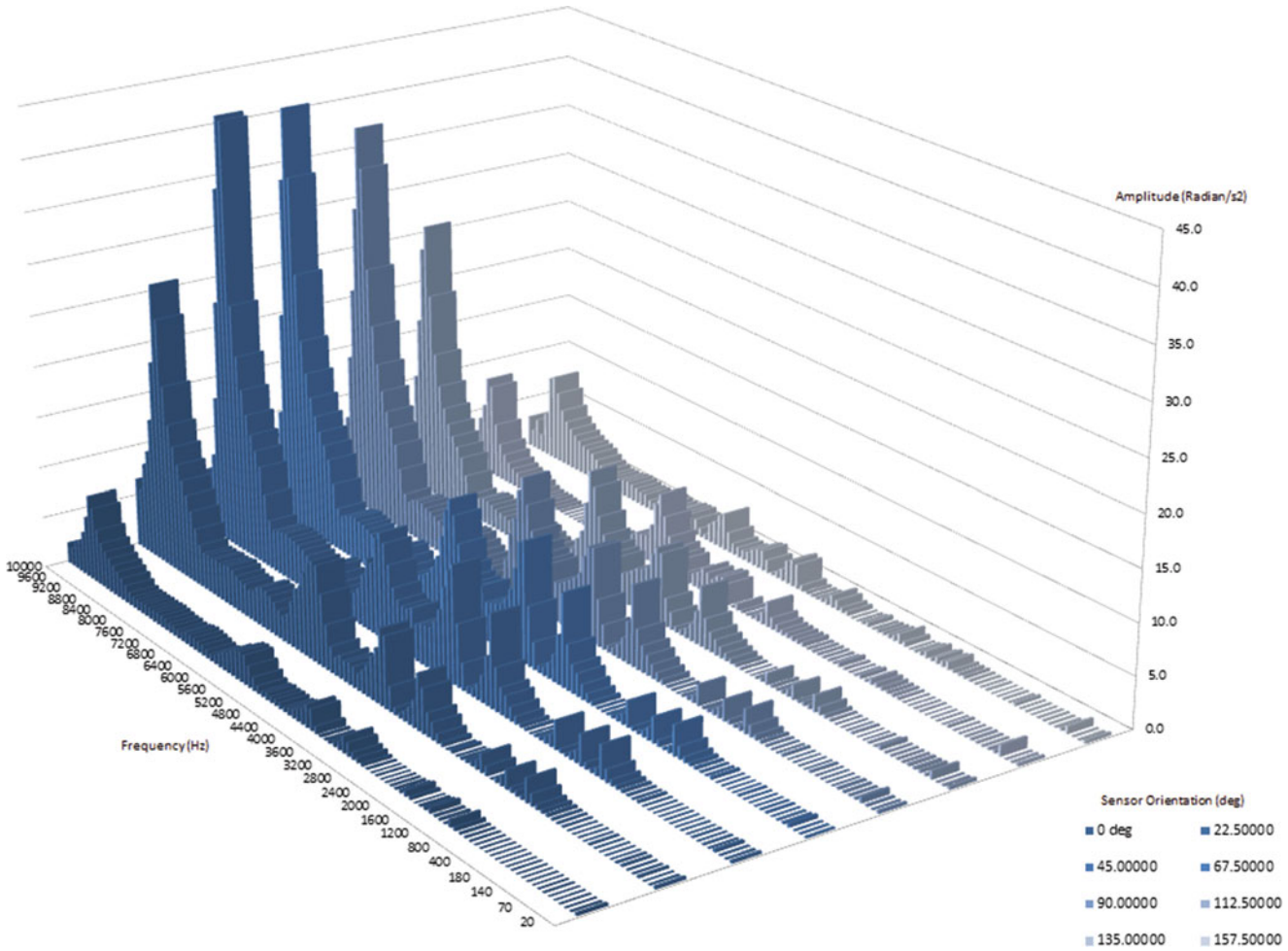

Fig. 10.11 Shaker type B. Rotational acceleration versus frequency versus 8840 sensor orientation

10.6 Summary

Angular acceleration measurement and rocking motion considerations are topics not often encountered in literature. This paper intends to give an overview on how those topics can be of high importance for modal analysis applications.

We have shown here that for many years rotational acceleration has been measured using linear accelerometers. Studies have shown that this could lead to high measurement errors where dedicated rotational sensor design was optimized for high sensitivity, high linearity and high stability.

Looking more into application of angular acceleration, we have seen how shaker head rotation can be of high or minor importance depending on the shaker quality chosen for modal analysis applications or calibration. If the sensors used during modal analysis or the reference standard used during calibration have an internal design sensitive to shaker head rotations, this could influence your results and accuracy.

References

1. Insalaco Michael D. The art of fabricating a rotational accelerometer, Kistler Doc K20.301e
2. A consideration of the effects of local rotations on the output of various accelerometers designs, Kistler Doc 20.167e
3. Cabral A, Godinho MI, Oliveira V, Rebordão JM, Nunes MC. Primary laser vibration metrology: evaluation of the rocking motion impact in the accuracy of acceleration measurements